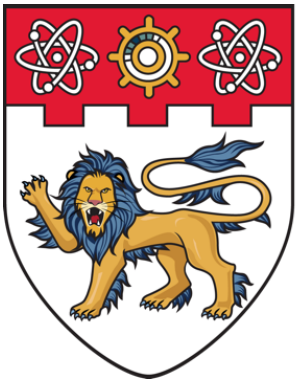

NANYANG TECHNOLOGICAL UNIVERSITY
SINGAPORE

LARGE SCALE 3D CONCRETE PRINTING: PROCESS AND MATERIALS PROPERTIES

YI WEI DANIEL TAY

SCHOOL OF MECHANICAL AND AEROSPACE ENGINEERING

2020

LARGE SCALE 3D CONCRETE PRINTING: PROCESS AND MATERIALS PROPERTIES

YI WEI DANIEL TAY

SCHOOL OF MECHANICAL AND AEROSPACE ENGINEERING

A thesis submitted to Nanyang Technological University in partial fulfilment of the requirement for the degree of Doctor of Philosophy

2020

Statement of Originality

I hereby certify that the work embodied in this dissertation is the result of original research, is free of plagiarised materials, and has not been submitted for a higher degree to any other University or Institution.

22/7/2019
Date

Tay Yi Wei Daniel
[Input Name Here]

Supervisor Declaration Statement

I have reviewed the content and presentation style of this dissertation and declare it is free of plagiarism and of sufficient grammatical clarity to be examined. To the best of my knowledge, the research and writing are those of the candidate except as acknowledged in the Author Attribution Statement. I confirm that the investigations were conducted in accord with the ethics policies and integrity standards of Nanyang Technological University and that the research data are presented honestly and without prejudice.

23/7/2019

Date

Tan Ming Jen

[Input Supervisor Name Here]

Authorship Attribution Statement

This dissertation contains material from [6] paper(s) published in the following peer-reviewed journal(s) in which I am listed as an author.

Chapter 2 is published as Y. W. D. Tay, B. Panda, S. C. Paul, N. A. Noor Mohamed, M. J. Tan, and K. F. Leong, "3D printing trends in building and construction industry: a review," *Virtual and Physical Prototyping*, vol. 12, no. 3, 2017. DOI: 10.1080/17452759.2017.1326724
The contributions of the co-authors are as follows:

- Prof. Tan and Prof. Leong provided the overall initial project direction.
- Mr. Mohamed and Mr. Panda contributed a few paragraphs in the article. The "Building information modelling" section was contributed by Mr. Mohamed and the "Concrete printing research at SC3DP section" was contributed by Mr. Panda.
- I prepared the rest of the manuscript drafts and the manuscript was revised by Dr. Suvash.
- I designed the methodology to review existing related papers systematically and analyses the data in this article.
- I compiled the state-of-the-art technologies in the related research field and also compiled the "material research in SC3DP" section.
- The experimental work shown in the article were carried out by me, Dr. Suvash, Mr. Mohamed and Mr. Panda.
- I also prepared the "Future work" section under the guidance of Dr. Suvash and Prof. Tan.

Chapter 2 is also published as Y. W. D. Tay, B. N. Panda, G. H. A. Ting, N. M. N. Ahamed, M. J. Tan and C. K. Chua, "3D Printing for sustainable construction" presented as a conference paper (keynote in 2nd International conference on sustainable smart Manufacturing (S2M 2019), April 2019, Manchester, UK.

The contributions of the co-authors are as follows:

- Prof. Tan, Prof. provided the overall initial project direction.
- Mr. Mohamed, Mr. Panda and Mr. Ting contributed a small portion of the article. Mr. Mohamed contributed a paragraph in Section 3 and some of the photos. Mr. Panda and Mr. Ting each contributed a paragraph in Section 2 of the paper.
- I prepared the draft rest of the manuscript and compiled the contribution from the rest of the co-authors together.
- The manuscript was revised by Prof Tan before submission.

Chapter 3 is published as Y. W. D. Tay, B. Panda, S.C. Paul, M.J. Tan, S.Z. Qian, K.F. Leong, C.K. Chua, "Processing and properties of construction materials for 3D printing," in Materials Science Forum, 2016, vol. 861, pp. 177–181. DOI: 10.4028/www.scientific.net/MSF.861.177

The contributions of the co-authors are as follows:

- Prof. Tan, Prof. Qian, Prof. Leong and Prof. Chua provided the overall initial project direction.
- I prepared the manuscript drafts and the manuscript was revised by Dr. Suvash.
- I tailored the mixture design and carried out the material preparation. The printing work was carried out by Mr. Panda, Dr. Suvash and me. All experimental work is carried out in School of Mechanical and Aerospace Engineering, Singapore Centre for 3D Printing (Building and Construction Lab).
- Dr Suvash provided guidance in the interpretation of the obtained result data.

Chapter 3 is also published as Y. W. D. Tay, Y. Qian, and M. J. Tan, "Printability region for 3D concrete printing using slump and slump flow test," Composites Part B: Engineering, vol. 174, pp. 1–9, 2019.

The contributions of the co-authors are as follows:

- Prof. Tan, Prof. provided the overall initial project direction.
- I prepared the manuscript drafts and it was revised by Dr. Qian.

- I established the methodology to quantify the different mix design.
- I also established different testing protocol to determine the characteristic of the different mix design.
- I carried out all of the experiment in the School of Mechanical and Aerospace Engineering, Singapore Centre for 3D Printing (Building and Construction Lab).
- I analyses the slump and flow diameter data and interpreted the printing results. With the slump and flow diameter results and the printing results, I combine both results to obtain the material printability region.

Chapter 4 is published as Y. W. D. Tay, M. Y. Li, and M. J. Tan, "Effect of printing parameters in 3D concrete printing: Printing region and support structures," Journal of Materials Processing Technology, vol. 271, pp. 261–270, 2019.
The contributions of the co-authors are as follows:

- Prof. Tan, Prof. provided the overall initial project direction.
- I prepared the manuscript drafts and it was revised by Dr. Li.
- I carried out all of the experiment in the School of Mechanical and Aerospace Engineering, Singapore Centre for 3D Printing (Building and Construction Lab).
- I processed the image and obtain the data that I need for charactering the printing parameters effect on the filament.
- I proposed the method of analyzing the data under the guidance of Dr. Li.

Chapter 5 is published as Y. W. D. Tay, G. H. A. Ting, Y. Qian, B. Panda, L. He, and M. J. Tan, "Time gap effect on bond strength of 3D-printed concrete," Virtual and Physical Prototyping, vol. 14, pp. 104–113, 2019.
The contributions of the co-authors are as follows:

- Prof. Tan, Prof. provided the overall initial project direction.
- I prepared the manuscript drafts and it was revised by Dr. Qian
- I discussed the testing protocol with Mr Ting and Mr He.
- I tailored the mixture design and carried out the material preparation. The printing work was carried out by Mr. Panda, Mr Ting and me. I also carried

out the rheological experiment myself. All experimental work is carried out in School of Mechanical and Aerospace Engineering.

- I analyses, interpreted and verify the rheology result with actual photos of the samples.

Chapter 6 is submitted as Y. W. D. Tay, J. H. Lim, N. H. A. Koh, M. Y. Li, and M. J. Tan, "Creating 3D Concrete Functional Graded Materials with Varying Printing Parameters" to Journal of Automation in Construction.

The contributions of the co-authors are as follows:

- Prof. Tan, Prof. provided the overall initial project direction.
- I prepared the manuscript drafts and is revised by Dr Li.
- I tailored the mixture design and carried out the material preparation. The printing work was carried out by Dr. Li, Mr. Lim, Mr Koh and me. All experimental work is carried out in School of Mechanical and Aerospace Engineering.
- Mr. Lim assisted in the topological optimization work. Dr Li, Mr Lim and I discussed on the parameters and model to use for the optimization. Dr. Li assisted in generating the printing code.
- Mr Koh and I performed all structural testing and prepared all the data collected.
- Dr Li also provide guidance on the interpretation of the result obtained.

22/7/2019

Date

Tay Yi Wei Daniel

[Input Name Here]

Abstract

The main challenge for the 3D concrete 'ink' to be printable is the contradicting characteristic it should possess. It should be flowable enough to be pumped through the hose as well as having sufficient strength for buildability during the layer-by-layer deposition. This posed a challenge as the mixture needs to overcome the internal shear resistance arising from the interaction between the particles to be pumpable and it requires sufficient shear strength for shape preservation after extrusion. Most of the existing studies that proposed mixture for 3D concrete printing used rheometers measuring dynamic yield stress and plastic viscosity. As the measurement with rheometer is sensitive to the protocols and control by the rheologists, as well as data processing if non-standardized measuring geometries are used, results could vary significantly. Little exploration on the material region of printability has been done for 3D concrete printing. This propels the motivation to investigate the material characteristic limits for printability (e.g. pumpability and buildability). A field-friendly protocol will be proposed to measure the slump and flow diameter of the mortars, which will be used to define the material printable region and are evaluated with the pumpability and buildability parameters of the mixtures.

Apart from the material aspect, the printing parameters also play an important role in 3D printing. Inappropriate printing parameters can have an adverse effect on the printed structure strength and stability. Since this technique prints layer-by-layer, the time taken to reach the same position in the subsequent layer is important as it will create an anisotropic property that has a weaker tensile strength at the bond interface of the two printed filaments. Through rheological

measurement, which reveals the material deformation and flow behaviour, and observation on the printed filament at macroscopic-scale, it is possible to examine the effect of time gap on the material structural build-up and how it affects the bonding between different layers.

Furthermore, through investigation of the print filament at different material flow rates and nozzle travel speeds, it is possible to identify the parameters for different printing operations. Different printing operations can be used to obtain different type of filament for various purposes. Functionally graded concrete material, which offers effective conservation of material usage and high performance of integrated structures efficiency, can be achieved with this technique. It can be obtained by 3D printing given that the printer has the ability to dynamically vary the material structure in complex 3D distribution and can produce a continuous gradient in a 3D printed part. Varying parameters allow for optimization of the material properties relative to their structural and functional performance. An optimized structure varying gradient was used to verify the performance of a functionally graded material (FGM) printed structure in terms of flexural strength-to-weight ratio.

Lastly, a full-scale pre-fabricated unit PBU is printed and the methodology to increase the scale was shown in this dissertation. In most literature, the printing takes places on a small scale, however, in order to increase the size of the printed part alteration to the material is necessary. This dissertation ends with a chapter describing the steps needed for large scale printing and the methodology to design the mix design. The economic evaluation shows that 3D concrete printing can save

around 25% of the total cost to produce the main concrete structure when compared with formwork casting method.

Acknowledgement

The author would like to express his sincere gratitude to his Ph.D. supervisors, Associate Professor Tan Ming Jen and Associate Professor Leong Kah Fai, for their great patience, invaluable academic inspiration, knowledge, guidance and support to his study and research. The author would also like to express his gratitude to Dr. Suvash Chandra Paul and Dr. Li Mingyang for sharing their knowledge and experience in their specific field and has significantly contributed to this research. This research is supported by the National Research Foundation, Prime Ministrer's Office, Singapore under its Medium-Sized Centre funding scheme, Singapore Centre for 3D Printing, and Sembcorp Design & Construction Pte Ltd. Lastly, the author would like to thank his family and friends for their love, patience and support throughout the process of his study and research.

Table of Contents

Chapter 1: Introduction

1.1 Background

Concrete is usually poured into a formwork that provides temporary support as well as performs as a mould that shapes the freshly placed concrete to the desired configuration. Formwork has been used extensively in the building and construction industry. While this construction process can produce homogenous material where the strength is the same throughout [1], it is a labour-intensive process. Usually, complex architecture is limited by the manufacturing method of the formwork. Furthermore, formwork accounts for 40-60% of the cost of the concrete frame and around 10% of the total building cost [2]. A portion of this cost is related to the labour required. In most cases, to reduce the cost of the formwork, walls are designs with simple and replicated design. This is to ensure that the formwork can be reused for subsequent projects.

3D printing technology, also known as additive manufacturing (AM), has increasingly become more evident over the past few years. It is a process where a three-dimensional computer-aided design (CAD) model can be materialized layer-by-layer. It has made a huge impact not only in aerospace, medical and consumer industries but also in the field of construction. In the recent decade, there has been an increase in interest in both academia and commercial application of 3D concrete printing. Tay et al. [3] reviewed the research papers relating to concrete printing until 2017 and found out that the number of the research paper in this field has increased exponentially since 2011.

3D concrete printing is a sustainable solution because of its ability to manufacture complex shapes to enable passive-design thus reducing energy consumption. Sustainability is interpreted as the effective use of resources as well as the preservation of the environment. A sustainable building is giving back to the environment more than it takes and ensuring that the resources are being used in an effective way that would benefit the community. Sustainable construction is a broad term and can involve different types of issues [4]. In general, sustainable construction is the aim to meet present-day needs for infrastructure, housing and working environments without compromising the ability of future generations to meet their own needs in times to come. This means ensuring that resources are being used in an efficient way that would benefit the community and the world.

A combination of smart design, efficient technology and designing buildings with sustainability in mind from the start of the designing phase is therefore necessary. In addition, the correct use of green materials and selection of sustainable complex architectural design can amplify the sustainability of this technology. The potential of this technology when it reaches maturity can revolutionize the construction market and make major changes such as shorter building time, cheaper construction, reduced labour involvement, less material wastage, freedom of shape and integration of functionality [5], [6]. All these reductions are eventually translated to cost-saving, which compel the exploration of using 3D printing in construction for structural with customized complex geometries.

Concrete pumpability during delivery and buildability after extrusion are important aspects of 3D concrete printing. Pumping of concrete is a complex process. Notwithstanding the time-dependent behaviour, the changes in the concrete

properties due to pumping condition such as segregation can make the material hard to predict. Furthermore, without the use of temporary support of the formwork, the material depends on its internal cohesion between the paste and the aggregates to retain its shape after extrusion. Both the shape retention and the supporting load of the subsequent layer require high static yield stress for buildability.

Currently, there is no standard test method to measure or quantify pumpability and buildability for 3D printing. Existing research has proposed various mixtures for 3D concrete printing through rheology characterization using rheometers [7], [8]. However, these rheological tests are sensitive to the protocols and the operation procedures by researchers [28]. The values obtained vary among the different apparatus [29]. Hence, standardize and field-friendly tests such as the slump and flow table tests are proposed to characterize the mix designs and to determine the printability region. The slump value is the difference in the height between the mixture and the mould after the mould is removed. The flow diameter value of the material is measured as the material's spread on the plate after dropping for 25 times. It could be regarded that dropping for 25 times makes the difference in the mixtures corresponding to the microstructural breakdown. Thus, the slump value is more related to the solid-state of the microstructure, which is the static yield stress, and buildability. The flow diameter value is related to dynamic yield stress and pumpability. Past research has shown that the slump value is inversely proportional to the dynamic yield stress [30].

The printing parameters are another important factor in 3D printing. Figure 1.1 shows the importance of coordinating the printing parameters. Furthermore, varying the printing parameters can create a filament with different properties. Most

of the current research work in 3D concrete printing focuses on new printable materials and possible structural design to improve mechanical strength [9], [10]. There is little research on the topological optimization of the printed structure especially in the direction perpendicular to the print path [11]. Since this manufacturing technique produces structure in an additive manner, by controlling the amount of material being deposited, a structure with different mechanical properties can be created. Printing a functionally graded concrete material (FGCM) structure helps to improve the strength-to-weight ratio, which saves on the load-bearing requirements of the structure as well as improves the use of resources effectively. Such an approach increases the complexity of a structure without affecting the printing cost. Therefore, the effects of the change of volume flow rate and travel speed on the printed filament are investigated. This investigation aims to create a concrete structure with spatially varying microstructure for optimal structure efficiency and maximum strength-to-weight ratio. This objective-tailored material can be achieved by adjusting either its volume flow rate or travel speed at a specific region of the print. To the best knowledge of the author, this approach has never been done for concrete material.

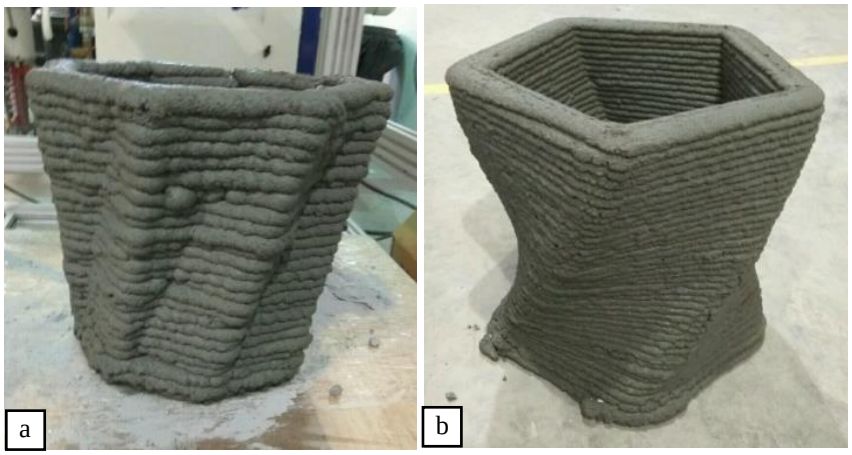

Figure 1.1: (a) Poor balance between travel speed and flow rate (b) proper balance between travel speed and flow rate

Finally, in order to increase the scale of the printed element, the material characteristics and the printing parameters should be complimenting. Either the printing parameters need to reduce the speed to accommodate the stiffening rate of the concrete or the stiffening rate of the concrete need to increase to satisfy the short time gap. Time gap is defined at the time needed for the subsequent layer to be deposited on the current layer. In most cases, concrete mixture without additive will not be able to print more than 0.5 m structure due to the slow stiffening rate. Therefore, the addition of admixture to accelerate the hydration process is required for printing large-scale object.

1.2 Research motivation and objective

The investigation of most existing material research for 3D concrete printing has explored the use of rheometers to examine the yield stress and viscosity. The use of rheology for characterization is a complex technique and the result is sensitive to the protocol. A test using a simple apparatus with a standardize procedure would be preferred. Furthermore, there is a lack of existing research to examine the printability

region of the material. The consistency of a printable material may reach the maximum limit of most rheometers and enter the region of hardened material testing [9]. This investigation of the printability region can be used as a benchmark to characterize other types of material for printing.

Additionally, the imbalance between the printing parameters can have an adverse effect on the printed structure in both its fresh and hardened state. The stability of the printed structure during its fresh state and the strength of the material at its hardened state might be compromised. A printing index should be introduced to characterize the filament quantitatively. With the coordination of the printing parameters, the research can be furthered to investigate the feasibility of printing an FGCM, which has never been done before in 3D concrete printing.

Finally, the printable material and the printing parameters must be coordinated in order for successful large-scale 3D printing. Choosing the correct stiffening rate to fit the printing parameters is important not only to prevent the structure from collapsing but also to prevent rapid hydration from occurring which may reduce the interlayer bond strength.

The above-specified motivation of the research leads to the objective of the research specified below:

1. To establish tests required to determine the printability of the material for benchmarking.
2. To investigate the effect of time gap on the inter-bonding layer strength
3. To investigate the effect of printing parameters on 3D concrete printing and to correlate the printing parameters with the material characteristics.
4. To explore the feasibility of printing FGM with cementitious material.

5. To match the material stiffening rate with the printing parameters for large-scale printing

1.3 Research scope

The slump and flow table test will be used to characterize the printability of the material. This field-friendly and low-cost method can be related to the static and dynamic yield stress of the cementitious material. Different mixtures with different slump and flow diameter values will be used to map out the printable region. With this set of experimental data, it can be used as a benchmark for developing other types of cementitious material. Furthermore, the effect of the printing parameters (e.g. the flow rate and travel speed) on the printed material properties will be investigated. This investigation can propose a few different printing parameters for different application. Using the same material, different regions of the structure can be printed with different properties to achieve an FGCM. The improvement of this FGCM printed material has to be quantified by the flexural strength-to-weight ratio. The improvement of this FGM will be compared to the controlled 3D printed structure (e.g. structure printed without optimisation) through three-point bending test. Finally, the matching of the material stiffening rate and the printing parameters is important to achieve large-scale printing. The stiffening rate is measured by using the material yield stress at different time intervals. This alteration of the stiffening rate can be achieved with the adjustment to the amount of the accelerator admixture added. The rate of loading of subsequent layers can be calculated by the travel speed and the distance of each layer. In order to achieve low deformation at the lower layer, the stiffening rate of these lower layers should be faster than the rate of loading of the

subsequent layers. However, in order to prevent the structure from falling and to achieve high bond strength at the inter-bonding layer, the stiffening curve should be close to the curve of the loading rate without crossing it.

1.4 Report outline

This dissertation is arranged in the following order. In chapter 1, the background of the 3D concrete printing will be introduced followed by the research objective and the scope of this project. Chapter 2 will present the existing 3D printing techniques in the construction industry and the challenges in concrete printing. The sustainability of concrete printing in terms of design and materials will also be reviewed. The printable material benchmarking properties and the effect of aggregates and paste content will also be reviewed in this chapter.

In chapter 3, the material research on the printability region will be presented. The slump and flow table test printing investigation protocol are described in this section. In order to validate the printability region, actual printing test will be used to characterize the material behaviour. Due to the complexity of concrete, no admixture was used in this section since the focus is on the printability region and an excessive number of ingredients often make a concrete mixture difficult to control.

Chapter 4 and 5 focus on the time gap effect on the material bond strength and the experimentation of printing parameters. The time gap effect of the printing parameters has on the inter-bonding layer will be discussed. Comparison between the rheometer and the visual inspection on the inter-bonding layer results are shown in Chapter 4. Additionally, in Chapter 5, the effects of printing parameters on the fresh material properties will be discussed. Printing speed which is the balance of nozzle

travel speed and the flow rate has a significant effect on the strength of the filament in the fresh state. In order to verify the significance of balancing the printing speed, a structure with support elements was printed. Different printing regions can be used to print the same materials with different properties. Furthermore, the significant of the gap distance is discussed in this chapter.

Chapter 6 presents investigation research on printing functionally graded concrete material. Printing a 2D optimized structure was explored and the results were compared with the un-optimised structure. The significance of the acceleration and deceleration during printing is discussed in this chapter. Chapter 7 will focus on coordinating the material stiffening rate and the loading rate of the printing parameters. The rheological results in comparison with the calculated loading rate will be validated with the printing of a full-scale prefabricated bathroom unit. Finally, this dissertation will end with a conclusion and some future research recommendation in Chapter 8.

Chapter 2: Cementitious material and technologies for 3D printing

2.1 State-of-the-Art technologies for 3D printing in B & C

The rapid development of large-scale 3D concrete printing technology in most literature is categorized into two techniques, which are the binder jetting technique and the material deposition method (MDM). The basic principle of both techniques is to build up any complex structure by adding material in small layers. It begins with the creation of a 3D CAD model, which is sliced into several 2D layers and then printed with an assigned material in an incremental manner to obtain the prototype as described in the CAD model.

2.1.1 Binder Jetting

Binder jetting is a 3D printing process that creates objects by depositing binder layer by layer over a powder bed. Figure 2.1(a) shows the printer used for binder jetting. Binder is ejected in droplet form onto a thin layer of powder material spread on top of the build tray. This method incrementally glues 2D cross-sections of the intended component to each layer of material powder [12]. Any raw material that is not glued by the binder remains inside the container and is used to support the subsequent layers. The cycle repeats until the whole 3D object is complete as shown in Figure 2.1(b). The unbound material can be removed from the print bed using a vacuum cleaner after the printing process, which can be recycled and deployed for another printing task [13]. This method encourages designs to have voids and overhanging features which enable the printing of complex geometries. It has a relatively high resolution that results in the good surface finish because of the small layer thickness. This layer thickness value is determined by the penetration of the

binder. If the layer thickness is too large, the binder may not penetrate deep enough to glue the current and the previous layer together [14].

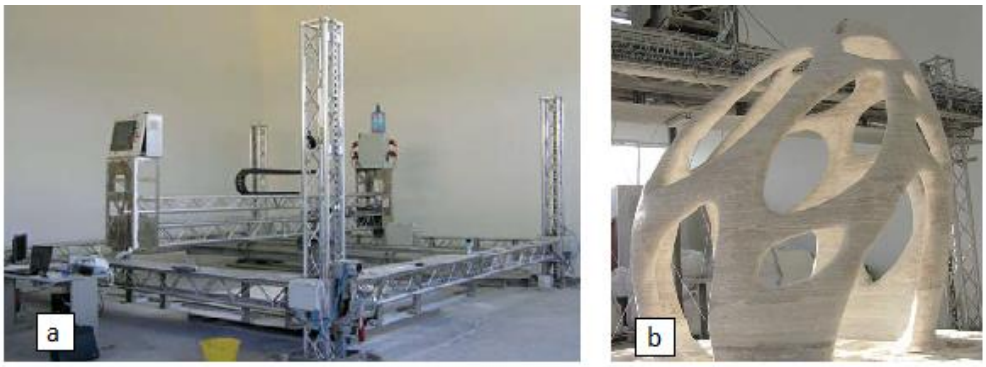

Figure 2.1: (a) D-shape printer (b) Final printed component with all the excess raw material removed [15]

2.1.2 Material Deposition Method (MDM)

Similar to fused deposition modelling (FDM), material deposition method (MDM) is a 3D printing process that successively lays material as per the CAD model [16]. While there are many materials such as polymer gels [17] and wood [18] that can be extruded for large scale design, this section focuses on extrusion methods that can be used for the construction industry and showcase some of the advancement made in this industry in recent years by various research groups around the world.

Contour Crafting

Contour Crafting (CC) is a gantry-based system that extrudes material in a layer-by-layer manner. The key feature of CC is the use of trowels attached to the nozzle. The trowel guides the printed material to create exceptionally smooth and accurate surfaces as shown in Figure 2.2. This trowel can be deflected at different angles (by computer control) to create various non-orthogonal structures. Such an

approach enables deposition of higher layer thickness without significantly compromising the surface finish [19]. Figure 2.3 displays contour crafted structures made of ceramic and concrete material. The detailed material composition and printing procedure are described in [23], [25]. It is also reported that printed walls with embedded conduits for both electricity and plumbing as well as structural reinforcement can be achieved through CC [19].

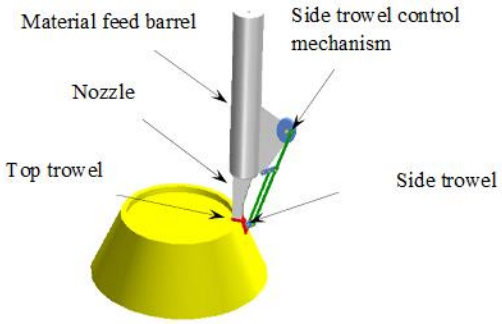

Figure 2.2: Contour crafting process [19]

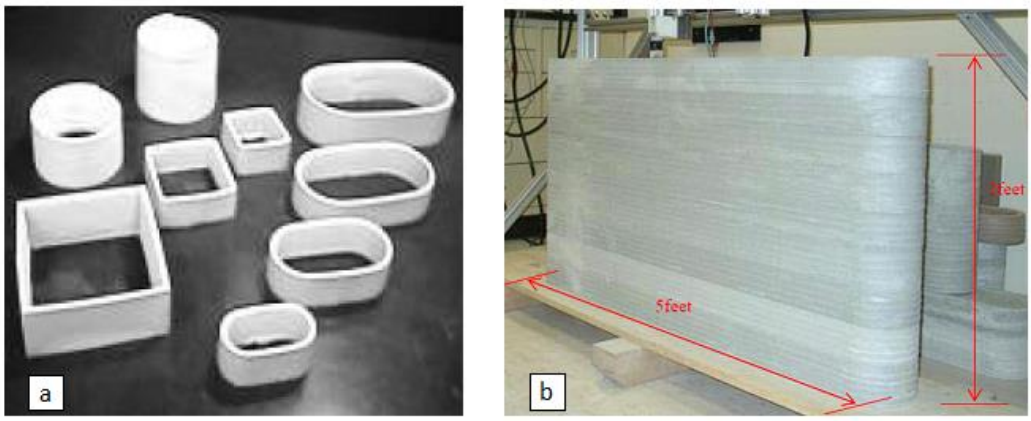

Figure 2.3. Contour crafting using (a) ceramic and (b) cement material [23, 25]

Curve-bed printing

Most MDM is categorized as flat-layered printing. Flat-layered printing extrudes material in a two-dimensional plane layer-by-layer until it reaches the

desired volume. This printing method creates mechanical weaknesses such as anisotropic properties and creates visual issue such as staircase effect on the completed print surface. Recently, Lim et al. [22] introduced another method of curved-bed printing. Curved-bed printing improves the aesthetic and mechanical properties of a printed part [22]. Figure 2.4(b) shows a concrete panel printed on a non-layered panel.

Certain new terms were introduced by the research group used to describe the flow of material deposition in this method due to the fresh properties of the concrete. “Over-printing” is when too much material is deposited at a specific point, causing unnecessary bulging of the printed part. “Under-printing” is when there is a lack of deposited material at a point which may cause breakage during printing. These problems, however, can be addressed by fine-tuning the machine operating parameters or modifying the tool path.

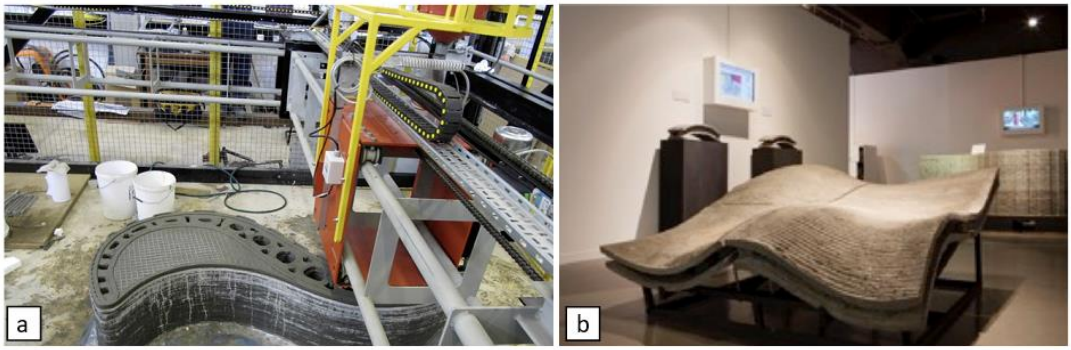

Figure 2.4: Concrete printing at Loughborough University [8].

Printer configuration

Different types of printers were proposed by researchers from all over the world and two of the most interesting printers were mini-builders and digital construction platform (DCP).

Mini-builders is a coordinated system of three individual robots that is built for the fabrication of in-situ construction. They are lightweight, compact and have autonomous mobility. Each robot has a different function during the printing process as described in detail by Nan [23]. A two-component resin material was developed for these robots as the speed of the robot determines the extrusion rate. If the material's curing time is not compatible with the flow rate and the robot travel speed, the material may clog in the hose. An additional heat source can be added depending on weather conditions for expediting the chemical reaction and reducing the curing time of the printed material.

DCP is a system used for on-site sensing, analysis and fabrication built by a group of researchers at Massachusetts Institute of Technology (MIT) [24]. This system is designed around a large boom, which is used for gross positioning to increase speed, accuracy and ease of access with a small robotic arm. Using ground reference sensors and an accelerometer allows the closed-loop system to accurately position the end effector. In this system, polyurethane foam is used as the material for printing because of its rapid curing time and its high insulating value. Printing a wall of a twelve-foot-long dimension would only take around five minutes. Besides being used for printing, the end effector is interchangeable and can be switched to a mill head for a subtractive manufacturing process if a finer surface finish resolution is desired.

Mesh mould

This technique utilizes a large 6-axis robot to extrude thermoplastics polymer to print in-situ structures freely in 3D space. Pinpoint cooling using pressurized air at the nozzle during printing allows for a high level of control thus facilitating the weaving of wireframe structures freely in space shown in Figure 2.5a. In this application, the structures act as reinforcement for the concrete. Concrete is then poured over this formwork and later troweled manually to smooth the surface as shown in Figure 2.5(b). Using such methodology reduces the time required for fabrication of complex structures which becomes feasible for large-scale applications. Different density of mesh can be printed (See Figure 2.5(c)) according to the array of forces acting on the structures. More interestingly, the presence of the mesh increases the tensile force of concrete ultimately becoming a possible replacement of conventional steel reinforcement.

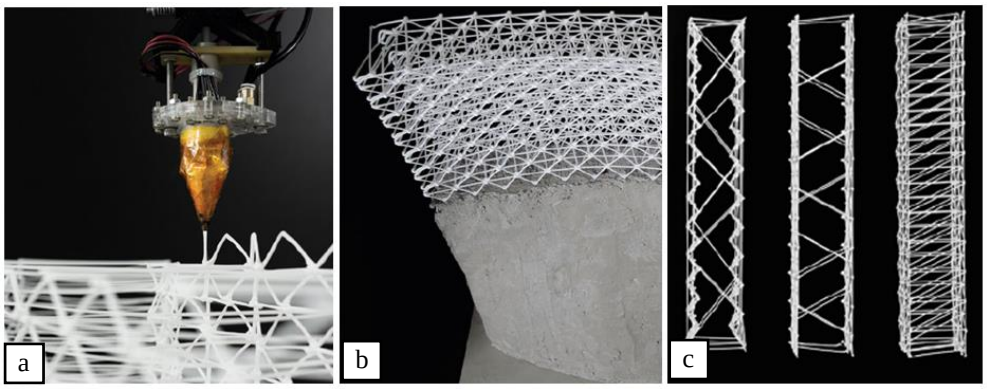

Figure 2.5. Mesh-mould combines formwork and reinforcement system for concrete [25]

3D scanning for restoration work

J. Xu et al. [26] uses 3D scanning technology with 3D printing technology to reproduce building components for the conservation and restoration of historical building ornaments. A hand-held 3D scanner was used to acquire the point cloud data of the intact building component which was processed into a digital model (See Figure 2.6 (a)). This digital model is loaded into a slicing software and the historical building component can be reproduced using the 3DCP technology as shown in Figure 2.6(b). Finally, the printed component is post-processed and installed to replace the existing damaged historical building component. This study shows that 3D scanning and 3D concrete printing are important tools that can be used for conserving and reproducing cultural heritage artefacts. However, the main challenge of such an application is the intricate patterns where high accuracy is required in both the scanning as well as the printing process.

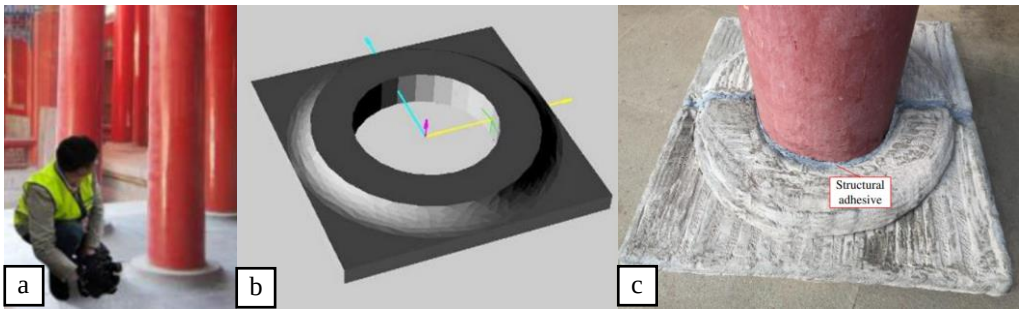

Figure 2.6: (a) 3D scanning of the intact plinth (b) converting to the STL model (c) printing and assembling of plinth [26]

Real-time monitoring and control for 3D concrete printing

A real-time height measurement and feedback system to monitor the nozzle height which is the distance between the nozzle to the substrate was developed by Wolfs et al. [27]. Due to the uneven print bed, the nozzle distance with respect to the print bed may not be consistent. An inconsistent print bed can cause a certain region of the printed filament to be squeezed as shown in Figure 2.7 (a).

Without a feedback system, the nozzle moves up by the design nozzle height each time it completes a layer. Furthermore, material deformation will the change in distance between the nozzle and the substrate [28]. As such, the actual nozzle height increases and deviates from the design nozzle height. The deviation of the actual nozzle height from the design nozzle height adversely affects the quality of the print as shown in Figure 2.7 (b).

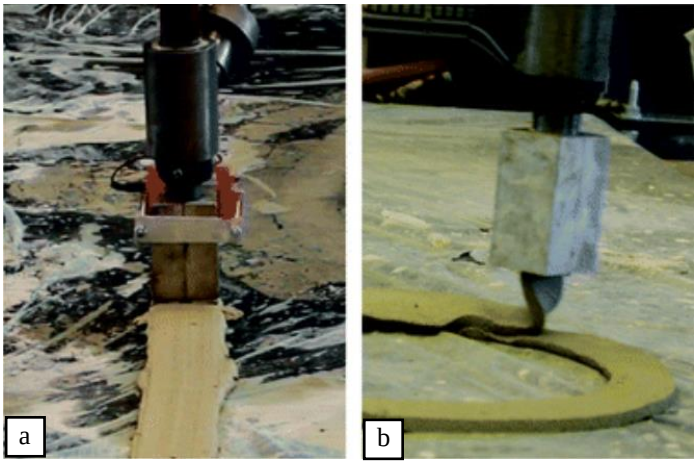

Figure 2.7: (a) Insufficient nozzle height resulting in the layer being squeeze (b) large nozzle height which results in the inaccuracy of filament placement [27]

The system uses a 1-dimensional time of flight distance measurement sensor (with an accuracy of approximately 1 mm) attached to the nozzle to measure the

distance between the nozzle to the substrate. The measurement data is continuously transmitted back to the control system which adjusts the nozzle position accordingly. Additionally, the printing along an arbitrary curved profile of which the nozzle variation in height position is not predetermined can be achieved as demonstrated in Figure 2.8.

Figure 2.8 Printing along the arbitrary curved profile without predetermining nozzle variation in height position [27]

Besides the correction of the nozzle height position, other feature such as correction of the extrusion rate can be used to monitor the dimensions of the printed filament. Kazemian et al. [29] use a camera attached to the extrusion head to monitor and capture the printed layers. The print quality is determined through an algorithm which measures the width of the extruded filament and compares with the target filament width to detect over-extrusion or under-extrusion conditions. The implemented feedback control system automatically adjusts the material deposition rate in order to achieve the desired dimensions of the printed layer.

While both of the real-time monitoring systems achieve its required performance, these monitoring systems have its limitation. Such equipment requires the section of the filament for real-time measurement as the nozzle travel along. It requires the filament to be straight without breakage. Tight corners and sharp turns are its shortcomings. Nevertheless, these monitoring systems help prevent the quality of printed structure from being affected by the inevitable variations in the material properties.

Interlayer adhesion

Due to the layering operation of 3D concrete printing, the interfaces of the layers are essentially vulnerable due to weak bonding of layers. Depending on the distance travelled by the nozzle at each layer, the interlaying time gap between the layer deposition changes, hence, affecting the layer interface bond strength as cold joint forms due to lack of material intermixing as the material sets.

Various researchers have proposed innovative solutions to enhance the interlayer bond strength in 3DCP. For instance, Zareiyan and Khoshnevis [30] proposed the use of mechanical interlocking between the printed layers to enhance the layer adhesion. They found that the interlayer bond strength peaked at a notch depth of 0.5” with 17% improvement by the uniaxial compressive test and 26% by the splitting test. On the other hand, Marchment et al. [31] enhanced the interlayer bond strength by applying a cementitious paste on the printed layer before the next layer is deposited above. Admixtures such as retarder, viscosity modifying agent (VMA) and superplasticizers were added to the cementitious pastes. It was found that

the cementitious paste with superplasticizer produced the highest interlayer bond strength with an improvement of 60% as compared to the control with no cementitious paste between the layers. Hosseini, et al. [32] also applied a novel polymer between the printed layers to enhance the interlayer bond strength. The polymer consists of black carbon as well as sulphur and an increase in interlayer bond strength tested by three-point bending test of more than 100% of the control was reported.

2.1.3 Concrete printing in SC3DP

The current research at the Singapore Centre for 3D Printing (SC3DP) has developed numerous printable construction materials such as geopolymer and fibre-reinforced mortar [33], [34]. Additionally, recycled glass, fly ash and cenospheres are incorporated to enhance the formulation for sustainable construction and lightweight properties [35], [36]. Other than the material investigation, the research activities in SC3DP have also devoted to the development of a machine for concrete printing applications. Figure 2.9 shows the different concrete printers at SC3DP. Typically, for large-scale printing, the gantry is more suitable due to its simplicity. However, for printing complex objects, the robotic printer is more practically suited due to its 6-axis rotational ability. In this dissertation, most of the investigation work was carried out on the gantry printer.

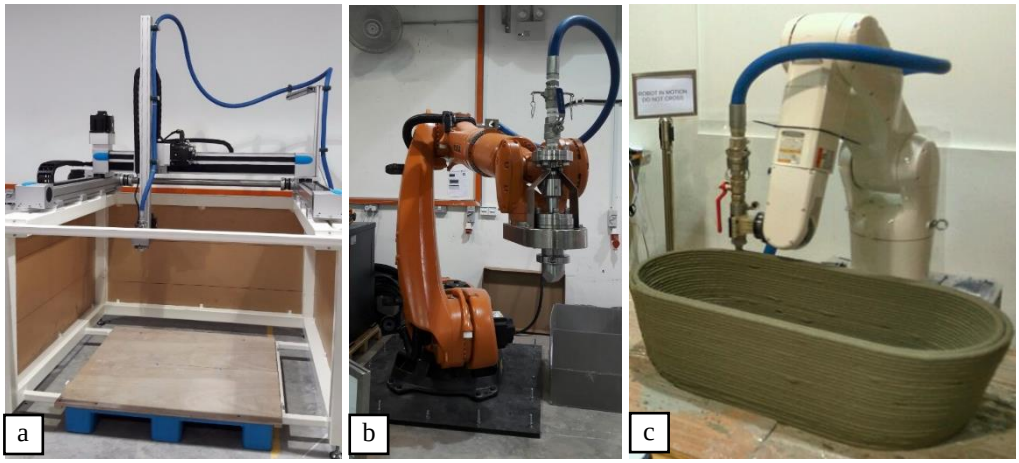

Figure 2.9. 3D concrete printers at SC3DP (a) gantry printer with a rotating nozzle (b) robotic printer with a rotating nozzle (c) six-axis robotic printer printing a miniature bathtub.

Furthermore, an innovative solution to overcome the scalability issue restricted by the gantry system or the reach of the robotic arm is developed in SC3DP. The maximum size of the printable structure is very much limited by the size of the gantry printer. Hence, large gantry systems have been built for the purpose of printing large scale structures in building and construction application. However, these gantry systems are often space-consuming and have low mobility for on-site printing. In some cases, the use of robotic arms has demonstrated improving the printing scale without excessive space needed for the robotic printer, but the scalability of the printed structures is still limited to the reach of the robotic arm printer. Zhang et al. [37] employed a team of mobile robots to work collaboratively for the application in large scale concrete printing. The team of two mobile robots as shown in Figure 2.10 printing a single joint structure with dimensions beyond the reach of the individual robotic arm concurrently demonstrates the capability of the multi-robot setup with improved time efficiency. The main challenge here was to avoid collision between the robotic arms movement by robot motion planning and coordination. The multi-

robotic arm printer concept improves the scalability of the printing in the horizontal directions but not on the vertical scale.

Figure 2.10 Concurrent printing of a single structure by 2 mobile robots [37]

2.2 Exploration of 3D concrete printing as a sustainable construction solution

2.2.1 Sustainable 3D printed passive designs

The energy used in the fabrication process, and the energy used in its operation after construction are equally important. The implementation of passive designs can dramatically reduce energy consumption and is an area where 3D concrete printing can potentially make a significant contribution because of the ease of creating a structure with high complexity. Printing passive design maximizes the potential of 3D printing to create comfortable space for the users. A passive system is a combination of energy-efficient design to take advantage of the climate to maintain the comfort level in an infrastructure. Such an approach reduces energy consumption during operation. However, such passive design has to be implemented during the design phase.

Apart from these passive designs, there are several sustainable materials that have a low carbon footprint that will amplify the use of 3D printing as a sustainable solution. Fly ash, geopolymer and recycled glass are some of the green material that has been used by the industry [38]. Although these sustainable materials have been used in conventional casting methods, the rheological behaviour for printing is different. The mixtures have to be tailored to this new manufacturing process for printing to be successful.

Management of passive cooling or heating effect

In warm climates, maximizing the use of natural airflow can reduce the energy load of the building. Excessive usage of air conditioning due to poor cooling efficiency design is not desirable. Clever designs such as “Cool Brick” can help in passive cooling [39] as shown in Figure 2.11(a). It is very important that this use of the natural cooling effect is incorporated in the design stage. In cold climates, the same principle should be applied in designing the insulation that could retain and recirculate the heat with minimum energy used.

The complexity of the shapes that can be printed by 3D printing is endless. The modular wall shown in Figure 2.11(b) is made up of modular blocks. These modular blocks can allow passive cooling and maximize the use of natural airflow while providing shade from the sunlight. Furthermore, such a design improves the appearance of the wall.

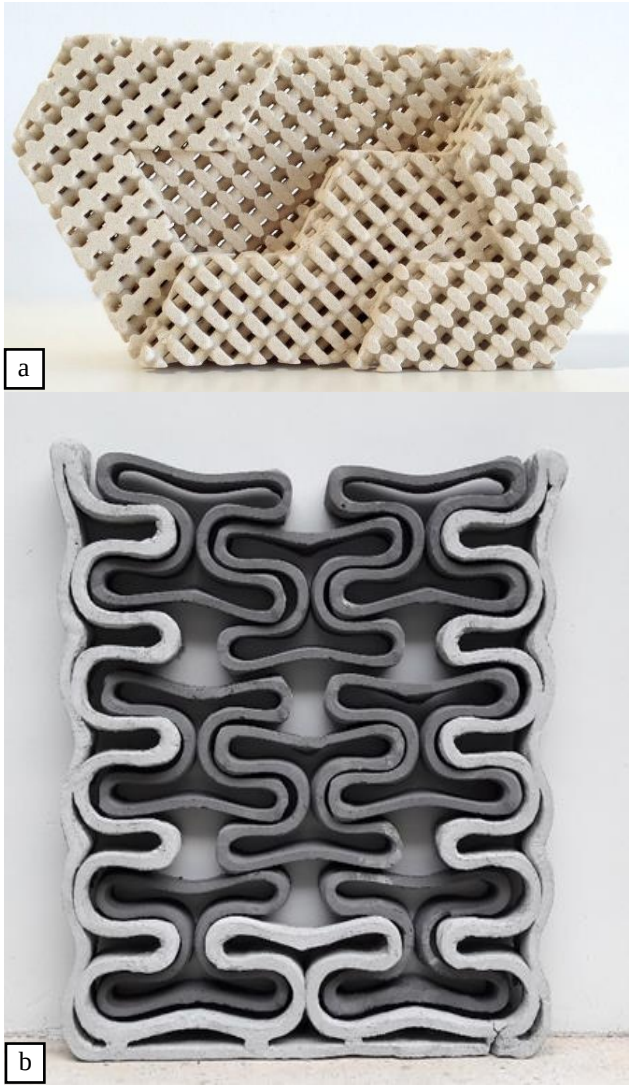

Figure 2.11. (a) Brick that provides passive cooling made by additive manufacturing [39] (b) 3D printed modular wall printed in SC3DP, NTU.

Management of natural lighting effect

Management of natural lighting is another important aspect. While the type of material and building orientation can achieve natural lighting, using additive manufacturing can control the lighting permeability while improving the appearance of the wall. Small modular blocks can be printed to control the amount of light allowed to be pass through as shown in Figure 2.12 [40]. Indoor spaces that are naturally brightened can reduce the need for artificial lighting at a later stage. Such

designs of using natural lighting need to be considered in the early stages of the designing process.

Extrusion over the doubly curved surface can be achieved with 3D printing without the need for formworks. Research work carried out in SC3DP, NTU printed the framework and was later assembled to form the curve bed for printing. The wireframe is then covered with a flexible textile to provide a surface for printing as shown in Figure 2.13. This printing serves as a proof of concept to build larger modular curved facades and complex architectural shape which can then be used for controlling the natural light.

Figure 2.12. Structure printed in modular that has different light permeability [40].

Figure 2.13. Curved bed printing with printed frames printed in SC3DP, NTU.

Management of acoustic effect

Dampening the sound surrounding the building or within the premises can improve the comfort of the user. Using passive designs can reduce the need for additional material for soundproofing. Figure 2.14 shows an element that was designed to enhance the soundproofing capability of a wall [41]. The generic elements were stacked together in order to form a complete wall. The geometries of the holes dampen the acoustic waves passing through.

Figure 2.14. Concrete printed acoustic wall element [41].

2.2.2 Sustainable printable materials

The rheological performance of printed concrete material is different from the conventional casted material. The usage of these materials that are going to be introduced is considered sustainable since dumping to a landfill will cause a negative environmental impact. The researchers working on these materials revolve around investigating a suitable mixture ratio to fulfil the required behaviour for printing.

High volume fly ash concrete

Fly ash-based materials are one of the possible alternatives for printing sustainable concrete structures. Fly ash is a by-product from the coal industry and is considered as a waste product. It contains some toxic metals that will degrade the soil and will cause air pollution. As such, a research carried out in SC3DP, NTU offers a suitable high-volume fly ash based formulation for 3D printing application which can reduce the environmental impact instead of disposing them to an open environment [42]. Hence, the high volume of fly ash was incorporated in the formulation and it

was found to improve long term strength performance of the building materials. The rheological properties of the printable material in its fresh state are crucial. Almost 80% of fly ash was utilized to formulate the mix design that exhibits thixotropic behaviour and achieves 35 MPa mechanical compressive strength, which is suitable for non-structural application [38].

Furthermore, this mixture is used to print a modular toilet shown in Figure 2.15(a). The toilet was printed in three parts and later assembled on site. Comparing to the conventional method of creating concrete structures, 3D concrete printing can reduce the material wastage and save production time, cost, and ultimately fetch sustainability in our built environment.

Geopolymers

3D printing with high volume fly ash is a challenge as the strength development in an early age is not quick enough to support subsequent layers. To avoid this problem, fly ash was activated with an alkali solution according to geopolymerization mechanism [43]. Figure 2.15(b) shows an example 3D printing of geopolymer mortar extruded through a rectangular orifice of a 4-axis gantry printer. To enhance the reaction process, 5-10% slag, which is also regarded as one of the by-products of steel power plant industries, was used [44].

Figure 2.15. (a) 3D printing of modular toilet with high volume fly ash at SC3DP, NTU. (b) 3D printing of geopolymer [44].

Recycled glass aggregates

Despite the abundant supply of sand from the desert or the seabed, the world is facing a shortage of construction sand. This is mainly due to the nature of the desert sand and sea sand are not suitable for applications in construction, thus, mainly river sands are used in the construction industry. Hence, with the limited resource for construction sand, an alternative solution is needed to meet the increasing demand for construction materials. Singapore generates over 70,000 tons of glass waste annually, of which only less than 20% is being recycled [45]. The remaining waste glass is usually disposed of in landfill where it is not suitable due to its non-

biodegradable nature. The study of replacing river sand by the recycled glass in cementitious materials has been established for decades.

At SC3DP, NTU the research on using recycled glass aggregates for 3D concrete printing focuses on the formulation of mix design and the effect of recycled glass aggregate gradation on printability [46]. The comparison of the river sand and recycled glass aggregates was studied to evaluate the printability performance of the materials [35]. The gradation study of the recycled glass particles was also conducted to optimize the material performance for 3D concrete printing application. Furthermore, the alkali-silica reaction which is a commonly known issue in the recycled glass aggregates is currently being investigated.

2.3 Properties of printable construction materials

Concrete is a heterogeneous material that is strong in compression and weak in tension. It is a composite material and is obtained by mixing cementitious materials, aggregate and water. It can be considered as a two-phase discontinued system material represented by aggregate particles dispersed in the cement paste matrix [47]. The rheological behaviour of concrete mixtures varies between two extremes during its fresh-state for pumpable behaviour and no-slump behaviour.

Pumping of concrete is a complex study that involves several parameters. Segregation, lubricating layer, the excess paste in the concrete and the required pump pressure are some of the parameters that need to be addressed before concrete can be pumped. A certain pressure gradient is necessary to move the concrete in the hose [48]. When experiencing high pressure, if the mix lacks mortar and does not deform readily, the particle interference and high friction could lead to segregation and cause

hose blockage as shown in Figure 2.16. When segregation occurs, the aggregate particles interlock, which causes the lubricating layer to be lost and stops the concrete from moving. Segregation is usually associated with mixtures having inadequate particle size distribution or with excessive water-to-cement ratio [49].

Several researchers reported that the lubricating layer formed between the concrete and the inner wall of the hose is an important parameter for concrete pumping [50]–[52]. The shear-induced particle migration was reportedly to contributes to the formation of the slip layer. According to Ngo et al. [53], the constituents composing the slip layer are water, cement and fine sane with a size lesser than 0.25mm. This lubricating layer thickness is proportional to the volume of cement paste, water-to-cement ratio and the dosage of superplasticizer.

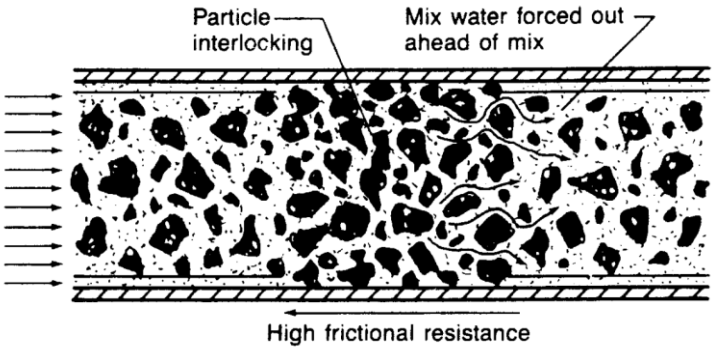

Figure 2.16: Segregation of water in pipe flow causing aggregate to interlock [49]

On the other hand, no-slump concrete is a mixture that has little deformation but has proper compaction after demolding or extrusion. Low water content attributes to this shape preservation ability. In 3D extrusion printing, shape preservation after extrusion from the nozzle is important as any slump could cause dimensional inaccuracy in the final printed structure. The correlation among mix composition,

deformability, pumpability and compaction is closely related. In order for mixtures to be no-slump and pumpable, not only does it need to have sufficient paste for flowability in the pipe, internal shear resistance needs to be high after extrusion for no-slump capabilities.

As the technology of 3D concrete printing starts to gain traction in recent years, many different printable mix design also starts to show in the literature. Table 2.1 shows the mix design from different institute working on 3D concrete printing. It is observed from the table that the commonly used raw material are cement (CEM 1 type), fine sand, fly ash, silica fume and limestone filler. While the materials obtianed by different institute is suitable for printing, their performance in terms of compressive strength is vastly different. The strength of the material depends not only on the hydration of the cemetitous paste, it also depend on the morphology of the interface between cementitious paste and the agregates. In this case, the printing parameter which can affect the arrangement of the material is crucial.

Table 2.1: Printable mix design from other publications [[20], [41], [54]–[57]]

Institute / Company	University of Southern California	Yonsei University	TU Dresden	Loughborough University	University of Southern Brittany	XtreeE SAS	American University of Beirut
Main binder	CEM II type cement (C/B: 1)	CEM I type cement (C/B: 0.6) Fly Ash (FA/B: 0.3) Silica Fume (SF/B: 0.1)	CEM I type cement (C/B: 0.55) Fly Ash (FA/B: 0.23) Silica Fume (SF/B: 0.22)	CEM I type cement (C/B: 0.7) Fly Ash (FA/B: 0.2) Silica Fume (SF/B: 0.1)	CEM I type cement (C/B: 0.5) Limestone filler (LS/B: 0.25) Kaolin clay (KC/B:0.25)	CEM I type cement (C/B: 0.6 - 0.8) Limestone filler (LS/B: 0.1 - 0.2) Silica Fume (SF/B: 0.1 - 0.2)	Cement (C/B: 1) (unknown type)
Fine aggregate/ Sand	S/B: 1.105	fine aggregate and silica sand (0.1mm to 0.6mm)	S/B: 1.5897	S/B: 1.5 (Maximum particle size 2mm)	NIL	S/B: 0.8 - 1 (crystalline silica)	S/B: 1.92 (combination of fine aggregate and sand)
Water	W/B: 0.505	W/B: 0.35	W/B: 0.23	W/B: 0.26	W/B: 0.205	W/B: 0.2 - 0.233	W/B: 0.39
Plasticizer / Superplasticizer	SP/B: 0.084	NIL	SP/B: 0.0128	SP/B: 0.01 Retarder/B: 0.005	SP/B: 0.0015	NIL	Acclerator /B: ~ 0.008 Retarder/B: ~ 0.005
Other Materials / Remarks	NIL	3mm fibers polysaccharide type thickening agent (0.1% of binder weight) styren-acrylic polymer resin (0.1% of binder weight	NIL	1.2 kg/m3 of 12mm length/ 0.18 mm diameter polypropylene fibres	Limestone filler had a particle size distribution ranging from 0.1 to 100 micron	NIL	NIL
Average compressive strength (Mpa)	18.9 Mpa	52 Mpa	80Mpa @ 21days	110 Mpa	no harden test result	Estimated compressive strength (120Mpa) from flexural strenght (14.2Mpa @ 90 days)	42 Mpa

From the review of existing literature, it was observed that a few benchmarking properties are required for printing. These benchmarking properties were consolidated into three main properties that are needed for cementitious material to be printable.

Pumpability is related to the concrete extrusion and workability, as it is important for 3D printing to ensure that the materials have a continuous easy-flowing behaviour from the source to the printing nozzle. Pumpability ensures the materials

can be pumped easily and continuously without creating clogging issues inside the delivery system (e.g. nozzle and hose).

Buildability is the resistance of a material to deform under loading of the subsequent layers. After each layer is extruded from the nozzle, the layer should be able to support its own weight and withstand the subsequent layer with little or no deformation (e.g. no-slump). Low buildability is caused by low yield stress of the materials. High paste content in the mixture could be one of the reasons for low yield stress and this may cause the material to deform under loading and each layer width to be larger than intended.

Layer adhesiveness is a very important aspect of concrete printing as it would affect the structural integrity of the fabrication part. The bond between layers has to be high in order to withstand the shearing load caused by an environmental factor. This all relates to the curing dynamics of the concrete so that it is relatively easy to extrude yet viscous enough to hold together and adhesive enough to create an integrated structural result. Current research has lag on the study of the bonding between concrete layers and understanding this aspect could allow us to improve the structural integrity [3].

2.3.1 The role of aggregates in concrete printing

Aggregates in concrete fulfil two main objectives - economy and strength. Aggregates are cheap and provide as a good filler. Morphology of the aggregates has significant influences on engineering properties of granular materials [58]. Concrete made with angular and rough particles usually needs to have higher mortar content to be pumpable. Aggregates composed of spherical shape with smooth surface

texture create a lower degree of particle-to-particle interlock than angular particles which is generally good for workability in concrete. However, a material having good workability alone is not suitable for printing. Other than workability, for it to hold its shape after extrusion, the material needs high yield stress. In hardened concrete, angular and irregular shapes with rough surface texture aggregates have a greater surface area for bonding with cement paste and have better interlocking between aggregate particle thus have higher strength. Therefore, non-spherical and rough texture aggregates are preferred [58].

Other factors such as the maximum size and the gradation of particle sizes can also affect the concrete pumpability. The maximum size of the aggregates should be at least 4 to 5 times smaller than the hose diameter. As the hose gets smaller, more mortar paste is required. A 75 mm hose will require a mix containing 58% mortar while a 50 mm hose will require 60% mortar [59]. In this study, the maximum allowable size of aggregates is limited to 2.3 mm due to the limitation of the pump and the hose (25 mm).

2.3.2 The role of paste in concrete printing

The mixture of the cementitious material and water forms the paste in the concrete. The production of every pound of Portland cement generates and release around one pound of carbon dioxide to the atmosphere [60]. Sustainability is a concern since concrete being the most widely used material [61] uses cement as a binder to bind the aggregates. Hence, pozzolanic materials were introduced (slag, fly ash, silica fume) as replacements for cement in concrete to control the emission of carbon dioxide. Pozzolan are defined as materials that possess little or no

cementitious value but can chemically react with calcium hydroxide in the presence of moisture form compounds having cementitious properties.

Reduction of carbon emissions is not the only benefit when replacing cement with pozzolan. Introducing pozzolans such as fly ash to a concrete mixture can improve durability and workability, reduce early heat of hydration, and often increase later age strength resulting in a longer lifespan of the structure [62]. As important as direct savings, there are also indirect savings such as resource preservation and reduced pollution through emissions and landfill space to be considered [62].

Fly ash is a by-product that is a non-combustible mineral portion of coal, produced during the burning of coal in a power plant. Figure 2.17 shows the scanning electron microscope (SEM) image of a single fly-ash. As a production waste, this material is normally used for landfills and its price is much lower than the cost of Portland cement [62]. Some of the benefits of this material include better control of temperature rise in mass concrete to reduce thermal cracking; improves the durability of the concrete; increase workability; reduce bleeding; increase stability against segregation; delay setting time; improves later age strength when fly ash content is below 20% [62]. It reacts with the by-product of cement hydrate (lime) to create additional calcium-silicate-hydrates crystals which adds to the strength of concrete. As recommended by previous literature, fly ash should not be more than 72 kg per cubic meter of concrete [59].

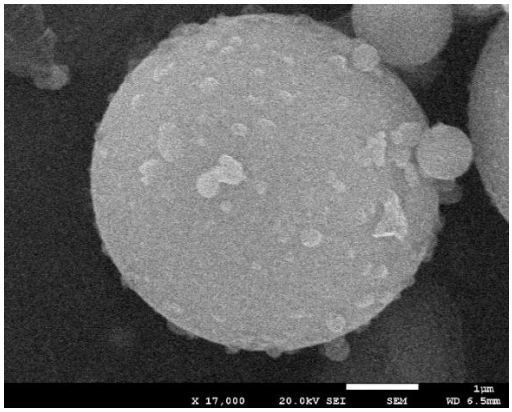

Figure 2.17: Scanning electron microscope (SEM) image of a fly-ash.

Silica fume is another pozzolanic material that is a by-product from the production of silicon metal and ferrosilicon alloys. This by-product is in a very fine powder-form consisting of mainly spherical particles or microsphere of around 0.15 micron and has a very high specific surface area [62]. When it is used in concrete, an increase in the silica fume content in the mixture increases the water demand of concrete to maintain the same workability. This increase in water demand is primarily caused by the high surface area of the silica fume. Some of the other benefits of using silica fume are promoting cohesion and reducing segregation in the concrete; reducing bleeding in concrete; reducing cracking due to lower heat output during hydration. Figure 2.18 shows the SEM image of the silica fume used.

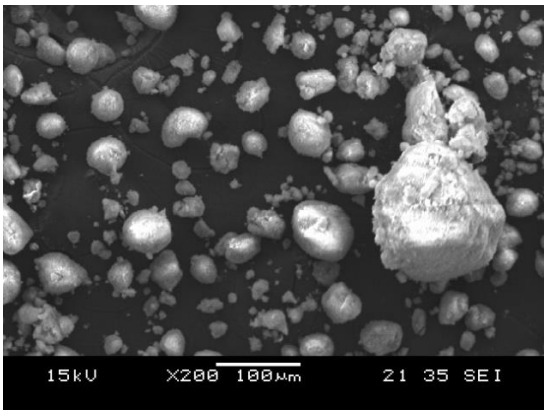

Figure 2.18: Scanning electron microscope (SEM) image of silica fume.

The presence of the particle in a Newtonian fluid, induce a change to the flow characteristics of the reported. In the presence of a low volume fraction of suspended particles, the fluid is assumed to behave like a Newtonian fluid with a higher viscosity than the interstitial fluid. By increasing the volume fraction of suspended particles, the behaviour of the system gradually changes from Newtonian to a shear rate dependent behaviour [63].

A paste exhibits a continuous network of soft interactions throughout the interstitial fluid is sufficiently high to change the behaviour from that of a suspension [64]. According to Hoornahad [65], paste consistency is characterized by the yield stress of the paste. Pastes can show elastic and viscoelastic behaviour. When the shear stress remains below the yield stress of a material, it remains in an elastic behaviour. As soon as the applied force is released, the initial configuration of the articles is restored. As the shear stress moves beyond the yield stress, the configuration of the particles is irreversibly broken, and the material starts flowing showing a viscoelastic behaviour. The rheological properties of cementitious paste are crucial to its flow characteristics and can be described by the Bingham model, with its two parameters: yield stress and plastic viscosity. Both parameters can affect the pumping behaviour of fresh concrete [50]. Furthermore, plastic viscosity is very important in estimating the resistance of concrete to flow in the pipe since this parameter is a measure of the change in shear stress with a change in shear rate [51].

According to Kennedy [66], there are two types of paste in a mixture: void paste and excess paste as shown in Figure 2.19. This is the fundamental theory on the close relation between paste and aggregate and its contribution to workability. The void paste is the paste that fills up the void space between the aggregates, this

void paste acts like glue to hold the aggregates together and keeps them in place. The excess paste is the layer of paste surrounding every particle in mixture with a constant thickness. This excess paste helps in the flow of the aggregates and reduces internal friction as it pushes the aggregates apart. More excess paste layer will increase the flowability of the mixture [66]. Deformability of fresh concrete is the ease of being deformed by gravity and external forces and yield stress is one of the governing parameters for deformability. Deformability of the mixture increases with the increasing volume fraction of the excess paste and consistency of the paste [67].

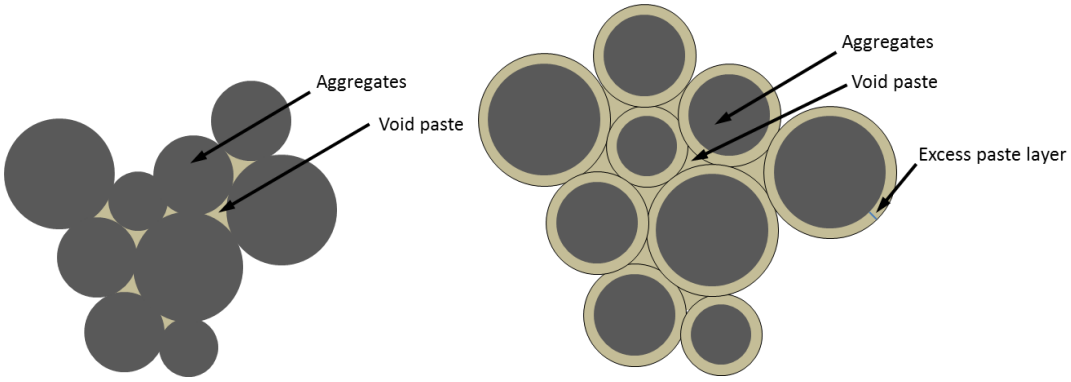

Figure 2.19: Mixture of aggregates and paste

2.4 Challenges of concrete printing with the current technology

2.4.1 Bond strength of concrete layers

The interlayer bond strength have been mention by a few researchers that it is the weakest part in the printed structure [57], [68]. The bond interface adhesion characteristics of two concrete layers can be divided into mechanical interaction and chemical bonding [69]. In concrete repair research, the analyses on the bonding and fracture mechanics of a hardened and fresh concrete reveal that a clean and rough

surface on the substrate is required for the repair material to bond well [69]. The bond between old and fresh concrete has been widely investigated. On the contrary, there is little research on the bond interface between two fresh concrete before the emergence of 3D concrete printing due to its limited application [70].

The material parameters and printing parameters such as the aggregates size, material composition, printing flow rate, printing travel speed and printing time gap can have a significant influence on the final 3D printed objects [7], [70]. It is reported by Zareiyan and Khoshnevis [70] that using smaller aggregate size and lower aggregate to cement ratio yields higher tensile strength. According to Paul et al. [68], the strength of printed concrete is anisotropic and the tensile strength is stronger in the direction parallel to its printed direction than the strength perpendicular to its printed direction. The low strength is usually caused by the weak bonds in-between the printed filament at the interfacial material shown in Figure 2.20 [43]. Studies that have been carried out in relation to this anisotropic phenomenon revolve mainly around the mechanical properties of the printed concrete in its hardened state [43], [70], [71].

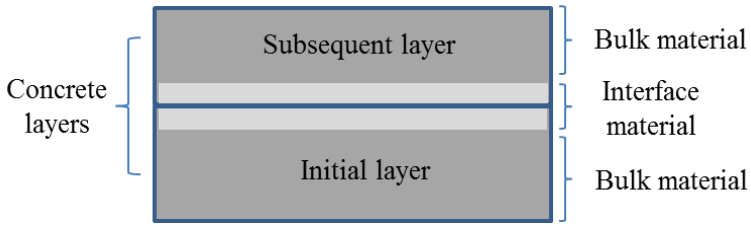

Figure 2.20: Cross-section of the printed filament

2.4.2 Printing of supports in concrete printing

The existing technology that is used to print the overhanging structure for the extrusion-based technique are examined and classified into three main categories. In order to 3D print overhanging structures without changing part orientation, fabrication of support underneath is inevitable. These sacrificial materials enable the overhanging segment to be integrated with the main structure instead of connecting modular parts.

Printing over an existing surface

To print over an existing surface, the nozzle must follow the contour of the surface after they are mapped out prior printing. In most cases, this support is placed manually. Figure 2.21 shows a structure printed with an overhanging design. A support structure is erected to hold the subsequent layers as shown in Figure 2.21(a). Printing over a flat existing surface, such as a re-useable plank can be a cheap solution. However, since 3D printing can be used to print more complex structure, which may not necessarily be a flat surface, this existing surface support needs to be tailored according to the design. The tailoring of the complex surface support is time-consuming and the labour intensive. Furthermore, the placement of support is disruptive to the printing process. This disruption can cause a longer time gap between the subsequent layer and the current layer where the support is added. Tay et al. [72] investigated the influence of time gap on the strength of the inter-bond layer and result revealed that a time gap of more than 5-minutes will have a significant decrease in the tensile strength at the inter-bond layer. Depending on the complexity of the overhang, a longer time gap can be expected and will further reduce

the bond strength. After printing, the support scaffolding cannot be removed until the material gains sufficient strength.

The support-less roof shown in Figure 2.22, inspired by ancient methods, is an example of constructing a support-less closed structure and was proposed by Khoshnevis [73]. The idea of this technique was borrowed from the vault construction, where bricks and mortar were used to construct parabolic-shaped roof at an angle approximately 20° to perpendicular along the longitudinal axis of the vault as reported by Dahmen and Ochsendorfs [74]. This angle allows the prior section of the roof to support successive sections without the need for formwork. Such technique integrates the supporting system with the main structure. By building the roof with this parabolic-shape, the arrangement of the bricks enables the structure to be in compression. However, this parabolic shape does not benefit 3D concrete printing as the material extruded is still in its fresh state. The successive layer needs to be supported by the prior layer at an inclination of more than 20° to perpendicular along the longitudinal axis for the material to be stable during the printing process. With the adoption of such technique, rapid hardening property of the material is expected so that the load of the subsequent layer can be supported by the previous layer which is also an overhanging structure.

Printing of supports with a support material

Generally, the generation of support starts by determining if the surface requires support. Strano et al. [75] explained that once a surface requires support, the support geometry is computed and is usually printed with a weak infill pattern. Some fused filament fabrication (FFF) (See Figure 2.23) and jetting-based additive

manufacturing technique use a dual-nozzle printer to print with primary material and support material. The primary material is defined as the material used to print the main structure. The support material, on the other hand, is a temporary structure to be removed during post-process. Stansbury et al. [76] presented a Multijet printing method that utilized a UV-curable material to produce smooth parts in highly complex geometry, wax or other gel-like support material that can be co-deposited for subsequent removal by heating. On the other hand, Fahad et al. [77] utilized a different property for the support material. For FFF technique, support material such as polyvinyl alcohol, PVA, a water-soluble thermoplastic is used as it can be dissolved in water. For jetting-based technique, support material such as propylene glycols is preferred as the high temperature is used to melt the support material. These printing techniques are usually used to print multi-piece assembly which careful consideration is given to the accessibility of the residual material between components. The dissolving and melting of the support materials also reduce the possibility of feature damage due to human error. In 3D concrete printing, Kaufhlod et al. [78] developed a sustainable support material with raw material such as native starch and wood flour which can be recycled after used. According to Kaufhlod, this recyclable perspective is the justification for the material savings and ecological friendliness of the building process. Although the results show potential in the use of such material, the support material was never validated with a prototype.

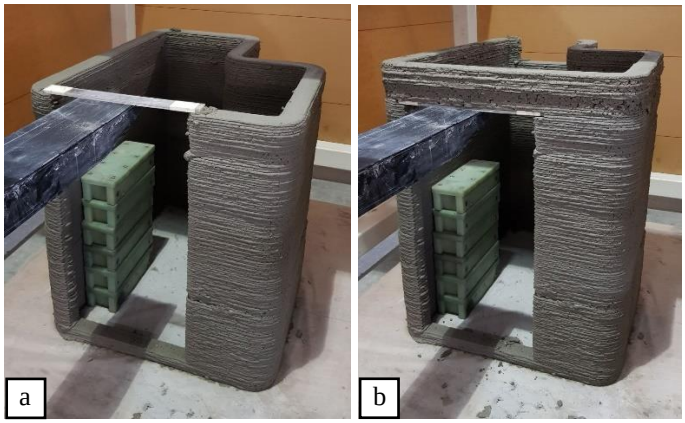

Figure 2.21: Printing of overhangs over existing support (a) manual insertion of support (b) printing over existing support.

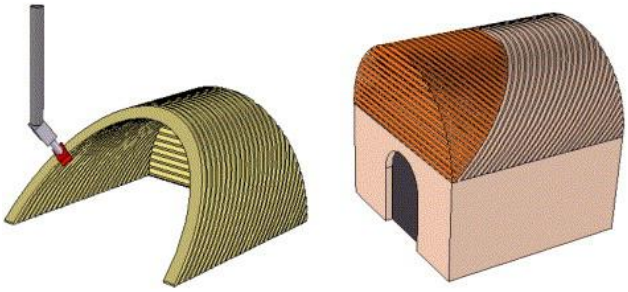

Figure 2.22: Contour crafting approach to fabricate support-less structures [19]

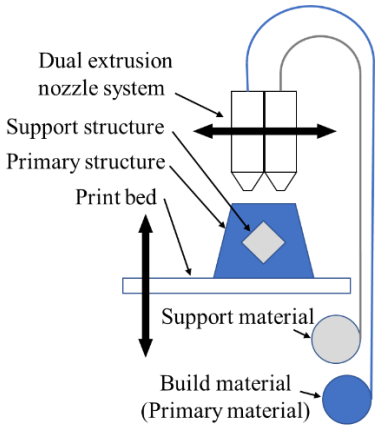

Figure 2.23: FFF dual nozzle system to print with support material

No printer setup with multiple materials has been reported in 3D concrete printing. However, using two robots to print a single piece structure was demonstrated as shown in Figure 2.10 by Zhang et al. [37]. Each robot printer is

attached to its own pump to print collaboratively. Although the materials used in the study are both primary material, support material such as clay can be put into one of the robots to create the support structure. With this configuration, high precision on the robot control is necessary to prevent any collision and to ensure communication on the exact location for the support and primary material is properly executed. The use of two or more nozzle increases the complexity of the printing system drastically. Nevertheless, mortar is generally a cheap material to use. Thus, if the cost of the support material is higher than the primary material, it could potentially drive up the overall cost of manufacturing the component.

Printing of supports with the primary material

Using the primary material to print support structures for the "overhanging" problem has already been investigated in many publications with different solutions being proposed for the FFF technique. Dumas et al. [79] exploited the ability of FFF printers to print bridges across gaps. Points to support for the overhangs were selected and optimised to print scaffolding composed of bridges and vertical pillars. Vanek et al. [80] optimised the framework to reduce the amount of support structure required which resulted in the support structure to have a tree-like shape that effectively supports the overhangs. In general, the support structures fill the free space beneath the overhang in a densely or truss-like manner. The differences between the literature are the quantity, suitability and reliability of the material used. Different support geometries were proposed to reduce the material wastage and reduce the contact point between the support structure and the main structure to improve surface finish. Printing of chamfers support without vertical structures was demonstrated by Cacace

et al. [81], however, the proposed technique was designed for FFF and the material used has a rapid hardening property.

Concrete printing, on the contrary, is a brittle material and requires curing time. It is not possible to print truss-like supports with concrete material because the gap distance is too far apart and may result in the main layer to slump. The study done by Tay et al. [72] has shown that a good mechanical mix at the interbond layer is important. Even though fast curing concrete may be able to achieve low slump with far gap distance support, if the curing or the stiffening time of the material is too rapid, it will weaken the bonding between the main layers.

Another approach for printing supports with the primary material is to vary the printing parameters. Although the support and the main structure may be the same material, the material properties extruded at different parameters will not be the same. Carneiro et al. [82] characterized the printed specimen mechanically through varying the printing parameters. The objective is to print the support structure with a lower strength that can be easily removed during post-processing. To the best knowledge of the author, there has been no literature which investigates the use of concrete as a feasible support material for concrete printing.

In the following section, an experimental method for obtaining the optimized values of the printing parameters for different printing region will be presented. Two different print paths will be used to correlate the effect of the travel speed and the flow rate on the dimensional precision of the filament. Also, investigation on the dimensional parameters such as the top surface area of the filament and the slump in the bridging layer is carried out. Furthermore, through experimental analysis and designing appropriate benchmarks, the printing parameters are calibrated to print

different types of filament for different structures (primary structure and support structure). The results obtained will be verified by printing an overhanging beam. Finally, the advantages and limitations of this technique will be discussed.

2.4.3 Functionally graded material (FGM)

Limited by the conventional manufacturing technique and the cost to create freeform structures, the existing beam and column that are topologically optimized are not common. Optimized geometrical complexity adds value to the structural component in terms of material saving. This improves the strength-to-weight ratio. Material saving can also help to reduce unnecessary load-bearing requirements from the structural elements [83]. Alteration to the formwork using the conventional method to create material saving elements requires additional time and money which can ultimately lose the incentive to optimize the structure.

Functionally graded concrete material

Jeffery et al. [84] conducted an experiment to study the fracture behaviour of functionally graded concrete material (FGCM) for rigid pavement. Plain cement concrete (PCC) and fibre-reinforced concrete (FRC) were used to fabricate four different configurations of functionally layered concrete materials. The configurations are PCC-PCC, PCC-FRC, FRC-PCC and FRC-FRC with the first mixture on the top and the second mixture on the bottom. Three-point bending test is used to characterize the fracture behaviour of the samples with different configurations. According to Jeffery et al. [84], application of FGCM for rigid pavement shows promising results in terms of fracture test and numerical modelling.

It was observed that concrete specimens with FRC have an improved residual strength or softening behaviour over pure PCC specimen. Hence, by having layers within concrete pavement surface with the specific function will achieve higher performance at a lower cost.

Nazari and Sanjayan [85] conducted an experiment to understand how different volume percentages of a functionally graded geopolymer made by two different geopolymer mixtures affect the compressive strength. In contrast to the production method by Jeffery et.al, there is a transition phase between the two geopolymer layers instead of having two distinct layers. According to their results obtained, all the FGG specimens have achieved higher compressive strength than anticipated. It is concluded that the position of the functionally graded layer and the thickness of the constituent layers can affect the strength of these specimens.

Oxman et al. [86] designed and produced a rapid fabrication apparatus to vary the properties of the cellular material as shown in Figure 2.24. The work focuses on cementitious foam material where the density is controlled by the reaction of the aluminium powder and lime to produce hydrogen gas bubbles. The results show that a graded beam with 9% less mass can support the same load as a solid beam with the same size.

Figure 2.24: Radial and linear density gradient of concrete samples [86]

Functionally graded printed material

Leu et al. [87] used a Freeze-form extrusion (FEF) method to fabricate a 3D printed functionally graded material. An extruder was designed with three individual plungers that consist of different pastes. This development of the extruder is the proof-of-concept for a triple-nozzle system to allow the different material composition to be printed. The triple-extruder FEF system was able to mix multiple aqueous pastes according to the required mix composition by varying the plungers' velocities. This extruded mixed paste can be used to fabricate 3D functionally graded parts layer-by-layer with the desired material gradient as shown in Figure 2.25.

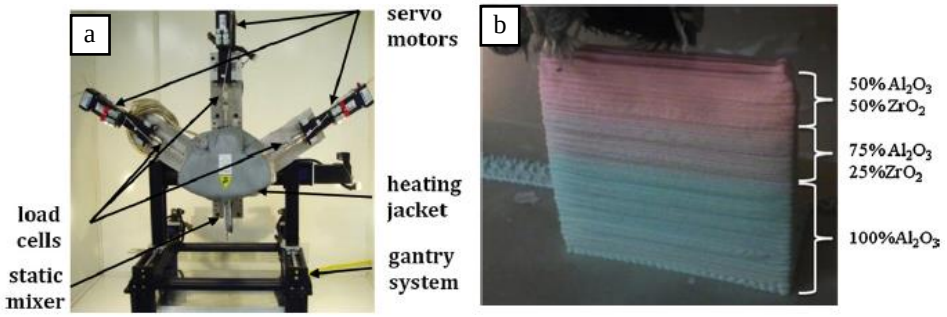

Figure 2.25: Functionally graded material with different material composition [87]

However, the main challenge is the coordination between the three plungers to maintain a consistent flow at the end of the nozzle. If any of the plungers are not synchronize, breakage or overflow may occur.

Rashid et al. [88] conducted an experiment to study how topology optimized printed metal beam fair against a regular solid beam under a three-point bend test. In order to create a complex optimized structure, a case study of a simple bending beam was made. Two topology optimized structures were generated using a modified topology optimization algorithm as shown in Figure 2.26.

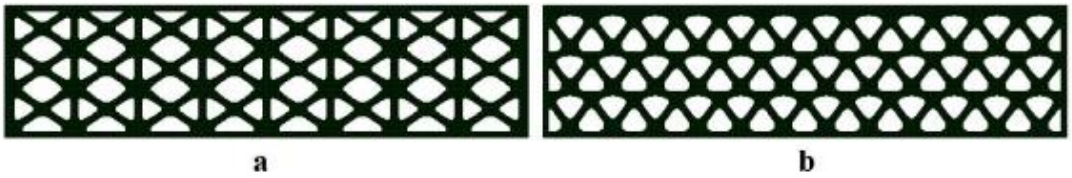

Figure 2.26: (a) 8x3 periodic lattice topology optimization design
(b) 12x3 periodic lattice topology optimization design [88]

A three-point bending test was conducted on these two structures and the results were compared to a regular solid beam. Based on the results, a graph of flexural load and displacement was plotted as shown in Figure 2.27. It was found that the optimized lattice unit beam absorbed more energy per unit volume as compared to the solid beam. The reason was that the fracture occurs one after another along the loading direction which allows more energy to be absorbed by the links before complete failure while the sold beam fail almost instantaneously with the initial crack [88]. The use of optimized lattice units could potentially open up an avenue to improve the strength-to-weight ratio of a component by replacing a solid material with it [88].

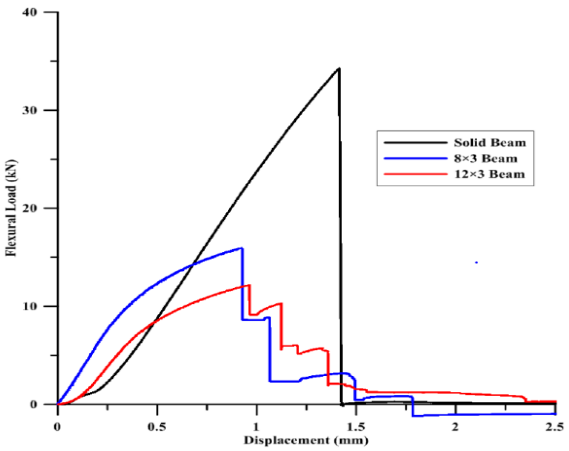

Figure 2.27: Load vs displacement graph [88]

Martens et al. [89] present work on optimizing 3D printed concrete structures. The research incorporates the orthotropic properties of the printed concrete and the manufacturing constraint of the 3D concrete printer is taken into consideration for the topology optimisation algorithm. This adoption of topology optimisation in concrete structure can save material which can potentially create sustainable and cost-efficient structures [89]. However, his investigation only introduces the methodology and algorithm to optimize the structure for stiffness and the work proposes was not validated with actual printing.

Most existing literature presented work that creates a functionally graded material by altering the material properties through intermixing with another material. However, with the aid of 3D printing, A concrete structure with spatially varying microstructure for optimal structure efficiency and maximum strength-to-weight ratio can be created. This can be achieved by adjusting either its volume flow rate or travel speed at a specific portion of the printing process. To the best knowledge of the author, this approach has never been done for concrete material.

2.5 Chapter summary

This chapter presents the background knowledge on the materials as well as systems used in the field of 3D concrete printing. Furthermore, the savings on the passive design created by 3D concrete printing cannot be neglected. This propels the motivation to explore the use of 3D concrete printing. Addition of green material to the mixture can further improve the suitability impact of the technology.

In this dissertation, river sand was chosen as the aggregates used in this research because of its non-spherical rough texture properties. This allows better

interlocking for buildability purpose. The size of the aggregates is limited to 2.3 mm due to the specification of the delivery system. Additionally, the fresh concrete is considered as a two-phase discontinued system material represented by aggregate particles dispersed in the cement paste matrix. The rheological behaviour of this heterogeneous type of materials depends on the local interaction between the mix components. This mixture can exhibit rheological behaviour close to that of either paste or granular systems, depending on the composition. The main challenge associated with 3D concrete printing is to develop appropriate material that can be extruded continuously and stacked up over one another without causing any deformation in the bottom bead layers.

Furthermore, the existing challenges of concrete printing such as interlayer bond strength, supports in concrete printing and printing of FGCM are some of the motivation for this desertion. The printing parameter such as material flow rate and nozzle travel speed are key parameters to these challenges and further indepth examination will be dissuss in the following chapters.

Chapter 3: Printability region of concrete material in 3D printing

3.1 Introduction

The flowability of concrete material is commonly characterised by the Bingham model, where dynamic yield stress and plastic viscosity are obtained. It corresponds to the steady-state after strong continuous shear. During a continuous shear, the microstructure is broken thus decreasing the shear stress [9]. In the case of concrete and mortar, the presence of sand and gravel further break down the microstructure during shearing [90]. The dynamic yield stress is described as the shear stress needed to sustain the flow, while the static yield stress is the shear stress needed to initiate the flow. Thixotropy is thought to be the origin of the discrepancy between static and dynamic yield stress [91].

Saak et al. [92] and Roussel [93] have attempted to correlate the slump and flow diameter results to the yield stress of the cement paste. The result shows that the fundamental relationship between yield stress and slump is material independent and largely independent of the cone geometry. On the other hand, the flow table test may not correlate with the yield stress of the material tested. Nevertheless, this test seems to be able to provide a cheap, simple and rather precise measurement of the yield stress of self-compacting concrete (SCC). Marchment et al. [94] present some work using the flow table. He tested the flow diameter at a different time interval and found that the flow of the material reduces with time. The main observation from the results shows that paste mixtures with additives slow the stiffening effects of cement to maintain a malleable bond interface. Ravindra et al. [95] used a flow table test to determine the consistence of the mortar. It is important as it enables a practical assessment of the degree of workability and the quantity of water required to obtain

adequate plasticity. The result shows that an increase in the fine recycled aggregates would lead to a reduction in consistence. This decrease in the consistence is mostly due to the water absorption of the aggregates.

Pumpability and buildability are the main crucial material parameters in concrete printing that relate to the plastic viscosity and the yield stress of the material. Pumpability, as defined in Section 2.3, is the ease of transporting the material from the reservoir to the nozzle. Pumping of concrete material is a complex process. Besides its time-dependent material behaviour, changes in the concrete properties due to pumping conditions such as bleeding and segregation can cause the pumpability of the material hard to predict [96]. Separation of the paste from the aggregates can lead to blockage of the hose. This phenomenon is usually caused by deficient particle size distribution or excessive water-to-binder ratio [97]. In a properly designed mixture, there should be sufficient surplus paste content to fill the voids between the aggregates. This paste content forms a coating wrapping the aggregates which serves as a “lubricant” between the aggregates when shear stress is applied to the mixture [98].

On the other hand, buildability, which has been recently defined and used for 3D concrete printing applications [42], [56], is dependent on the yield stress of the material, structural build-up of the material, and the shape stability of the cross-sectional shape of the layers. The static yield stress of the material gives the material its initial rigidity. This rigidity, which is related to the initial shape retention capability after extrusion from the nozzle, is required before the structural build-up of the mixture comes into effect. The structural build-up of the material depends on the rate of flocculation and hydration of the binders [99]. If the deposition of the

subsequent layer is faster than the structural build-up rate of the material, the structure will fail [56]. The balance between the structural build-up of the material and the printing parameters is important to achieve high buildability. Addition of admixtures such as accelerators can improve the material structural build-up rate [8]. Furthermore, shape retention capability after extrusion can give an indication on the material's buildability. Without the use of formwork, the material depends on its internal cohesion between the paste and the aggregates. In order for the material to retain its shape after extrusion and be able to sustain the load of subsequent layers, the high static yield stress of the material is required.

Currently, there is no standard test method used to measure or quantify pumpability and buildability for 3D printing. Existing research has proposed various mixtures by using rheometers for measuring dynamic yield stress and plastic viscosity in 3D concrete printing [68], [100]. However, these measurements with the rheometer are sensitive to the protocols as well as data processing if non-standardized measuring geometries are used, which can cause results to vary [101]–[103]. Hence, a field-friendly test such as the slump and flow table tests are used for characterisation.

The slump test in this study uses a cone-shaped mould as described in ASTM standard [104]. After the material is poured into this mould, this mould is lifted. Material flow occurs if the shear stress generated by gravity inside the material is higher than the yield stress of the material. The slump value is the height of slump after the mould is lifted up. This shear stress caused by the gravity decrease with the thickness of the material as it flows. If the stress generated by the gravity becomes smaller than the material yield stress, the flow stops. This slump in the material is

therefore directly linked to the yield stress of the tested material [105]. The area of the slumped material over the surface was also determined. After dropping for 25 times, the material spreads out on the plate and the diameter is measured as the flow diameter values. It could be regarded that dropping for 25 times makes the difference in the mixtures corresponding to the microstructural breakdown. Thus, the slump value is more related to the solid-state of the microstructure and static yield stress and buildability. The flow diameter value is related to dynamic yield stress and pumpability. In most cases, the slumped area was circular, indicating a uniform deformation throughout the material. The area at the base is called the slump spread or flow diameter. Such measurement technique is usually used for evaluation of self-compacting concrete (SCC) due to the low yield stress of such materials [106].

In this chapter, the investigation of the slump and flow diameter results will be used to evaluate the pumpability and the buildability of the mixtures. Parameters such as water-to-binder ratio, sand-to-binder ratio, fly ash to binder ratio and silica fume to binder ratio are used for analysis. Additionally, pumpability index and surface quality index will be introduced to examine the material characteristics. Furthermore, this investigation aims to map out the printable and non-printable regions for mortar in the slump and flow diameter diagram in order to evaluate the material suitability for 3D concrete printing.

3.2 Methodology

3.2.1 Mix design and preparation method

From Table 2.1, it is observed that most of the researcher in the literature use fine sand, CEM 1 type cement, fly ash, limestone filler and silica fume in their

mixtures. It is also observed that the fly ash and limestone filler is not used in combination. For the experiment results to be consistent, the raw material and the preparation methods have to be the same. In this dissertation, Ordinary Portland Cement (OPC, ASTM Type 1, Grade 42.5), silica fume (Undensified, Elkem), fly ash (Class F) and river sand was used. For the material to be delivered by the progressive cavity pump (Mai Pictor), the maximum particle size of the sand aggregates has to be lesser than 2 mm. This pump is coupled with a 10L rotor-stator and the hose has an inner diameter of 25.4 mm. The fineness modulus (FM) of the sieved river sand is 2.19, where fine aggregates generally have FM ranging from 2 to 4.

Four parameters such as water-to-binder ratio (W/B), sand to binder ratio (S/B), fly ash to binder ratio (FA/B) and silica fume to binder ratio (SF/B) were evaluated for their significance to slump and flow diameter value. In order to select the significant parameters, a full factorial design experiment was carried out. The values of the factors were selected based on existing literature from Portland Cement Association [107], [108] as well as the printable mixtures from Table 2.1. After the significance of the effects was determined from the results, effects that have relatively lower significance were fixed with a constant value. The second set of experiments are then established by varying the significant effects to systematically map out the printable region in the slump and flow diameter diagram. Additional 3D printing tests with a gantry printer were carried out to verify the printable region in the slump and flow diameter diagram established with the second set of experiment. The factors with the low level (-1) and high level (+1) are shown in Table 3.1. Figure

3.1 shows the cumulative percentage passing and the individual percentage retained results of the raw material by the particle size analyser (Malvern Mastersizer).

Table 3.1: Factors and their levels

Effects	Abbreviation	Symbol	Variable levels	
			-1	+1
Water/ binder ratio	W/B	W	0.45	0.55
Sand/ binder ratio	S/B	S	1.20	2.00
Fly ash/ binder ratio	FA/B	FA	0.10	0.30
Silica fume/ binder ratio	SF/B	SF	0.08	0.12

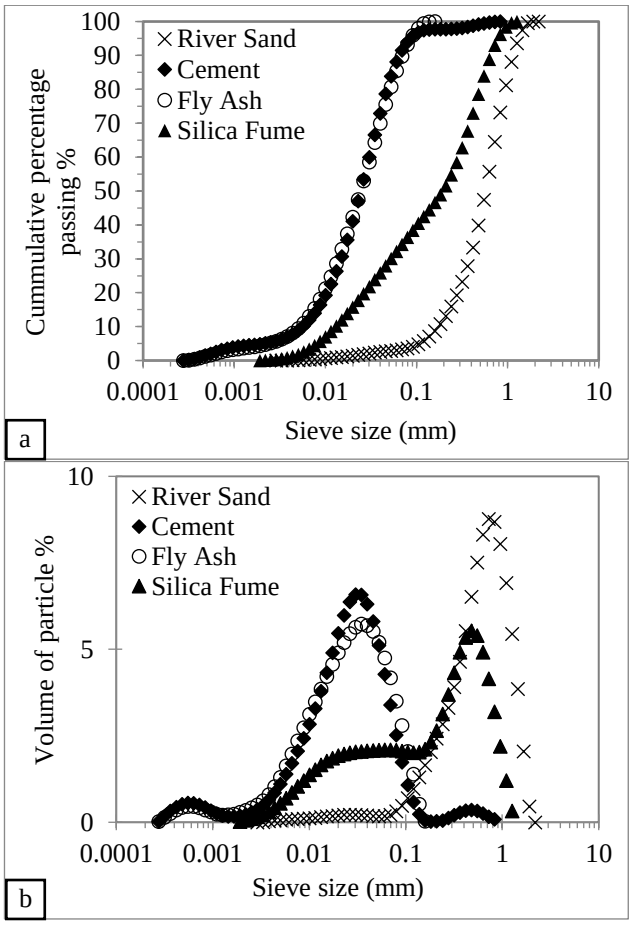

Figure 3.1: (a) Cumulative percentage passing of raw material; (b) Individual percentage retained of raw material

A Hobart mixer was used to prepare the material. Dry components were dry-mixed at 59 rpm for 5 minutes. Water is then added to the mixture for mixing at slow-speed (59 rpm) for 1 minute and follow by 7-minutes of high-speed mixing (198 rpm). After mixing, the material is used immediately for either testing or printing.

3.2.2 Slump and flow table test

A conical mould, as shown in Figure 3.2, in accordance with the ASTM C230 [104] was used for the slump tests. The slump test procedure starts by filling half of the mould with mortar. It was tamped 20 times to assure uniform distribution over the cross-section of the mortar. More mortar is filled to the brim of the mould and is tamped as specified for the first half. Excess material is removed by drawing the edge of a trowel with a sawing motion. Subsequently, the mould is removed and the difference in the height is recorded as the slump value. Figure 3.2 shows the setup of the flow table test and the specification follows ASTM C1437 [109]. The preparation protocol of the mortar for the flow table test, which follows ASTM C230 [104], is similar to the slump test. After the mould is removed, the flow table is dropped 25 times and the diameter of the mortar is recorded. Both the slump and flow diameter values for the different mixtures will be mapped out to determine the material region for printability.

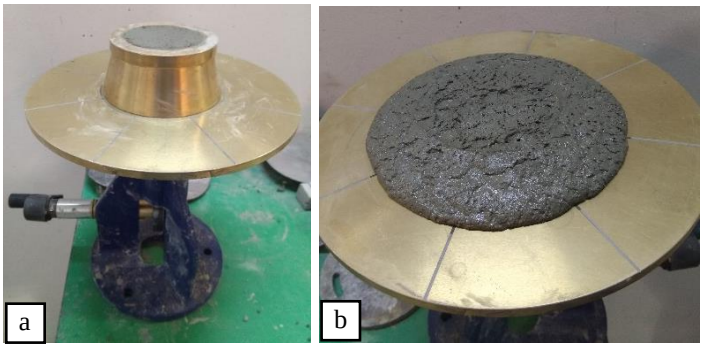

Figure 3.2: Flow table test experimental setup (a) before the mould is removed (b) the spread of the material after dropping the table for 25 times.

3.2.3 Pumping and printing test

A progressive cavity pump (Mai Pictor) with a 10L rotor-stator (MAI-Rotor/Stator 10L) as shown in Figure 3.3 is the material delivery system. The pumping speed and the dimension of the rotor-stator such as the rotor pitch determine the flow rate of the material. A pumping flow rate test is used to quantify the pumpability of different mixtures. This test measures the weight of each mixture being delivered through the pump at a constant speed of 2890 rpm for 30 seconds. The measured weight and density of the mixtures are used to calculate the flow rate in volume per second (ml/s). A pumpability index, which is the ratio of the flow rate of the mixture and that of water, is introduced to characterize the pumpability of the mixture. Material that has high pumpability index could achieve a flow rate at a slower pump speed as compared to material that has a low pumpability index.

Figure 3.3: Progressive cavity pump

In order to compare the results between various mixtures, the printing parameters such as flow rate, travel speed, layer height and printing path must be consistent. The flow rate of all mixtures was adjusted by controlling the pump speed before printing. A cylinder structure with a diameter of 150 mm and a layer height of 15 mm, a travel speed of 60 mm/s with a flow rate of 23 ml/s are the printing parameter preset for this experiment. Existing literature has used the maximum number of layers printed before collapsing as an indicator for buildability [57]. In this investigation, the cylinders are printed continuously using the gantry printer until they collapse. This relative comparison is a practical method to determine the mixture that has high yield stress for buildability. The surface quality and the maximum number of layers printed were compared between different mixtures.

3.2.4 Surface quality index

An imaging software (ImageJ) was used to analyses the photos obtained from the experiment. It measures the amount of abnormality in the printed structure as shown in Figure 3.4. Three different area of 150 by 150 pixel were randomly selected on the printed structure for each printed mixture. Each of these selected areas captures the abnormality by detecting the dark spots. Figure 3.4 shows the original photo and the filtered photo of the different mixture. The average of the three values obtained is the structure's abnormality surface area. In order to correlate the data obtained, a dimensionless surface quality index is introduced. The surface quality index is the ratio of the abnormality surface area in the sample with the worst surface finish to the abnormality surface area of each structure. Higher surface quality index means lesser abnormality on the surface of the structure.

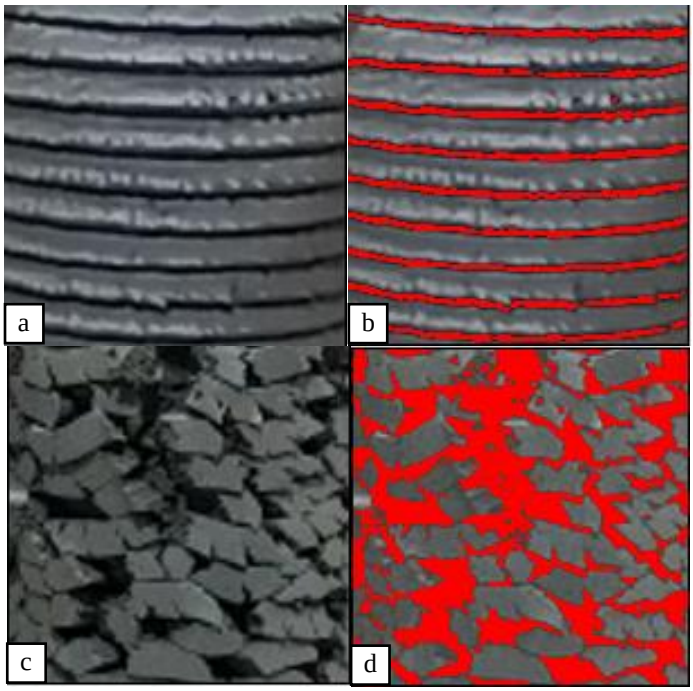

Figure 3.4: (a) Original photo of Mix 8 (b) Filtered photo of Mix 8
(c) Original photo of Mix 21L (d) Filtered photo of Mix 21L

3.3 Results

3.3.1 Full factorial design experiment analysis

A full-factorial design for 4 factors with 2 levels is shown in Table 3.2. There are only 4 factors thus resulting in 16 mix design for this full factorial design. It measures the responses of every possible combination of the factors and levels. These responses are analysed to provide information about the main effect and the interaction effect. The slump and flow diameter average results are also shown in the right column of Table 3.2.

Table 3.2: Slump and flow diameter result.

Runs	Factors (coded values)				Results	
	W	S	FA	SF	Slump (mm)	Flow diameter (mm)
1	-1	-1	-1	-1	4.2	158
2	1	-1	-1	-1	10.2	212
3	-1	1	-1	-1	0.5	112
4	1	1	-1	-1	5.3	183
5	-1	-1	1	-1	3.1	167
6	1	-1	1	-1	7.5	209
7	-1	1	1	-1	0.5	111
8	1	1	1	-1	3.8	152
9	-1	-1	-1	1	2.1	147
10	1	-1	-1	1	6.5	186
11	-1	1	-1	1	0.2	113
12	1	1	-1	1	3.1	153
13	-1	-1	1	1	2.3	138
14	1	-1	1	1	6.2	184
15	-1	1	1	1	0.0	108
16	1	1	1	1	2.0	152

The results obtained from the full factorial design were evaluated by ANOVA (analysis of variance) at 5% significance level shown in Table 3.3 and Table 3.4. The F-value determines if the source of variation is significant. If the F-values of the source of variation is large, it means the source of variation has a large significance. The F-values of W and S are 116.84 and 81.89 respectively as shown in Table 3.3. These values are significantly higher than the other F-values for the slump test. Similarly, the F-values of W and S for the flow table test are significantly higher than those of other parameters. Additionally, the P-value is used to weigh the strength of the evidence, which helps to determine the significance of the result. Small P-values indicate that there is strong evidence that a factor is significant. The P-value of W and S in both slump and flow table test are less than 0.001. This means that assuming the W and S have no effect, the observed difference will be obtained in less than 0.01% of studies due to random sampling error. This means that compared with the other two parameters the W and S, which are water-to-binder ratio W/B and sand-to-binder ratio S/B, have a higher effect on the slump and flow table test. The interaction between the main effects has significantly lower F-values. This means that the different type of material interacting with each other is not significant.

Table 3.3: Analysis of variance (ANOVA) table for slump result

Source of variation	Degree of freedom	Sum of Square	Mean Square	F-Value	P-Value
W	1	125.73	125.73	116.84	<0.001
S	1	88.12	88.12	81.89	<0.001
FA	1	5.58	5.58	5.19	0.037
SF	1	20.21	20.21	18.78	0.001
W*S	1	3.80	3.80	3.53	0.078
W*FA	1	2.41	2.41	2.24	0.154

W*SF	1	3.85	3.85	3.58	0.077
S*FA	1	0.13	0.13	0.12	0.734
S*SF	1	1.16	1.16	1.08	0.314
FA*SF	1	1.92	1.92	1.78	0.200
W*S*FA	1	0.01	0.01	0.01	0.925
W*S*SF	1	0.16	0.16	0.14	0.709
W*FA*SF	1	0.35	0.35	0.33	0.575
S*FA*SF	1	1.43	1.43	1.33	0.266
W*S*FA*SF	1	0.04	0.04	0.03	0.854
Error	16	17.22	1.08		
Total	31	272.11			

3.3.2 Slump and flow diameter

The 16 slump and flow diameter results obtained in Table 3.2 were plotted on the slump and flow diameter diagram shown in Figure 3.5. The relationship between the slump and flow diameter values could be fitted into a trend line. Additionally, 8 mixtures that are labelled in Figure 3.5 show the extreme region of the material characteristics on the diagram. Through the experimental observation, the four data points (run3, run 7, run 11 and run15) on the bottom left of Figure 3.5 are too stiff and are not flowable. These mixtures show low values of the slump and flow diameter. They have low values of W/B and high values of S/B. It could be reasoned that a high volume fraction of the aggregates could result in high internal friction between the aggregates thus resisting flow [110]. On the other hand, mixtures that have a high level of W/B and a low level of S/B have a high slump and flow diameter values. Run 2, run 6, run 10 and run 14 slump and flow diameter values were found to be more than 6 mm and 180 mm respectively. With a higher volume fraction of water content, the aggregates in the mixture have a lesser tenancy to interact. This reduces the internal friction thus resulting in higher flowability [64].

Table 3.4: Analysis of variance (ANOVA) table for the flow table test result

Source of variation	Degree of freedom	Sum of Square	Mean Square	F-Value	P-Value
W	1	17907.80	17907.80	91.85	<0.001
S	1	12521.50	12521.50	64.22	<0.001
FA	1	225.80	225.80	1.16	0.298
SF	1	1906.50	1906.50	9.78	0.007
W*S	1	26.30	26.30	0.13	0.718
W*FA	1	124.00	124.00	0.64	0.437
W*SF	1	185.30	185.30	0.95	0.344
S*FA	1	132.00	132.00	0.68	0.423
S*SF	1	427.80	427.80	2.19	0.158
FA*SF	1	13.80	13.80	0.07	0.794
W*S*FA	1	57.80	57.80	0.30	0.594
W*S*SF	1	34.00	34.00	0.17	0.682
W*FA*SF	1	331.50	331.50	1.70	0.211
S*FA*SF	1	225.80	225.80	1.16	0.298
W*S*FA*SF	1	30.00	30.00	0.15	0.700
Error	16	3119.50	195.00		
Total	31	37269.50			

While the full factorial design result obtained is sufficient to prove that W/B and S/B have a more significant effect than FA/B and SF/B, this result is not sufficient to illustrate the printable region of the material. Furthermore, the results obtained from the factorial design do not show a good scatter of the data points as shown in Figure 3.5. Intermediate level of the significant effects is therefore required to show a good scatter of data points on the slump and flow diameter diagram. In order to systematically map out the printable region in the slump and flow diameter diagram, another series of mix design experiment that encompasses small increment at different intervals is carried out.

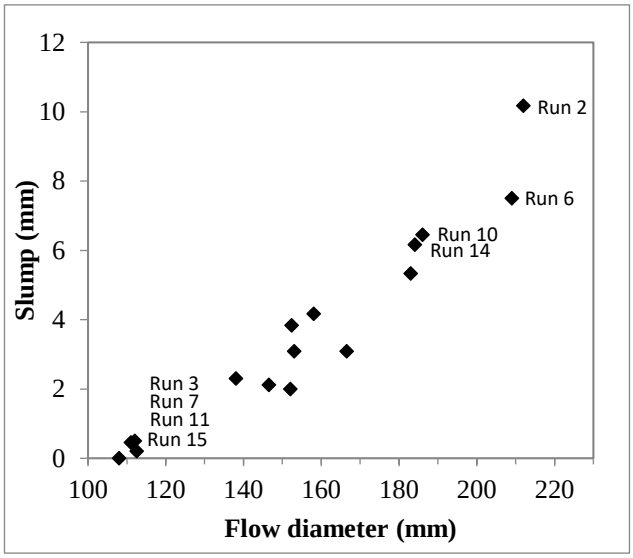

Figure 3.5: Slump and flow diameter results obtained from the factorial design experiment

Table 3.5 shows the additional series of experiment to increase the scatter of data on the slump and flow diameter diagram. Mix 8 to Mix 23 have a fixed FA/B and SF/B content since these two parameters have a lower impact on the slump and flow table test. Furthermore, to reduce the possibility of low flow diameter, the S/B was reduced to a range of 0.8 to 1.6. Similarly, to reduce the possibility of a high slump, the W/B was reduced to a range of 0.4 to 0.5. These ranges were selected based on the factorial design experiment. Additionally, Mix 1 to Mix 7 were selected to increase the scatter of the data points on the slump and flow diameter diagram that is not achievable when FA/B is 0.3 and SF/B is 0.06.

Table 3.5: Mix design to map out the printable material region

<table>
<tr><td></td><td colspan="6">Mixture composition</td></tr>
<tr><td></td><td>W/B</td><td>S/B</td><td>FA/B</td><td>SF/B</td><td>Slump (mm)</td><td>Flow diameter (mm)</td></tr>
<tr><td>Mix 1</td><td>0.40</td><td rowspan="11">0.80</td><td>0.00</td><td>0.13</td><td>4.67</td><td>154</td></tr>
<tr><td>Mix 2</td><td rowspan="2">0.41</td><td rowspan="2">0.39</td><td>0.12</td><td>4.00</td><td>143</td></tr>
<tr><td>Mix 3</td><td>0.10</td><td>5.70</td><td>149</td></tr>
<tr><td>Mix 4</td><td rowspan="2">0.42</td><td>0.33</td><td rowspan="19">0.06</td><td>7.38</td><td>182</td></tr>
<tr><td>Mix 5</td><td>0.37</td><td>7.16</td><td>175</td></tr>
<tr><td>Mix 6</td><td>0.40</td><td rowspan="2">0.40</td><td>5.11</td><td>159</td></tr>
<tr><td>Mix 7</td><td>0.46</td><td>9.56</td><td>193</td></tr>
<tr><td>Mix 8</td><td>0.40</td><td rowspan="15">0.30</td><td>5.94</td><td>169</td></tr>
<tr><td>Mix 9</td><td>0.43</td><td>8.61</td><td>189</td></tr>
<tr><td>Mix 10</td><td>0.46</td><td>10.66</td><td>200</td></tr>
<tr><td>Mix 11</td><td>0.50</td><td>12.78</td><td>212</td></tr>
<tr><td>Mix 12</td><td>0.40</td><td rowspan="4">1.00</td><td>4.56</td><td>162</td></tr>
<tr><td>Mix 13</td><td>0.43</td><td>5.89</td><td>177</td></tr>
<tr><td>Mix 14</td><td>0.46</td><td>6.67</td><td>191</td></tr>
<tr><td>Mix 15</td><td>0.50</td><td>9.89</td><td>213</td></tr>
<tr><td>Mix 16</td><td>0.40</td><td rowspan="4">1.30</td><td>2.94</td><td>135</td></tr>
<tr><td>Mix 17</td><td>0.43</td><td>4.72</td><td>160</td></tr>
<tr><td>Mix 18</td><td>0.46</td><td>5.61</td><td>174</td></tr>
<tr><td>Mix 19</td><td>0.50</td><td>8.94</td><td>203</td></tr>
<tr><td>Mix 20</td><td>0.40</td><td rowspan="4">1.60</td><td>0.00</td><td>112</td></tr>
<tr><td>Mix 21</td><td>0.43</td><td>2.42</td><td>136</td></tr>
<tr><td>Mix 22</td><td>0.46</td><td>3.28</td><td>146</td></tr>
<tr><td>Mix 23</td><td>0.50</td><td>6.28</td><td>182</td></tr>
</table>

From Figure 3.6, a trend similar to Figure 3.5 was observed. However, Figure 3.6 shows more scattered data points across the slump and flow diameter diagram as compared to Figure 3.5. With this good scatter of data points, it allows the classification of the printable region. It is observed in Figure 3.6 that with the increase in W/B or the reduction in S/B, the slump and flow diameter values increase. Increase in the volume fraction of the water content or the reduction in the aggregates volume

fraction can reduce the friction caused by the interaction between the interparticle which would increase the slump or flow diameter values.

The flow diameter value below 130 mm was too stiff to be smoothly pumped and the flow diameter value above 210 mm was too flowable to make a cohesive printed filament. With the reasoning above, it is decided that Mix 11, Mix 15 and Mix 20 are excluded from further analysis since these mixtures are not suitable for printing. This enables the study to focus on the materials that have a slump value between 2 mm and 12 mm and flow diameter values between 130 and 210 mm.

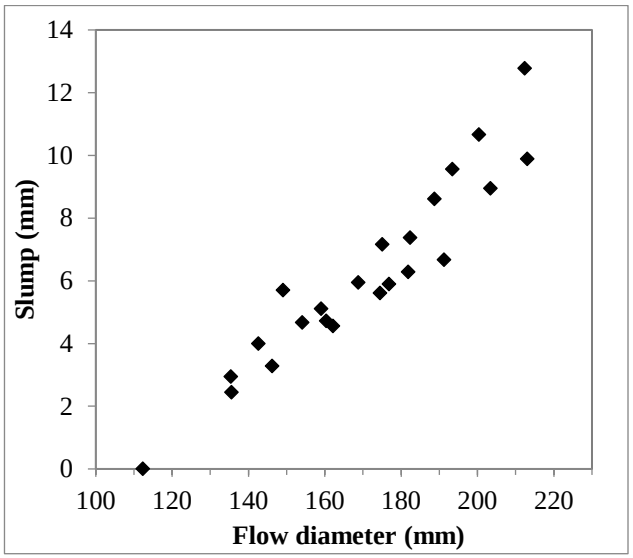

Figure 3.6: Slump and flow diameter values for mix design in Table 3.5.

Six data points were selected from the extreme ends in the region-of-interest for analysis, as shown in Figure 3.7. These six specimens were denoted by their mixture number and the two different regions L (lower region) and U (upper region) as shown in Figure 3.7.

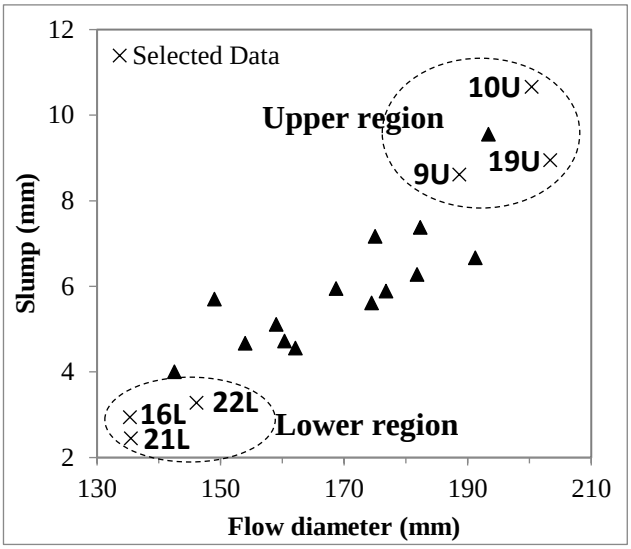

Figure 3.7: Slump and flow diameter separated into two regions with the mix number and region alphabet of selected mixture for further analysis.

3.3.4 Pumping flow rate

The blank bars in Figure 3.8 show the flow rate of the 6 selected samples and water that was tested with the delivery system. Comparing the selected sample with water gives an interesting insight into the difference of the pumpability of the viscous cementitious materials and Newtonian fluid. The different interaction between the particles in the mixture causes the difference in the flow rate. As seen from Figure 3.8, with the same pumping speed at 2890 rpm, different mixtures show different volumetric flow rate. In order to obtain a dimensionless parameter to characterise pumpability, a pumpability index is introduced to compare the pumpability of mixtures with the Newtonian fluid, i.e. water. The pumpability index is defined as the ratio of the flow rate of concrete to that of water at the pumping speed of 2890 rpm. It was observed in Figure 3.9 that the pumpability index is proportional to the flow diameter value of the samples.

In consideration that the flow rate would affect the size of the filaments after extrusion and printing quality [11], it is crucial to keep the flow rate consistent for all mixtures during printing for comparison. Therefore, pump speeds are adjusted for all the mixtures to make sure that they have the same flow rate of around 23 ml/s for extrusion and printing, as shown as the dark bars in Figure 3.8.

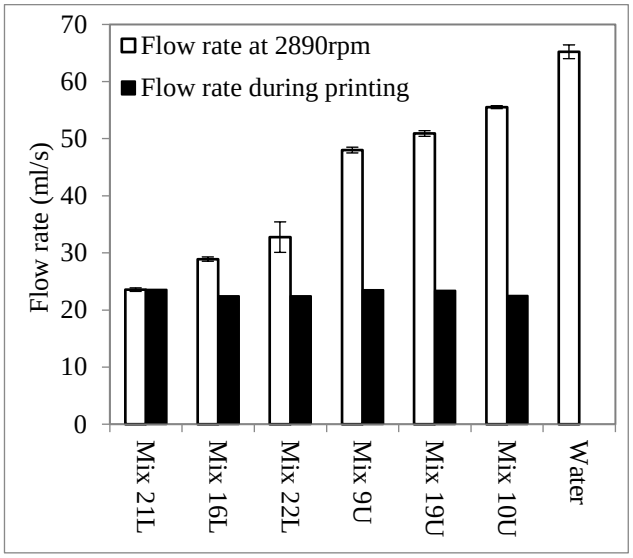

Figure 3.8: Pumping flow rate of different mix design

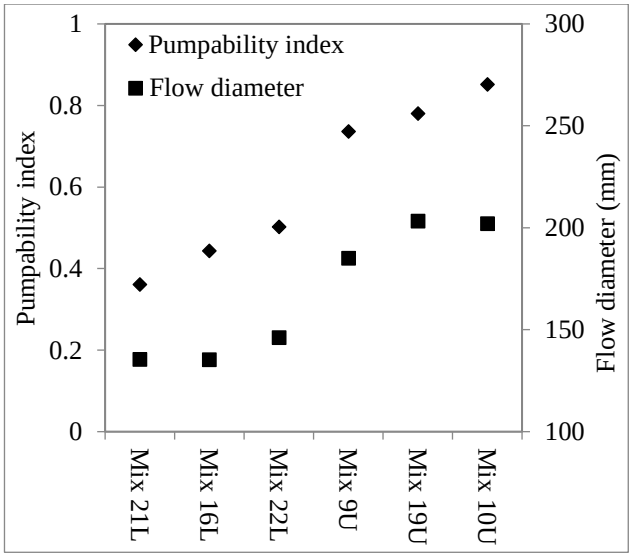

Figure 3.9: Pumpability index and flow diameter of the selected mixtures

3.3.5 Printing investigation

In order to illustrate the 3D printing performance of the mixtures in the lower and upper regions, cylinders using these mixtures are printed as shown in Figure 3.10. All of the selected mixtures are printed until the structures collapse. The photos shown in Figure 3.10 were the last layer of the printed cylinder before it collapse. The maximum heights of the structures are used to indicate the buildability of the mixtures.

Mixtures with low slump and flow diameter values appear to have a rough texture on the surface of the filaments as shown in Figure 3.10 (a)-(c). High shape retention, large voids/cracks and low pumpability index are some of the characteristics of such behaviour. Mix 21L and Mix 16L, as shown in Figure 3.10 (a) and (b) respectively, have a low pumpability index. These voids and cracks cause instability in the structure which eventually results in structural failure. Furthermore, it is notable that high material stiffness may result in lower interlayer bonding strength [72].

On the other hand, mixtures that have a high slump and flow diameter values appear to have a smooth surface and a lower amount of voids and cracks as shown in Figure 3.10 (d)-(f). Lower shape retention, smooth surface, high pumpability index are some characteristics of such behaviour. As the pumpability index increases, the maximum height that it can print reduces. Mix 19U and Mix 10U slump under its own weight within a few layers of printing. The internal cohesiveness of the material is not able to sustain the weight of the structure thus causing the material at the bottom layer to slump. This slump causes instability and eventually causes the structure to fail, as shown in Figure 3.10 (f).

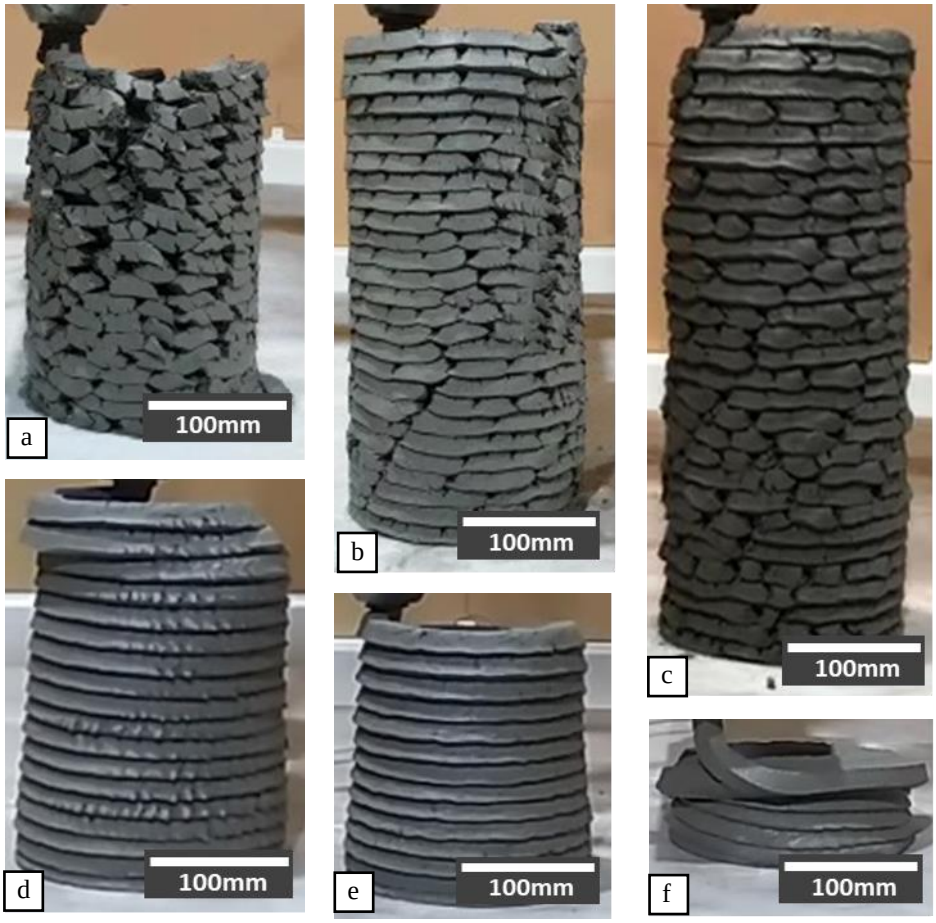

Figure 3.10: Maximum layers printed for different mixture
(a) Mix 21L; (b) Mix 16L; (c) Mix 22L; (d) Mix 9U; (e) Mix 19U; and (f) Mix 10U

Surface quality index is introduced to provide statistical analysis to the surface finishing of the printed structure. Figure 3.11 shows the surface quality index of the selected mixtures. Mix 10U was not included in the analysis because there are not enough layers printed for proper measurement of the surface quality. Nevertheless, the result shows that as the slump or slump values increase, the surface quality index increase.

From Figure 3.10 and Figure 3.11, Mix 21L, Mix 22L and Mix 16 L have too many abnormalities and the surface quality index value between them are close. This lower region is deemed as not suitable for printing. On the other hand, if the sample

does not have sufficient cohesion, it is not possible for a subsequent layer to be lay upon, therefore Mix 10U is also not suitable for printing.

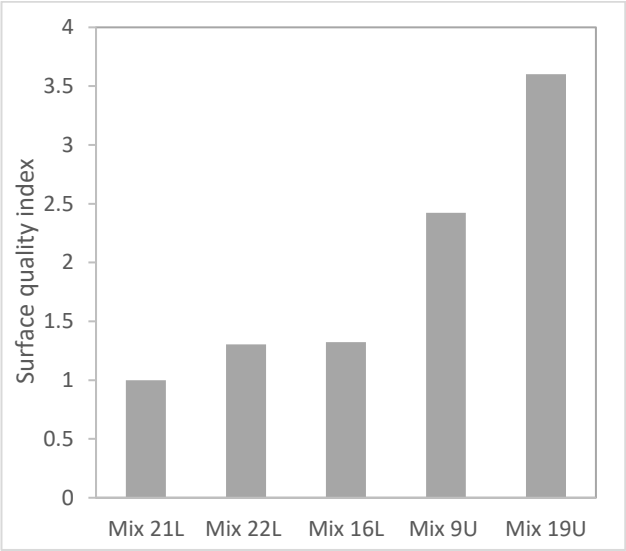

Figure 3.11: Surface quality index of the selected mixtures

On the other hand, Mix 9U and Mix 19U show good surface finish. Mix 9U and Mix 19U have an estimated 2.5 and 3.5 times lesser dark regions as compared to Mix 21L, respectively. However, due to the slow structural build-up rate, the maximum layers that can be printed for Mix 9U and Mix 19U are only 17 and 14, respectively. Depending on the required time frame of the project, the time gap of the printing parameters can be increased to match the structural build-up rate of these mixtures. However, it is not the optimal choice. Therefore, these mixtures are neither in the non-printable region nor the acceptable printing region.

Based on the observation above, the acceptable printing region should be within the area as shown in Figure 3.12, with the slump value ranges from 4 and 8 mm and the flow diameter value ranges between 150 and 190 mm.

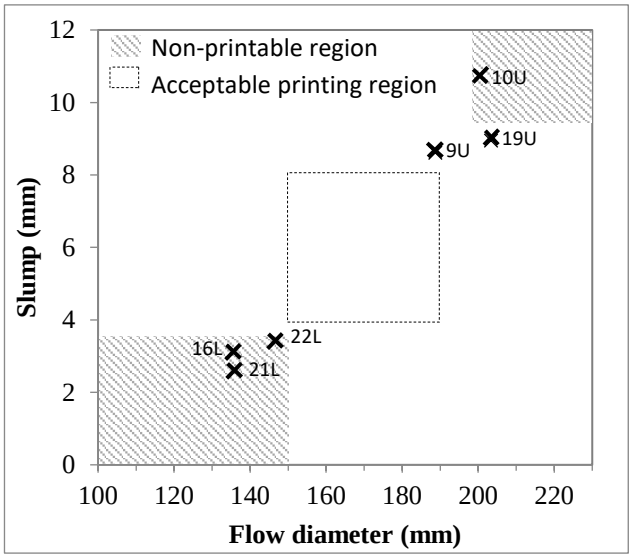

Figure 3.12: Printable and non-printable region on a slump/flow diameter graph

Figure 3.13 shows the correlation of the slump value, pumpability index and the maximum number of layers for each mixture. The trend of the pumpability index and the slump value appear to be correlated. For the lower region, the higher the pumpability index and flow diameter value, the higher the maximum number of layers are printed. In contrary, for the upper region, the lower the pumpability index and flow diameter value, the higher the maximum number of layers are printed. It could be reasoned that for the lower region, pores and discontinuity are the main reasons why the structure lost integrity and collapsed. In this case, the higher pumpability index helps to feed more material and less discontinuity, thus increasing the maximum height. In contrary, for the upper region, the high slump and low static yield stress make the structure unstable. These samples collapse due to the slump of the bottom layers. The material strength gain is insufficient to sustain the stress from the weight of the subsequent layers. Overall, it could be reasoned that an optimal region for high maximum height exists between the upper and lower regions. It seems

to justify the high buildability in the printable region in Figure 3.12. Further verification is going to be done in the next section.

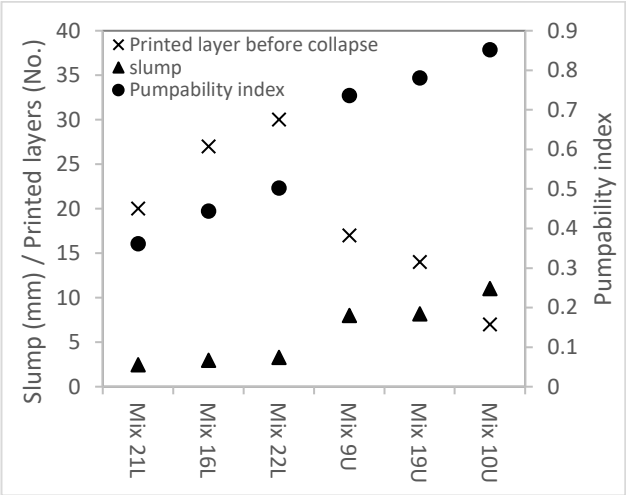

Figure 3.13: Slump, pumpability index and maximum printed layer before the collapse of selected mixtures.

Mix 22L and Mix 9U are near to the edge of the acceptable printing region. These two mixtures were used to examine the extreme region of a printable mixture. The slump of the bottom filament was recorded after each layer is deposited to examine the behaviour of the filament during actual printing. The 3rd filament from the bottom was used for analysis. The first two layers were not used for measurement to eliminate the possibility of uneven print-bed. A camera was used to capture the filament after each deposition of a layer. These photos were analysed with an image processing program (ImageJ) and the change in the slump of the filament was presented in Figure 3.14.

A stepwise response is observed on the thickness of the filament of Mix 22L due to the vertical stresses acting upon when subsequent layers are added. The filament is able to hold on to the same slump value for a few layers before slump and

subsequently holding on to the new slump value for the next few layers. This slump process increases the filament width, which increases the filament top surface area thus increases the yield point. On the other hand, Mix 9U, a mixture that has high slump and flow diameter values has a certain slump in the filament when each layer is deposited. The filament is not able to withstand the vertical stress acting on it thus its yields with every layer deposited.

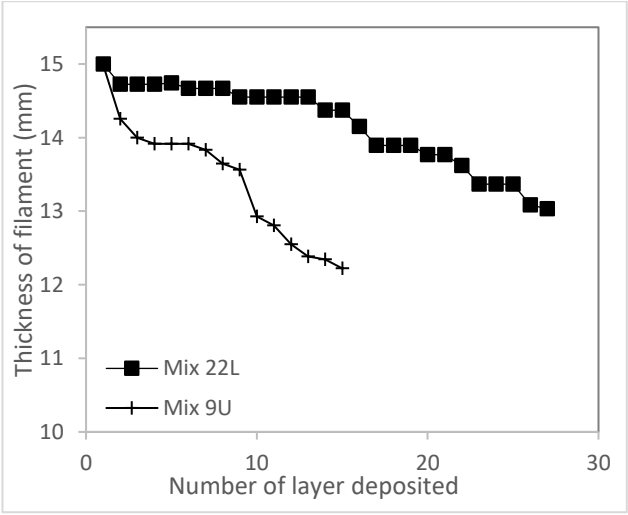

Figure 3.14: Change in the thickness of the third layer filament with every layer deposited

3.3.6 Validation of printable region

Since the mixtures are mainly controlled by the change in the W/B and S/B value due to their significant effect as proven in Section 3.3.1, it is observed that an increase in the W/B increase the slump and flow diameter values of the mixtures. On the other hand, an increase in the S/B reduces the slump and flow diameter values. All the results obtained appeared in between the two lines drawn. This causes an unreachable region as shown in Figure 3.15(a). Since this study does not consider

other materials such as accelerators or superplasticizer admixtures, these regions remain unreachable.

In order to verify the acceptable printing region described in Section 3.5, four mixtures (Mix 3, Mix 8, Mix 12 and Mix 23) were selected as shown in Figure 3.15. These four mixtures were selected because they are the extreme points within the acceptable and reachable printing region. Selecting mixture at the extreme points helps to characterise other mixtures within the region.

Table 3.6 shows the different results obtained in the order of increasing pumpability index. As anticipated, high flow diameter values correlated to high pumpability index. Within the acceptable printing region, the maximum number of layers printed is between 19 and 28, which is within the number of layers printed of 30 and 17 for Mix 22L and Mix 9U respectively. Similarly, the pumpability index in Table 3.6 is within the range of 0.5 to 0.7 for Mix 22L and Mix 9U respectively. This indicates that there is a trade-off between the pumpability and buildability and this region between the Mix 22L and Mix 9U is the zone to obtain the maximum pumpability and buildability.

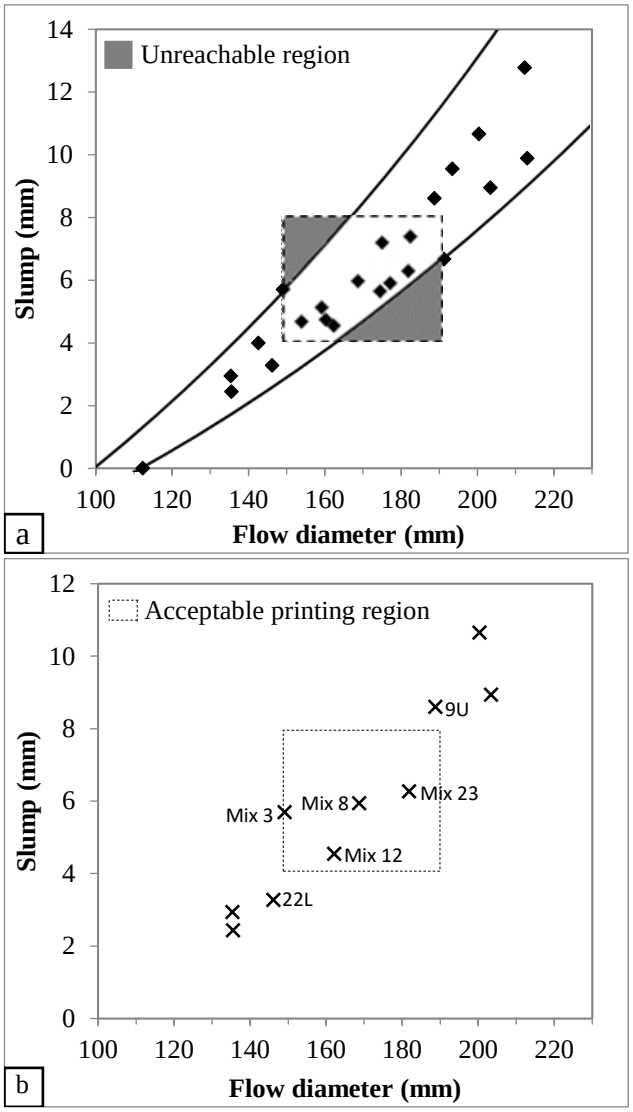

Figure 3.15: (a) Unreachable regions in the acceptable printing region

(b) Four mixture selected for verification

Table 3.6: Results obtained for the mixtures within acceptable printing region

	W/B	S/B	FA/B	SF/B	Slump (mm)	Flow diameter (mm)	Pumpability index	Max layer printed
Mix 3	0.41	0.80	0.39	0.10	5.70	149	0.52	28
Mix 12	0.4	1.0	0.30	0.06	4.56	162	0.53	26
Mix 8	0.4	0.8	0.30	0.06	5.94	169	0.65	19
Mix 23	0.5	1.6	0.30	0.06	6.28	182	0.67	22

Figure 3.16 shows the maximum number of layers printed for the different samples. Although the four samples are within the acceptable printing region, the surface finish of the samples varies to some extent. While the surface quality index results for these four mixtures were anticipated to be between the 1.3 and 2.5, all but one appeared inside of the range. Mix 8 shows better surface finish due to the absence of cracks and abnormalities found in other printed structure. Figure 3.17 shows the surface quality index as well as the pumpability index for all printed structure. Although there is no strong correlation between the surface finish and the pumpability index of the material, they show a similar upward trend.

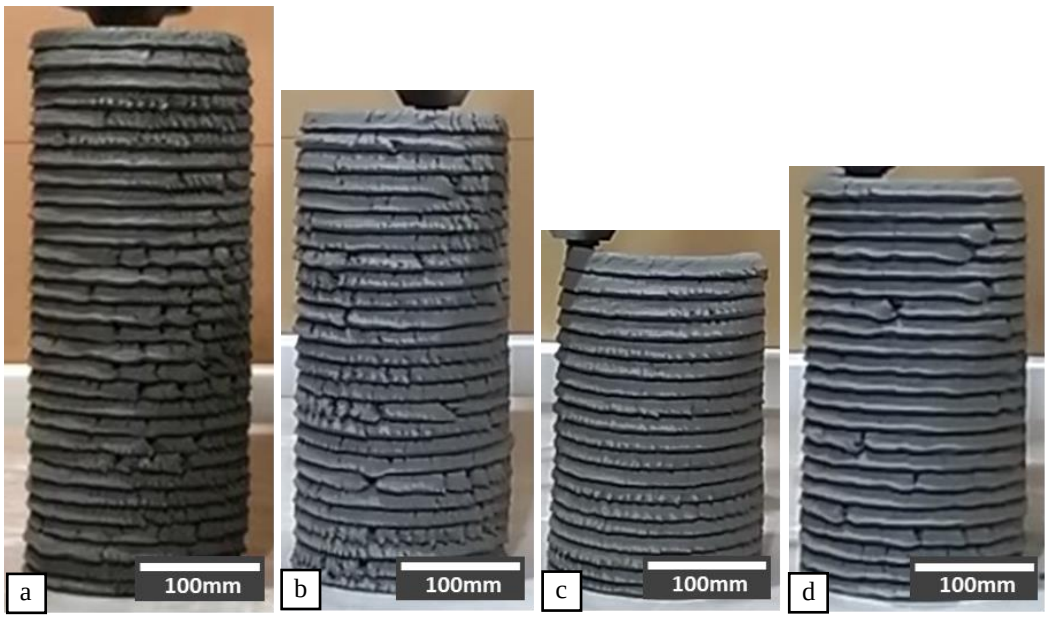

Figure 3.16: Maximum layers printed for the different mixture (a) Mix 3; (b) Mix 12; (c) Mix 8; and (d) Mix 23

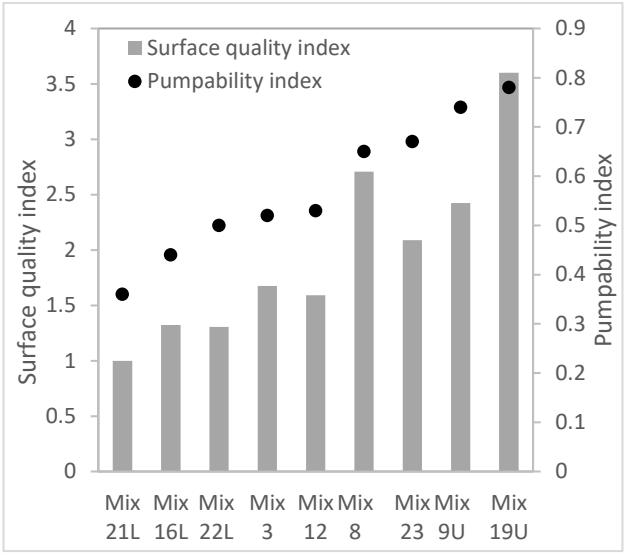

Figure 3.17: Surface quality index and pumpability index for all printed structure.

Figure 3.18 shows the deformation in the slump of the filament when each layer is added. A significant slump on the measured filaments was observed when the first layers were deposited above. This was a common trend for all mixtures. It is noticed that this slump is caused by stress-induced during deposition of the direct subsequent layer. Mixtures that have a low slump value is better at withstanding this initial slump. As the deposition of the layer progresses further, this additional stress is gradually reduced.

Mix 3 and Mix 12 exhibits a more solid-like behaviour when compared to Mix 8 and Mix 23. Similar to Mix 22L, this solid-like behaviour allows the mixture to support high vertical stress and can, therefore, be printed with more layer without slumping. On the other hand, Mix 8 and Mix 23 exhibit a more paste-like behaviour similar to Mix 9U.

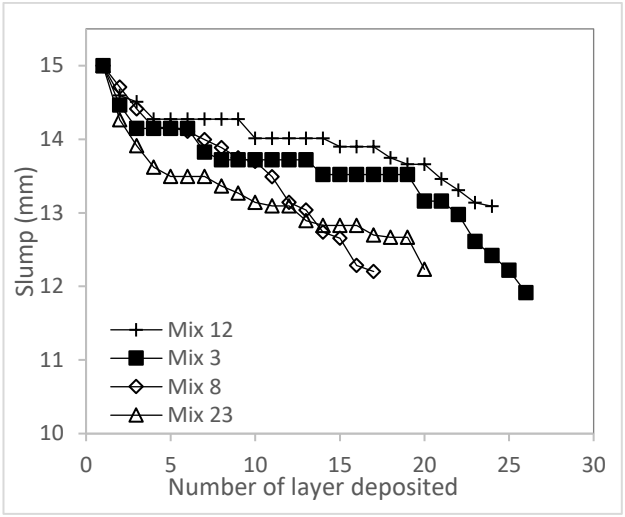

Figure 3.18: The slump of filament for the mixtures within acceptable printing region

Geopolymer, high-volume fly ash (HVFA) and recycled glass (RG) based printable material were used to validate the printability region as described in Figure 3.12. As shown in Figure 3.19, all the materials fall within the acceptable printing region. Figure 3.20 shows the structure printed with the respective material. These mixtures exhibit high pumpability and buildability properties, which therefore enable such structure to be printed. Further information on the individual material investigation can be found in the existing literature [35], [38], [44].

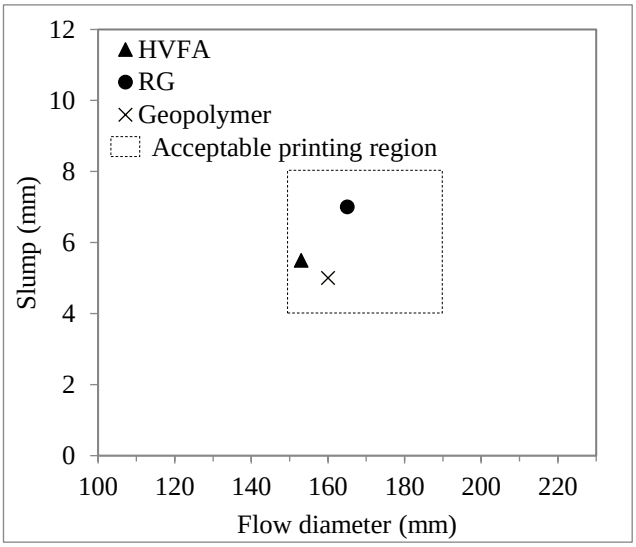

Figure 3.19. Verification of printability region with the material in the existing literature.

Figure 3.20. (a) A 60 layer structure printed with geopolymer mixture [44] (b) A toilet unit printed with high-volume fly ash mixture ((HVFA) (c) A vase structure printed with recycled glass (RG) mixture.

3.5 Discussion

Buildability and pumpability are two of the key material properties needed for successful printing. While not taking the hydration of the cementitious particles

into consideration, buildability and pumpability are closely related to the slump and flow diameter of the material. Figure 3.13 shows that the buildability is proportional to the slump value in the lower region and it is inversely proportional to the buildability in the upper region. While printing Mix 21L, its stiff material behaviour causes pores and discontinuity that eventually cause the sample to lose structural integrity hence its low buildability. On the other hand, in the upper region of the slump and flow diameter graph, the filament at the bottom is too soft to support the weight of the subsequent layer thus causing instability in the structure. Therefore, the middle region between the two extremes regions possesses a balance material behaviour ideal for printing. This middle region should be between a slump value of 4 and 8 mm and a flow diameter value of 150 to 190mm.

Past research has shown that as the yield stress increase, the flow diameter decrease [106]. On the other hand, the flow diameter decreases as the plastic viscosity decrease. Since the viscosity is a measure of the resistance to the flow of a fluid as it decreases, it would mean it is harder for material to flow thus decreasing the flow diameter value. While most literature uses slump test to measure stiffer material, such as zero slump mixture for precast construction, flow table test is used for SCC where the mix usually have collapsed slump [111]. However, in the context of 3D concrete printing, the material behaviour exists in between the two extremes. This cause some of the mixture to exhibit a low slump value while also able to achieve high flow diameter values as compared to other mixture. While the materials may have the same slump, they may behave differently when stress is applied. Material with a low fluidity paste and a low-volume fraction of sand can have the same slump value as a material with high fluidity paste and a high-volume fraction of sand. This is the case

for Mix 3 and Mix 23 where both mixtures have a close slump value and have a significant difference in the flow diameter value. The low fluidity in the paste of Mix 3 dominates the contribution to the material rigidity and the high-volume fraction of sand in Mix 23 dominates this contribution. As shown in Figure 3.15 and Figure 3.16, Mix 3 and 23 have close slump values but the material characteristics such as buildability, surface quality index and pumpability index vary (See Table 3.6). Therefore, the flow diameter value is another parameter to characterise the material behaviour. Although flow diameter seems to be proportional to the slump value, flow diameter helps to differentiate different material behaviour when stress is applied.

Besides the slump and flow diameter values, the pumpability index and the surface quality index are also introduced to better characterize the pumping behaviour and the printed material surface finish respectively. The pumpability index is correlated to the flow diameter values and has a similar trend with the surface quality index. While this surface quality measurement approach serves to quantify the surface quality of the printed structure, the result obtained for analysis is limited to this experiment only. The surface quality index is a relative estimation of surface quality. The result obtained cannot be used to compare with other samples in another study.

The morphology of concrete printed samples is much different from a cast sample. Although the material flow rate and the nozzle travel speed can be the same for all mix design, the surface finishes obtained are not the same. This has to be the material individual morphology. All mixtures in this study are bind together by the cementitious paste. However, as the cementitious paste is lesser for the mixtures with

lower slump or flow diameter values, the material may not be able to bind properly after extrusion thus creating cracks and voids.

In general, the result obtained in this study is limited to the material used and the printer's limitation. This investigation gave an insight into the performance of a printable material over a limited region. Such material performance is based on printer capability and material morphology. While the performance of the mixtures obtains from this study is dependent on the material used and printer performance, similar trend and behaviour should possess in other cementitious material.

3.5 Chapter summary

This investigation used a standardized field-friendly protocol to measure the slump and flow diameter values of the mortars. It is found that compared with fly ash and silica fume replacement ratio, water-to-binder ratio and sand-to-binder ratio play a much bigger role in the slump and flow diameter values when hydration is not considered. The slump and flow diameter results are also correlated for these mixtures.

The pumpability and buildability of 3D printable concrete are evaluated in terms of the pumpability index, surface quality index and the maximum height printed. The 3D printing tests show that the surface quality increases with flow diameter value and pumpability index. The buildability in terms of maximum height is optimal in the middle range. Mixtures with a slump between 4 and 8 mm and a flow diameter value between 150 and 190 mm give a smooth surface and high buildability for a limited range of raw material and printing parameters. Thus, the material printable region is defined according to the slump and flow diameter values.

With this simple and standardized method, printability of the mixtures can be determined before 3D printing.

Chapter 4: Time gap effect on the bond strength of 3D printed concrete

4.1 Introduction

The conventional construction method uses formwork with vibrating rod to remove air bubbles and increase the compaction of material within the formwork. Such a process produces homogenous material where the strength is the same throughout the structure. However, for 3D concrete printing, the vibrating rod cannot be used since there is no temporary support and inducing a vibration would cause shear thinning on the material causing the structure to collapse. Without vibration, This layering effect and the time gap caused the material to possess a weak bonding at the interface between the two layers [57], [68]. As the nozzle travels to trace out the two-dimensional profile to print a layer, the time it needs to reach the same location on the subsequent layer is called “time gap”. The time gap is dependent on the travel speed of the nozzle and the distance that it needs to cover for a single layer.

4.2 Rheological behaviour of cementitious paste

Rheology is the science behind the material deformation and flow, which emphasizes the relationship between the stress, strain and time [112]. The rheology of mortar, containing a range of particle size, is more complicated than one of its constituent material which is cement paste [113]. Banfill [114] mentioned that the flow properties of suspensions are governed by the interface of the solid-water and the dominant contribution is the cement-water interface. The presence of the aggregates increases the material stiffness causing some of the result to exceed the rheometer measurement limit. Therefore, in this study, the rheological testing only focuses on the cementitious paste instead of the mortar.

Fresh cement paste is a concentrated suspension that exhibits a complex viscoelastic behaviour [115]. Understanding the viscoelastic behaviour of cement paste can be helpful to better understand the behaviour of concrete [116]. Viscoelastic behaviour of a material is often modelled by a system of dashpot and springs. The dashpot represents the viscous behaviour of the material and when a load is applied, the deformation will increase with time. The viscous behaviour is usually represented by the loss modulus G". The spring represents the elastic response of the material. This spring elasticity behaviour of the material is defined by the storage modulus G' [117]. The dynamic test can be used to distinguish the elastic and viscous properties of the material [118].

Research done by Roussel and Cussigh [119] has shown that in distinct-layer casting (casting two layers of self-compacting concrete (SCC)) the initial layer has a short amount of time to rest and rebuild structure before the second layer of SCC is cast above it. If the initial SCC layer rebuilds too much, above a critical yield stress value, the two layers do not mix well thus creating a weak interface between the concrete layers. Furthermore, this weak interface may increase porosity locally and could cause permeability to an aggressive substance. The time gap in-between the two layers should be as small as possible to eliminate this weak interface.

This chapter focuses on investigating the effect of the time gap on the material in its fresh states and its correlation with the tensile strength. Rheological experiments were conducted to examine the effect of time on the paste material behaviour in its fresh states under high shear which mimics the pumping process, as well as the effect of time on the structural rebuild of the paste material in its fresh state which mimics the material at rest after extrusion. In addition to the rheology

test, the observation at the macroscopic scale of the cross-sectional inter-bond layer will be examined to understand how layers are stacked on top of another which could provide insights on the bonding affected by the time gap.

4.3 Methodology

4.3.1 Materials preparation

The mix design was aimed to meet the requirement of pumpability during delivery through the hose and shape retention after extrusion. Material preparation details are specified in Section 3.2.1. Table 4.1 shows the mix design composition. No additives were incorporated in this study as the main objective is to investigate the effect of time gap the inter-bonding layer. Addition of additives may increase the complexity of this study.

Table 4.1: Mix design of material to binder ratio by weight

Cement to binder ratio	Fly ash to binder ratio	Silica fume to binder ratio	Sand to binder ratio	Water to binder ratio
0.7	0.2	0.1	1.2	0.46

After printing, to prevent evaporation of the water from the fresh concrete, the samples were covered with a plastic wrap. After 24 hours in the plastic wrap, these printed samples were cut into smaller cube size of 30 mm^3. These smaller cubes were then wrapped back with the plastic wrap and were cured in the laboratory environment for 28 days under the temperature of 23 ± 2 °C and relative humidity of 60%.

4.3.2 Rheological measurement protocol

A rheometer (MCR102, Anton Paar, Germany) equipped with a measuring stirrer with two hollow blades (Stirrer model: ST59-2V-44.3/120) and a cup was used. The cup of the rheometer has a modular insert cage with serrations as shown in Figure 4.1(a) to prevent wall slippages. Figure 4.1(b) illustrates the schematic drawing of the measuring system. Two protocols were conducted: amplitude oscillatory sweep test and rotational-oscillatory time sweep test.

An amplitude sweep was carried out to measure the critical strain of the material. Using a value below the critical strain allows the material to rebuild its structure without destroying its internal bond. The rheometer oscillates at a linear increment shear strain from 0.01% to 1%. The frequency is held constant at 1Hz. A strain value within the linear viscoelastic region (LVR) will be used in the structural rebuild test.

Rotational-oscillatory time sweep test was carried out to determine the viscoelastic behaviour of the paste. In the first interval, the rheometer destroys the microstructure with a constant rotational shear rate $\dot{\gamma}$ of 10 s^{-1} for the duration of 50 seconds. In the second interval, the material is allowed to recover and the stirrer oscillates within its LVR with a shear strain γ of 0.1% at 1Hz for the duration of 300 seconds. This test was carried out at a different time intervals after mixing (0-minute delay, 10-minutes delay and 20-minutes delay) to simulate the time gap printing.

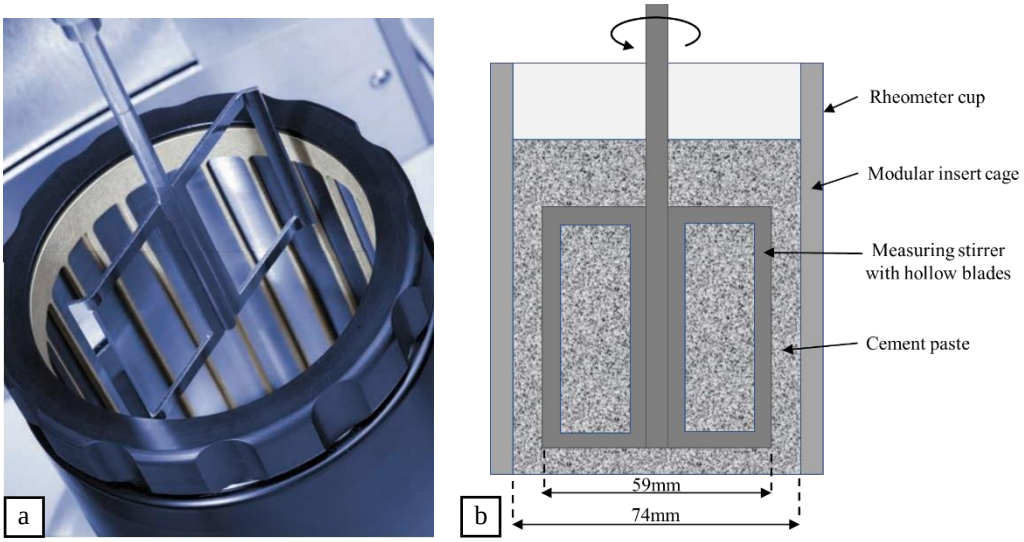

Figure 4.1: (a) Rheometer measuring system [120] (b) schematic drawing of the measuring system

4.3.3 Printing parameters

A gantry printer is coupled with a rectangular nozzle orifice with a dimension of 30 mm by 15 mm. The schematic drawing of the printing parameters such as concrete flow direction, printing directions and nozzle orientation were shown in Figure 4.2. A rectangular nozzle was chosen because it provides a large surface contact area between the layers which contributes to the stability during printing. Interval of 1-minute, 5-minutes, 10-minutes and 20-minutes was chosen as the printing time gap in-between layers. Some other printing parameters are shown in Table 4.2.

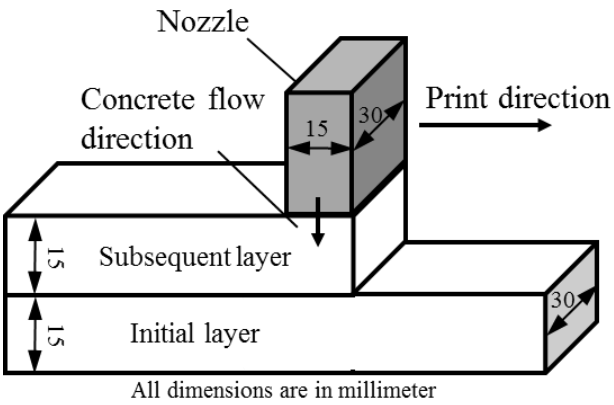

Figure 4.2: Schematic drawing of the flow of concrete

Table 4.2: Printing parameters used for the experiment

Travel speed	Flow rate	Layer height	Area of the nozzle orifice
80 mm/s	39 $m\ell$/s	15 mm	450 mm^2

The initial layer is denoted by 0-minute and the subsequent layer of the printed filament is denoted by 1-minute, 5-minutes, 10-minutes and 20-minutes depending on the time gap in-between the filament as illustrated in Figure 4.3.

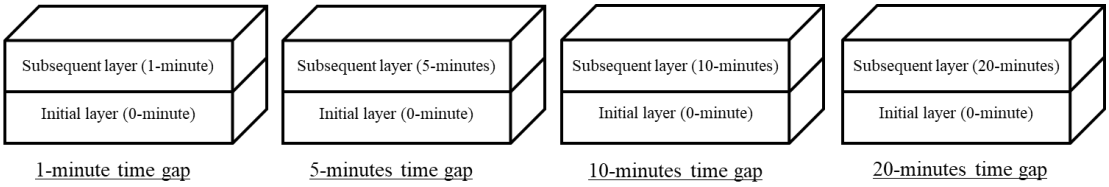

Figure 4.3: Labeling of different layers for this study

4.3.4 Bond test

Instron 5960 dual column tensile test machine was used to measure the tensile bond strength of between the two layers on the 28th day after printing. In this investigation, the direct tensile bonding tests were conducted only on 3D printed samples with interfaces. Four cube specimens at each time gap with a length of

30 mm were extracted from the concrete block with a diamond cutter. It is noted that the height of the sample is relatively small compared to the width, which might induce not only tensile stress but also shear stress during the fracture.

Both sides of the samples were glued to two mild steel plates using rapid hardening adhesive (X60) supplied by HBM showed in Figure 4.4. The tensile test was carried out at a rate of 0.035 ± 0.015 MPa/s according to ASTM C1583/C1583M-13 [121]. It is noted that after extrusion, the filament exhibits slump behaviour. The cross-section of the filament shows an isosceles trapezoid shape where the bottom length is longer than the top length. The effective area of bonding and failure load was then used to calculate the bond strength for each specimen and the average bond strengths out of the four samples were reported and discussed in the following section.

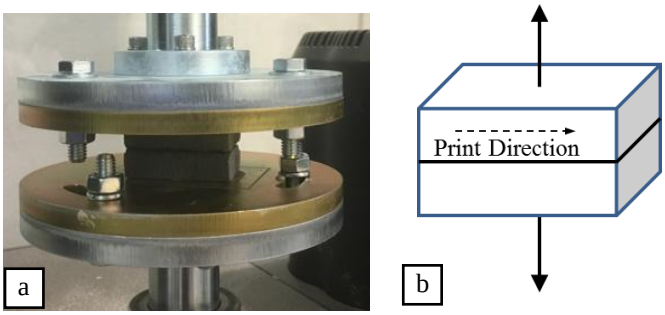

Figure 4.4: Preparation of specimen for the tensile test.
(a) Actual experiment setup (b) Schematic drawing of the bond test

4.4 Results

4.4.1 Rheological measurement result

The amplitude oscillatory sweep test result used to determine the critical strain is shown in Figure 4.5. This critical strain was measured to be above 0.2%.

Below the critical strain, the structural integrity of the network is maintained during measurement [122] and behaves like solid. The material behaviour is dominant by the storage modulus (G') indicating that the material is highly structured [123]. Above this critical strain, the bond between the particles no longer has an attractive interaction and the flocculated network loses its structural integrity [124]. Only the paste portion of the material was used in the rheological experiment (which includes only cement, fly ash, silica fume and water as shown in Table 4.1). Since the change in the material stiffness behaviour due to time effect is mainly caused only by the hydration in the paste portion, to reduce the complexity of the material, the inert aggregates were not included in the rheological testing.

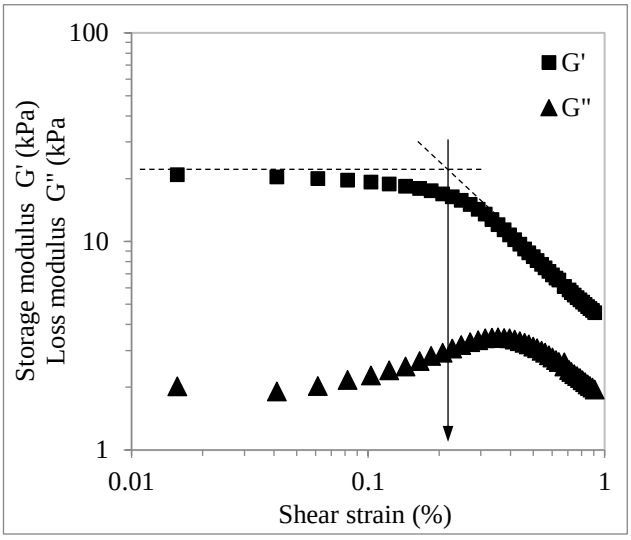

Figure 4.5: Critical strain of paste material with strain sweep measurement

After the LVR is defined by the strain sweep, the effect of time on the material structural rebuild can be further characterized using the rotational-oscillatory time sweep test. The LVR is below the critical strain value of 0.2% as measured by the amplitude sweep test (See Figure 4.5) [125]. To ensure the strain is well within the

LVR, 0.1% strain was chosen to be used for measurement. The rotational-oscillatory time sweep test in the second interval will oscillate within the material LVR which will not destroy the microstructure [126]. 1-minute and 5-minutes samples were not included in the rheological experiment because of the proximity of the time difference and the difference was thought to be insignificant as compared to 10-minutes and 20-minutes samples.

The first interval of the protocol rotates the material at a constant shear rate of 10 s^{-1}. In this interval, the microstructure bond within the material is broken down which simulates the action of the pumping process where the material is delivered from the reservoir to the print-bed [127]. The rheological breakdown measurement is shown in Figure 4.6. The calcium silicate hydrate (C-S-H) is the product of hydration that is responsible for the strength gain in the material. As time increases, more C-S-H is formed between the cement particles, which increases the strength of the material [128]. When a constant shear rate is applied to the material, the bond breaks down in a logarithmic manner for all time gap samples as presented in Figure 4.6. It requires more effort to pump a 20-minutes sample because more C-S-H bond was formed as compared to a 0-minute sample.

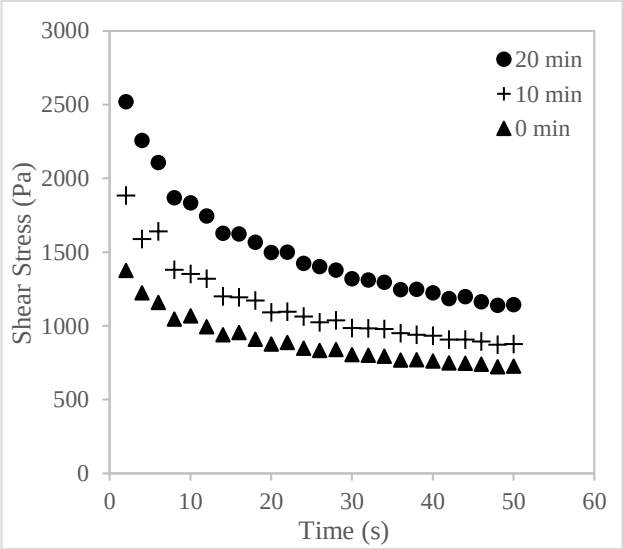

Figure 4.6: Results of the first interval for the structural rebuild test

Figure 4.7 shows the oscillation result for the second interval. This second interval oscillatory result mimics the structural build-up of the subsequent layer material after extrusion in the printing process. Although there is a time difference between the samples (10-minutes and 20-minutes time difference), this time gap does not affect the stiffness and structural build-up rate which implies that the material behaves the same for all time gap specimen (0-minute, 10-minutes and 20-minutes) after extrusion as shown in Figure 4.7.

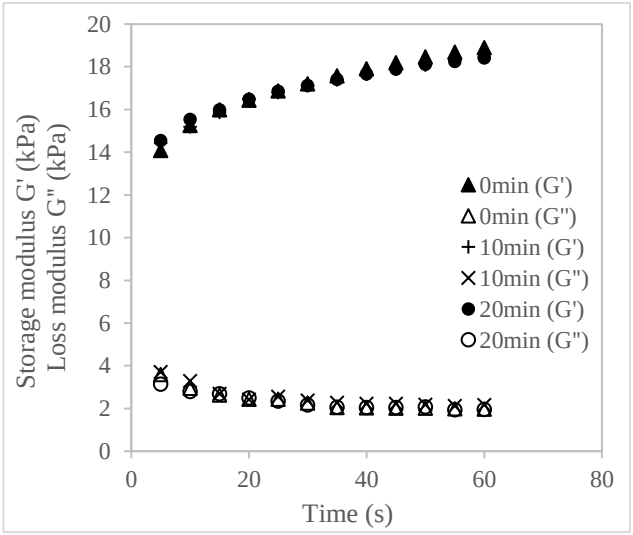

Figure 4.7: Oscillatory results of the specimen at a different time interval

The structural build-up of the initial layer increases logarithmically as presented in Figure 4.8. This increment behaviour of the material structural build-up is inversely proportional to the tensile strength of the material. The forces acting on the initial layer caused by the layering of the subsequent layer above will induce certain shear stress on the interfacial material on the initial layer. This shear stress is the same for all time gap, considering that the subsequent filament size, shape, height and material properties remain unchanged. With the increase in stiffness in the initial layer of the material, it will require higher stress to achieve the same shear strain for the 20-minutes sample as compared to the 0-minute sample.

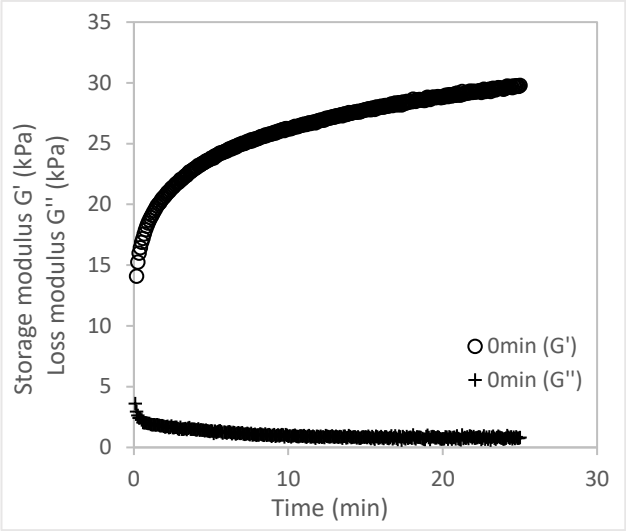

Figure 4.8: The structural build-up of the initial layer

4.4.2 Time gap effect on bond strength

The direct tensile test results as shown in Figure 4.9 show a decrease in strength as the time gap increases. The strength reduced logarithmically, it is more significant initially between 1-minute and 5-minutes time gap and the reduction in strength is insignificant after a 10-minutes time gap (See Figure 4.9). This material behaviour is similar to the material structural build-up rate. As time increases, more C-S-H nucleation occurs between the cement grain which improves the overall stiffness of the material [129]. The stresses acting on the initial layer by the subsequent layer during deposition is the same for all time gap. This increase in stiffness at the initial layer will cause less disruption on the interfacial materials as time gap increases, thus producing a weaker bond due to insufficient interaction between the two layers.

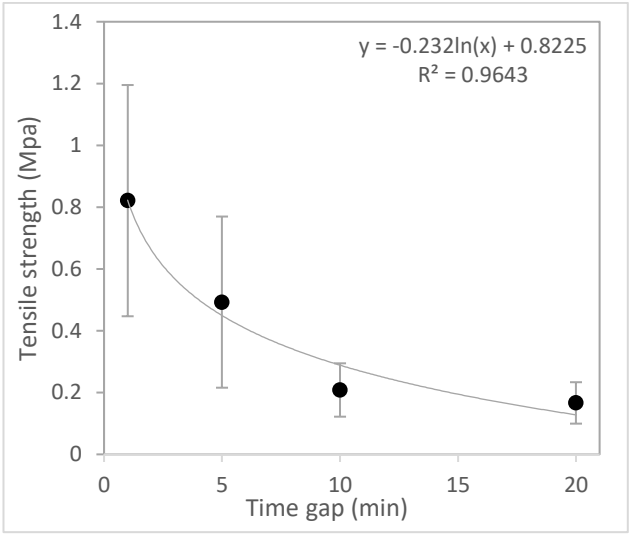

Figure 4.9: Tensile strength of samples at the different time gap

In order to interpret the result statistically, a one-way ANOVA is used to compare the result. The P-value for the time gap interval ANOVA is less than 0.05 as shown inTable 4.3. This indicates that the bond strength at different time interval differs significantly. A Tukey comparison is used to test the difference between the pair of groups if it is statistically significant. The graph that includes the Tukey simultaneous confidence intervals shows that the confidence interval for the difference between the means of time interval at 1min and time interval at 10mins is 0.167 and 1.06 as shown in Figure 4.10. A similar confidence interval is noticed for time interval at 1min and time interval at 20mins. This range does not include zero, which indicates that the difference between these means is significant. The confidence intervals for the remaining pairs of means all include zero, which indicates that the differences are less significant.

Table 4.3: One-way ANOVA for time gap interval

Source of variation	Degree of freedom	Sum of Square	Mean Square	F-Value	P-Value
Factor	3	1.1008	0.36694	8.13	0.003
Error	12	0.5414	0.04512		
Total	15	1.6422			

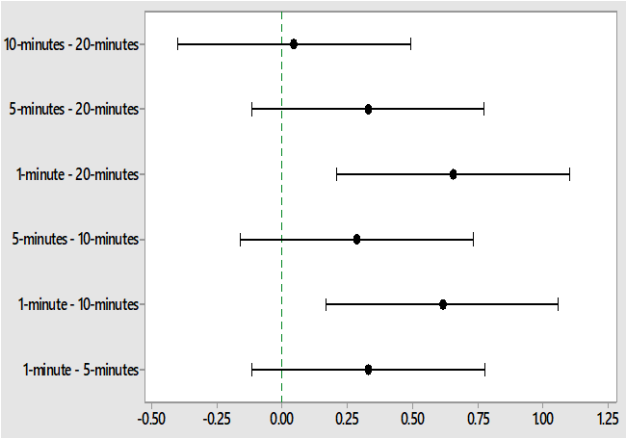

Figure 4.10: Tukey simultaneous 95% confidence intervals

Further investigation on the bond from its cross-section shows that there are almost no obvious voids in-between the layers for the 1-minute specimen (See Figure 4.11(a)). However, as the time gap increases, the void in-between the layers is increasingly obvious (See Figure 4.11(b), (c) and (d)). The interfacial materials at the initial layer and the subsequent layer are sensitive to disturbance when the time gap is short. As a new layer is deposited on top, the interface layer at the bottom substrate may rearrange its orientation to accommodate the stresses brought by the deposition of new layers. However, the material stiffness at the initial layer increases logarithmically with time. As a subsequent layer is deposited on top, the energy caused by the deposition is not sufficient for the interface layer to rearrange its orientation thus voids appear at the bond as shown in Figure 4.11.

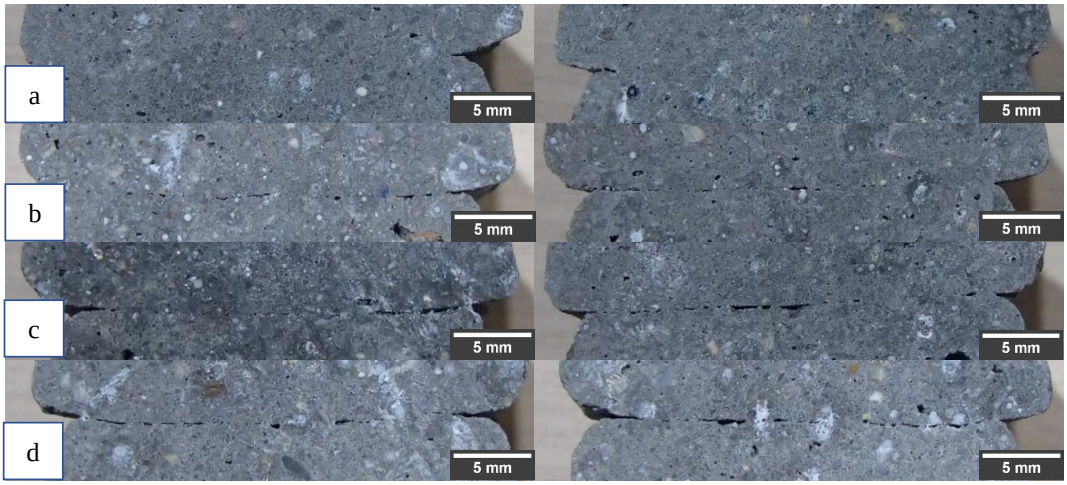

Figure 4.11: Samples printed at (a) 1-minute time gap (b) 5 minutes time gap (c) 10 minutes time gap (d) 20 minutes time gap

Close observation shows that at longer time gaps, the filament at the interface is deformed forming a mild U-shape (See Figure 4.11(b), (c) and (d)). This deformity may be caused by the weight of the subsequent layer and the stresses during the printing process which may disturb the interface material. When the material has a short time gap, this disturbance will help the material at the interface to interact and bond well. However, if the time gap is long, the material at the interface does not interact well thus only deforming it without interaction, creating voids at the bond interface.

4.5 Discussion

It could be seen in Figure 4.6 that during the pre-shear process, which corresponds to the pumping process during 3D printing, the longer the resting time, the higher the initial shear stress in the beginning is. It could be related to the structural building up process due to colloidal flocculation [99].

However, after a strong shear over 50-seconds, the equilibrium shear stress becomes much closer between various resting times. Moreover, after extrusion, as shown in Figure 4.7, the storage moduli between various resting times show little difference. It could be assumed that the pumping process is strong enough to break down the microstructure and eliminate the effect of resting time on the shear stress or modulus within 20-minutes.

After extrusion of the initial layer, the modulus of the initial layer will increase with time shown in Figure 4.8. Longer time gap will result in higher modulus of the initial layer. The increase in modulus of the initial layer could make the interface too stiff to mix well with the subsequent layer. For the actual printing process, since the second layer shows similar performance, the difference in tensile bonding under various time gap could be related to the modulus of the first layer. Some researcher attributed it to the surface moisture of the first layer [130].

In the meantime, in this investigation, it was found that the pores at the interface could play another big role. Similar research also found a large gap between the filament in the scanning electron microscope (SEM) images [131]. It is clearly seen in Figure 4.11 that with increasing resting time, the amount of voids at the interface is increasing and the pores become bigger.

Although the printed material shows an anisotropic property, this manufacturing technique is not the direct cause of it. If the material has high workability and is able to interlock with the previous layer caused by the printing process, the bond strength would remain the same, regardless of the time gap. However, since the stiffness of the material increases with time and in order to retain

the shape retention capability, there is a limit in the workability of the material which makes the time gap important.

4.6 Chapter summary

3D concrete extrusion-based printing has a printing time gap in-between layers, due to the layer-wise manufacturing method, which has a considerable influence on the bond strength between the filaments. Rheological properties of the initial layer will have an impact on the bond with the subsequent layer and the adhesion at the interface between these two layers is the key to the tensile strength of the structure. The modulus of the subsequent layer is not affected by the time gap, however, the modulus of the initial layer increases with the time gap. It is reasoned that high modulus of the initial layer prevented the good contact and mix at the interface. As the time gap increases, voids were increasingly induced at the interface which weakens the bond strength logarithmically. In the meanwhile, the high modulus of the initial layer is necessary to support the subsequent layers and keep structural stability.

Chapter 5: Effects of printing parameters on printing region and support structure

5.1 Introduction

Although printing complex structure was demonstrated by Le et al. [8], a major hurdle persisted for 3D concrete printing is to construct overhanging structures. Unlike the other popular B&C powder-bed fusion techniques which use un-used powder to create the support required for overhanging structures as reported by Feng et al. [132], a temporary physical surface to support the overhanging filament is required for extrusion-based printing which would otherwise be hanging over empty space.

For extrusion-based 3D concrete printing, some popular techniques that were used to accommodate for overhanging structures include support-less closed structure design and using supporting wood planks, as shown in Figure 5.1. Rudenko [133] printed a parabola-shaped window as shown in Figure 5.1 (a). This support-less closed structure design has a maximum slope angle with reference to the printing direction that can be printed without the structure collapsing. The maximum slope angle of the design is material-dependent. Even though using self-supporting design to support overhanging layer is a clever idea, it is limited by the slope angle. More recently, a house printed on-site by Arup [134] with a portable robot to showcase the role of 3D printing can play in reducing construction waste, by minimizing inefficiencies during the building process. Wooden planks and scaffoldings were used to support the overhanging material as shown in Figure 5.1(b). Although the existing support technique as shown in Figure 5.1 is able to mitigate the overhang problem, human intervention and design constraint are still issues that need to be solved.

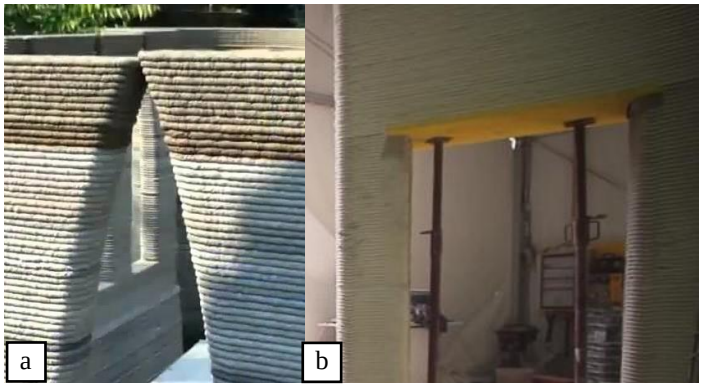

Figure 5.1: Different techniques used for printing overhangs. (a) support-less closed structure design to support subsequent overhanging layer [133] (b) wood planks with supporting scaffolding [134]

To overcome the freeform issue, a method varying the printing parameters to produce support material is proposed. This technique can effectively build structures with overhanging components. In this investigation, the gaps between the supports were exploited to determine the maximum distance of the bottom layer without the subsequent bridging layer sagging. By varying the flow rate and travel speed, it is possible to obtain the optimum range for the main structure and the support structure.

This chapter aims to print a support structure by examining the effects of printing parameters on the printed filament. This examination on the printing parameters hopes to obtain different material properties for different printing operations. In Section 5.2, presents the methodology of the technique proposed in this investigation and the results in Section 5.3 will be examined. Lastly, the discussion and conclusion in Section 5.4 and 5.5 will review the advantages, limitation of this proposed technique.

5.2 Methodology

5.2.1 Materials and preparation

Table 5.1 shows the material composition. The material preparation of the mix design is illustrated in Section 3.2.1. While the material's hydration plays an important role in the strength gain, due to the small structure printed and the long setting time of the material, the stiffening rate is neglected in this investigation. The mixed material was placed in the progressive cavity pump for printing immediately after mixing.

Table 5.1: Mix design of material to binder ratio by weight

Cement to binder ratio	Fly ash to binder ratio	Silica fume to binder ratio	Sand to binder ratio	Water to binder ratio
0.7	0.2	0.1	1.7	0.495

Panarese [135] suggested that the gradation of the aggregates used for pumping should match the gradation requirements specified in the ASTM C33 [136]. Fine aggregates are important in the design of a pumpable concrete mix. Fine particles such as fine sand and mortar form the lubricating film inside the pipeline and prevent bleeding of the fresh concrete during delivery. On the other hand, excessive fine sand should be avoided, as it not only increases the water requirements, it affects other properties of the material in terms of durability and shrinkage. Crepas [49] explained that finer materials have more surface area to be coated with the cement-water paste. If there is too much fine sand in the mixture, more water will be needed to get the same workability.

5.2.2 Filament and gap distance characterization

A gantry printer coupled with a rectangular nozzle as shown in Figure 5.2 was used in this study. The rectangular nozzle has a dimension of 30 mm by 15 mm which forms a nozzle orifice area of 450 mm^2 and the height of each layer was set at 15 mm to match the width of the nozzle.

Figure 5.2: 30 mm by 15 mm nozzle used for printing

Two printing paths (See Figure 5.3 and Figure 5.4) were established to characterize the filament. The first printing path was used for filament characterization. As shown in Figure 5.3, the printing path was repeated for four different flow rates (37.9 ml/s, 45.2 ml/s, 48.0 ml/s and 51.3 ml/s) to print a single layer. An analogue knob is used to control the speed of the pump during printing. A range of values on the analogue knob was selected between the maximum and minimum operating range of the pump. These analogue values correspond to the material flow rate selected.

Evaluation of the relationship between the printing parameters and the dimensional parameters of the filament was carried out by characterising with a dimensionless value $R_{m/i}$. It is the ratio of the measured top surface area divided by the ideal surface area of the filament.

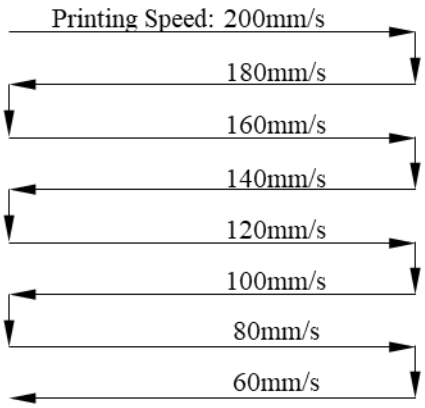

Figure 5.3: Print path for filament characterization

A support structure should be printed with sufficient top surface area to support the subsequent main layer. Therefore, to simulate the different breakage gap distance in the support filament, the printing path as shown in Figure 5.4 is established. The objective for this test is to evaluate the maximum gap distance on the support filament (first layer) before any significant sag in the bridging layer (second layer) that is in contact with the support filament is observed. A bridging layer is defined as the subsequent layer in contact with the support layer. This bridging layer is printed over the gaps of the support layer and it should not have significant sag or breakages. The flow rate and travel speed are kept constant for this investigation.

5.2.3 Solidity ratio and printing limits

The flow rate of the material and travel speed of the nozzle variation can affect the solidity ratio (*SR*) which is the expected filament size and is defined as:

$$SR = 1000Q/A_p v \quad \text{Equation 5.1}$$

where A_P (mm^2) is the cross-section area of the nozzle, v (mm/s) is the nozzle travel velocity and Q (ml/s) is the flow rate of the material.

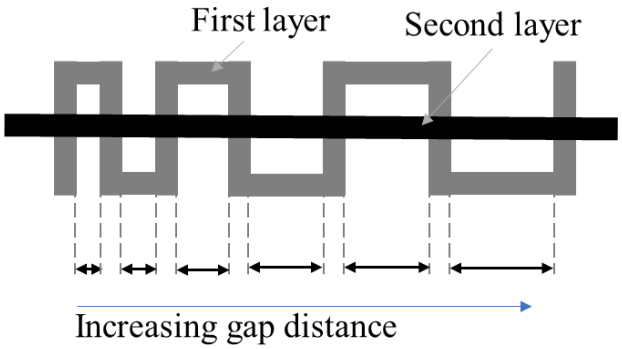

Figure 5.4: Print path for gap distance characterization

Figure 5.5 shows the theoretical effect of the flow rate and the travel speed on the filament. In theory, when SR is less than 1, the printing process is operating within region D, where there are more discontinuities, more voids, lower filament strength and smaller filament width. On the other hand, when SR is more than 1, the printing process is operating in region A, where there are fewer discontinuities, fewer voids, higher strength and larger filament width. Theoretically, the solidity ratio can also be calculated by

$$SR = W_f H_f L_f / A_p v \quad \text{Equation 5.2}$$

where W_f, H_f, L_f (mm) are the measured width, height, and length of the printed filament, respectively. Lao et al. [137] revealed that the filament will deform during

the printing process, the cracks and the fluctuation of flow rate will also lead to measurement error of filament width and length. Thus, further investigation is still necessary to study the relationship between solidity ratio and printing parameters.

Printing processes operating in region B and C, where SR is approximately 1, would produce the best filament. Printing in region B reduces the printing time and the time gap in between the layers. On the contrary, printing in region C increases the printing time.

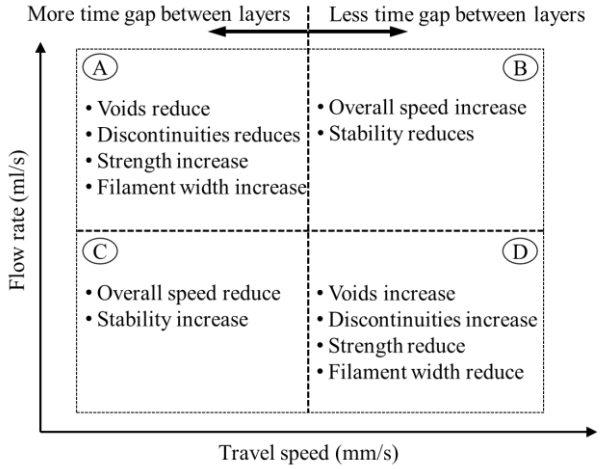

Figure 5.5: Printing limits: effects of flow rate and travel speed on the printed filament

5.3 Results

5.3.1 Effects of flow rate and travel speed on the surface area of the filament

A total of 32 specimens of different flow rates and travel speeds were printed as shown in Figure 5.6. Large filament surface area was found in high flow rates and slow travel speeds (Region A). More material was extruded than expected thus causing the material to be squeezed on to the substrate pushing the material in the lateral direction. Although excess material deposited will improve the bonding

between layers and thus leads to better mechanical strength, but it will also result in the poor surface finish and poor geometrical resolution. On the other hand, large breaks were found in low flow rates and fast travel speeds (Region D). These breaks were caused by the disproportionate slow flow rate of the material exiting the nozzle. The friction force between the substrate and the material that has been extruded causes a shear on the existing material at the nozzle thus resulting in breakages.

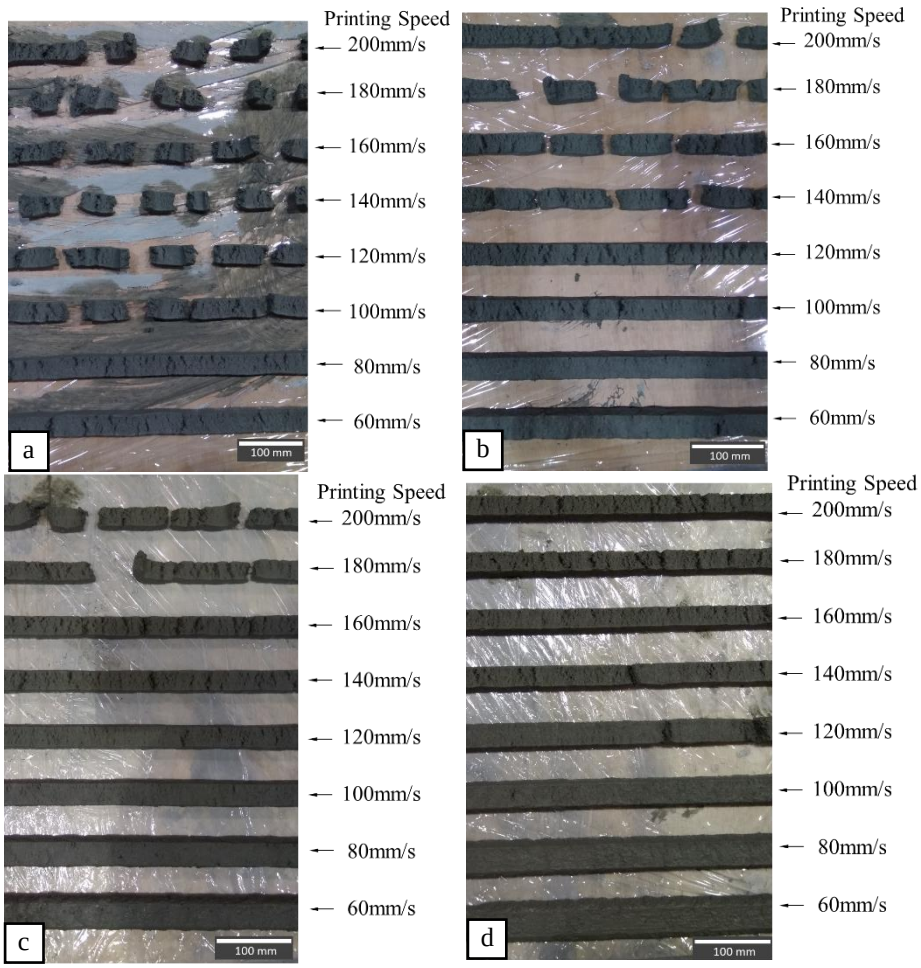

Figure 5.6: Filament printed with different flow rate (a) flow rate: 37.9 ml/s (b) flow rate: 45.2 ml/s (c) flow rate: 48.0 ml/s (d) flow rate: 51.3 ml/s

A filament length of 400 mm was cropped from Figure 5.6 for each respective flow rate and travel speed and was processed with an image processing program

(ImageJ) to measure the printed specimen surface area. This printed specimen surface area is divided by the ideal surface area of the filament which is the filament length of 400 mm and the length of the nozzle of 30 mm to obtain a dimensionless value ($R_{m/i}$)

$$R_{m/i} = A_s / 400 \times 30 \qquad \text{Equation 5.3}$$

where A_s (mm^2) is the printed specimen surface area. Basically, $R_{m/i}$ is the experimental measurement of SR.

The filaments shown in Figure 5.6 were classified into four different types as shown in Table 5.2. The filaments that were found to have a large surface area are shaded in the darkest shade of grey and are found to have an $R_{m/i}$ value above 1.4. Those filaments that have no breaks and cracks generally have the optimum filament width which is within the range of 1 to 1.4. Those filaments that have cracks but do not have any breaks are found in the range of 0.75 to 1. Lastly, those filaments that have breaks and cracks were below 0.75.

Table 5.2: Ratio of the measured surface area and ideal surface area of the filament ($R_{m/i}$).

		Travel Speed (mm/s)							
		60	80	100	120	140	160	180	200
Flow Rate (ml/s)	51.3	1.794	1.470	1.237	1.046	0.913	0.840	0.814	0.785
	48.0	1.523	1.380	1.093	0.999	0.860	0.772	0.681	0.621
	45.2	1.317	1.204	1.062	0.931	0.814	0.712	0.668	0.632
	37.9	0.990	0.860	0.661	0.574	0.480	0.470	0.424	0.398
Filaments that have a thicker width									
Filaments that have no breaks and crack									
Filaments that do not have breaks but have obvious cracks									
Filaments that have breaks and cracks									

5.3.2 Factorial test result

In this study, a factorial test was performed to determine if the printing parameters have any statistical significance on the dimensional parameter of the filament. The velocity is inverse to support Equation 5.1 derived from the first principle and is denoted by s that $s = 1/v$. The formulas to obtain the values in Table 5.3 can be found in the book written by Montgomery [138]. Larger F values indicate that the variation of the printing parameters is more significant on the dimensional parameter changes. From Table 5.3, the F-values of s and flow rate (Q) are 54.92 and 74.59 respectively, which is significant. It is also evident from the F-value that the flow rate (Q) is more significant than the inverse of travel speed (s). However, the interaction of the s and Q ($s \times Q$) does not have a significant effect on the dimensional parameter. On the other hand, low P-value reflects the there is strong evidence that an effect is significant. The P-value of s and Q is lesser than 0.001, this means that these two parameters have a significant effect on the filament surface area.

Table 5.3: Analysis of variance (ANOVA) table

Source of variation	Degree of freedom	Sum of square	Mean square	F-value	P-value
s	7	4.682	0.669	54.92	<0.001
Q	3	2.726	0.909	74.59	<0.001
$s \times Q$	21	0.460	0.022	1.8	0.065
Error	32	0.390	0.012		
Total	63	8.259			

The individual main effect of the travel speed and the flow rate is shown in Figure 5.7. As the inverse of the travel speed increases, $R_{m/i}$ increases. This indicates that the filament surface area increases as the travel speed reduces. The effect is more

significant when the *s* value is around 0.01 to 0.0167 which translates to the travel speed of 60 mm/s to 100 mm/s. It is less significant when the *s* value is around 0.005 to 0.0063 which translates to the travel speed of 160 mm/s to 200 mm/s. On the other hand, the effect of the flow rate is increasing for all values.

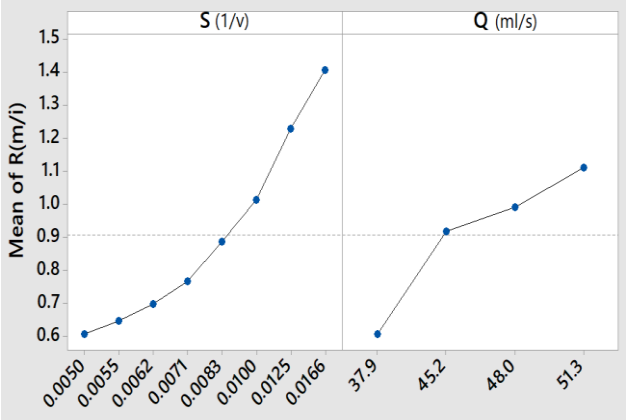

Figure 5.7: Main effect plot for $R_{m/i}$

A quadratic model expression was obtained through statistical software (Minitab). The quadratic model has an R-squared of 0.97 which is a good fit for the actual data. It can be seen in both Equation 5.4 and Figure 5.8 that the measurement value has the same trend as the theory expression and the difference is non-negligible. When the flow rate and travel speed match, i.e., in regions B and C of Figure 5.5, the difference between theory and experimental results is small. However, when the flow rate and travel speed are different, i.e. in regions A and D of Figure 5.5, the difference between theory and experimental results becomes larger. These differences, as discussed in Section 5.2.3, are mainly caused by the deformation of the filament when the solidity ratio is high, or the crack and voids when the solidity ratio is low.

$$R_{m/i} = -0.321 - 54.7/v + 0.0129Q + 2.773Q/v \qquad \text{Equation 5.4}$$

where $R_{m/i}$ is the ratio of the measured surface area to the ideal surface area of the filament, v (mm/s) is the travel speed and Q (ml/s) is the flow rate. Figure 5.9 is evolved from the theoretical chart shown in Figure 5.5 by using data in Table 5.2, which is differentiated by four different types of filament. As indicated in Figure 5.9, the filament surface area increased the most when the increase in flow rate and a decrease in travel speed are in the direction that is perpendicular to the lines separating the types of the filament (Direction A). Moving in direction A also increased the print time. On the other hand, the total print time can be reduced when the flow rate increases and the travel speed increases parallel to the lines separating the types of the filament (Direction B), while keeping the filament width consistent.

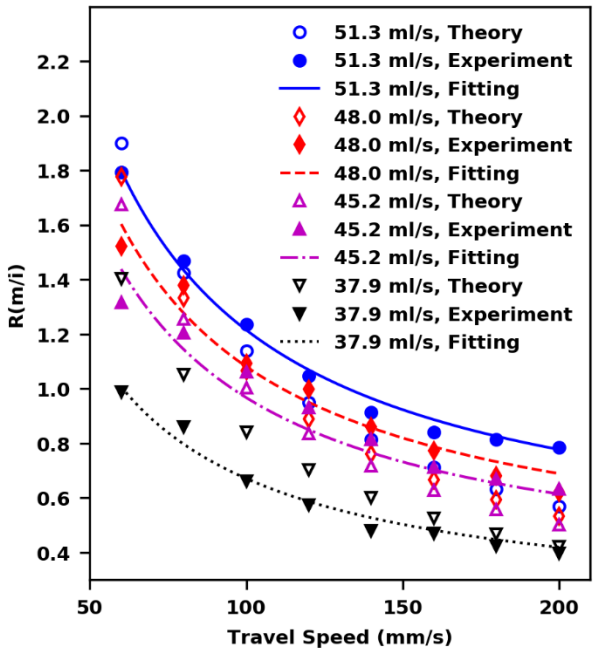

Figure 5.8: Solidity ratio from theory, experiment, and the fitted model.

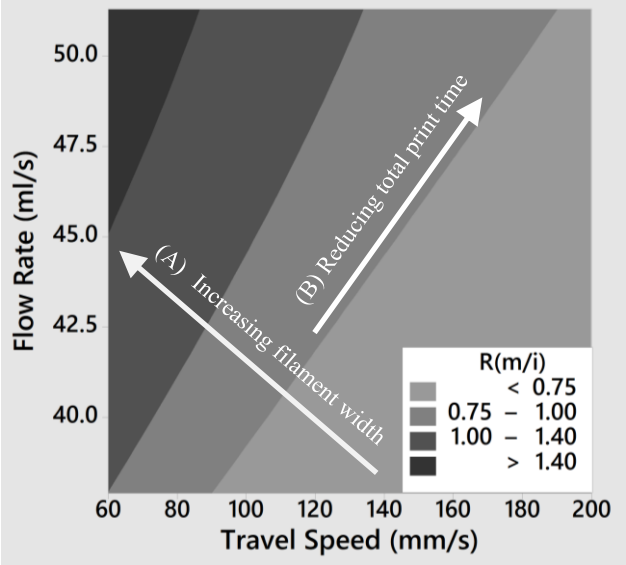

Figure 5.9: Contour plot of the ratio of measured surface area to the ideal surface area of the filament

5.3.3 Bridging vs supports

In FFF, Jin et al. [139] optimized the number of support points which can reduce the total time needed for fabrication. However, the structural recovery of fresh concrete is not as rapid as a polymer material after extrusion, and it tends to sag if there is insufficient support surface underneath. Therefore, it is not recommended to print support structures with large breaks. The following experiment was carried out with the 2nd print path (See Figure 5.4) to determine the maximum gap distance for the bottom support without significant sagging of the bridging layer. The different types of sagging of the bridging layer at different gap distance are shown in Figure 5.10.

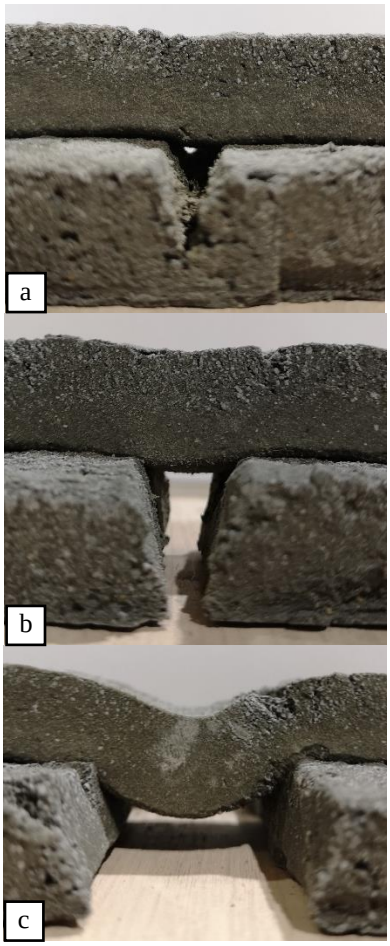

Figure 5.10: Effect of gap distance on the sag of the bridging layer (a) 6 mm (b) 10 mm (c) 28 mm

Figure 5.11 shows the relationship of the gap distance of the first layer to the sag of the bridging layer. An exponential model $y = 1.56[\exp(0.05x) - 1]$ was able to fit the experimental data with $R^2 = 0.9506$. The sag of the bridging layer should not be more than 15 mm which is the thickness of the first layer. In order to maintain a level bottom surface of the bridging layer, a 2 mm sag is determined to be within a satisfactory limit (<13% of the layer thickness). This 2 mm sag of the bridging layer is translated to a maximum 10 mm gap distance of the first layer.

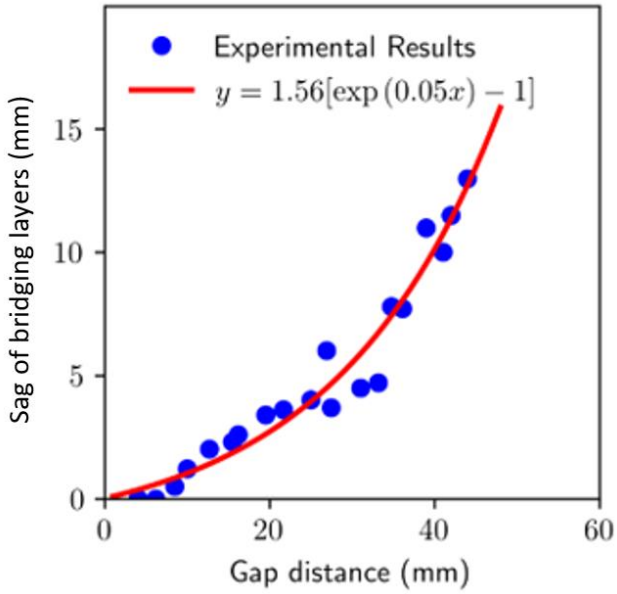

Figure 5.11: Relation between gap distance and the sag of the bridging layer

From Figure 5.6, it is observed that the filament having a gap distance of less than 10 mm is the filament with the travel speed and flow rate of 140 mm/s at 45.2 ml/s and 160 mm/s at 45.2 ml/s, which has a $R_{m/i}$ of 0.814 and 0.712 respectively. Therefore, when the $R_{m/i}$ is less than 0.7, which is referred to as the failure region, the gap distance is larger than 10 mm. To print the support layer that will cause a deformation of less than 2 mm sag in the subsequent bridging layer, the $R_{m/i}$ should be within the range of 0.7 and 0.8. Figure 5.12 is the combined results of Figure 5.9 and Figure 5.11 to show the different regions of the printing parameters.

A normal printing region was determined to have a $R_{m/i}$ range of 1 to 1.4. In this region, the filament appears to have high dimensional accuracy and minimum cracks appearing on the surface, as shown in Figure 5.6. The intermediate region is the region between the normal printing region and support printing region with a $R_{m/i}$ range of 0.8 to 1. This is not suitable for printing the main structure because of the cracks that appear on the surface of the filament which may reduce the strength in

the main structure. It is also not desired for printing supports because the gap distance is too narrow in this region. Printing supports in the intermediate region will use more material than required and it will increase the production time which is uneconomical in terms of time and cost.

The last region is the oversupply region. In this region, the flow rate of the material is significantly higher, which causes the filament to possess a thick and inaccurate dimension. The oversupply region has a $R_{m/i}$ range of more than 1.4. By using Figure 5.12, it is possible to determine the different regions suitable for printing different application.

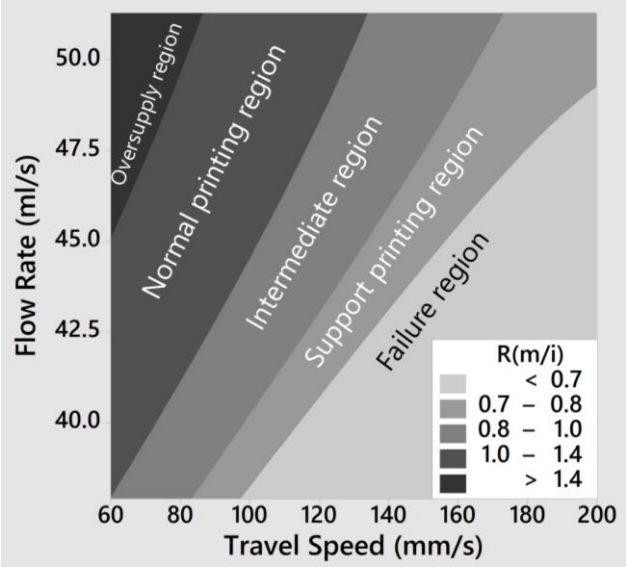

Figure 5.12: Characterization of the different printing region

5.3.4 Printing of supports for overhanging structures

A design as shown in Figure 5.13(c) that requires supports was printed to verify the results obtained from sections 4.1, 4.2 and 4.3. Figure 5.13(a) and (b) show the main structure and the supports printed using the primary materials only. Due to the configuration of the printer, it is easier to keep the flow rate constant throughout

the printing process. Therefore, only the travel speed parameter is changing throughout the printing process. The printing parameters were selected based on the result shown in Figure 5.6 and Figure 5.12. For this demonstration, the flow rate was chosen as 45.2 ml/s. The travel speeds were then selected within the respective region for the main structure and support structure as shown in Figure 5.12. The travel speed parameter to print the main structure and the support structure for this flow rate are selected at 80 mm/s ($R_{m/i}$ = 1.2) and 160 mm/s ($R_{m/i}$ = 0.7) respectively. During post-processing, the support structure was easily removed using a chisel and a hammer after a day of curing and the end result is presented in Figure 5.13(c).

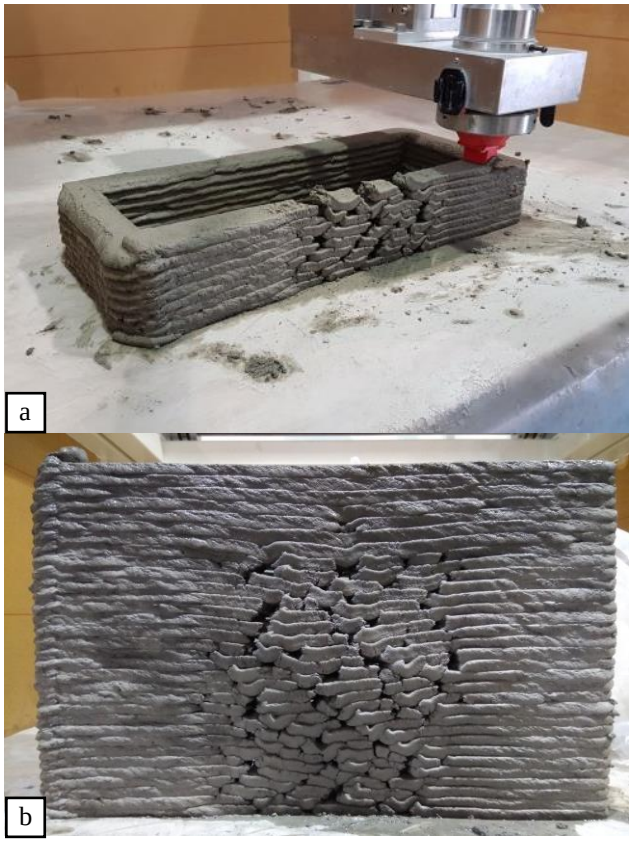

Figure 5.13: (a) Printing with supports (b) before post-processing
(c) after post-processing

5.4 Discussion

The main objective of this study is to obtain a limits diagram to examine the effect of the printing parameters such as flow rate and travel speed have on the printed filament. With the use of this limits diagram, different printing operations can be performed. The printing parameter determinants are the travel distance and time required for each layer. These two requirements can be established by knowing the size of the structure to be printed and the properties of the material used. These two requirements can then be used to compute the travel speed of the nozzle. With the used of Figure 5.12, the other printing parameter (flow rate) can be determined. There are many different printing operations that can be performed, and this limits diagram provides a proper method to identify the suitable printing parameters based on the requirements.

Through the factorial test, it was ascertained that the travel speed and flow rate have a huge effect on the filament dimension and these two parameters are not

dependent on each other. Furthermore, it was observed that the flow rate has a greater effect on the filament dimension. To better understand the sag of the subsequent bridging layer, the gap distance characterisation test was carried out to find the maximum distance that the filament can cross over without a significant sag. In this study, a sag of more than 2 mm on the bridging layer was deemed as a significant sag, therefore the maximum gap distance was determined to be 10 mm. To keep the support layer gap distance less than 10 mm, the $R_{m/i}$ should be within 0.7 and 0.8.

The theoretical concept of the printing parameters regions are shown in Figure 5.5. It indicates a fundamental guide to the effects of the filament dimension at different printing parameter regions. However, after much research was performed and compiling the results in sections 5.4.1 to 5.4.2, the printing parameters regions were remodelled and is presented in Figure 5.9. They were corrected in Figure 5.12 to the printing operations such as normal printing and supports printing. Although the graphs shown in Figure 5.11 and Figure 5.12 are material-dependent, similar material composition can take these graph as a reference. Nevertheless, the methodology approach to characterise the printed filament is the first in this research field and more work can be done to reinforce this methodology. Besides the normal printing and the support printing regions used in this study, the oversupply region and the intermediate region can also be used for different printing operations. When higher strength is required, the oversupply region can be printed within dimensional limits to improve the strength as compared to the normal printing region. On the other hand, if the strength requirement is not significant, printing in the intermediate region can help to reduce the time and material needed. However, these two printing regions can affect the geometrical precision.

5.5 Chapter summary

For 3D concrete printing, material extruded from the nozzle will retain its soft characteristic. Without the use of formwork, a temporary physical surface is necessary to support the overhanging filament. Based on the literature review in section 2.4.2, printing supports with the primary material can eliminate the complexity of a dual-nozzle system, as well as, eliminating the increase in the time gap between the bridging layer and the current layer where the support is added. In this study, the feasibility of adjusting the printing parameters to print the main structure and support structure using a single type of building material was demonstrated.

It was found that the nozzle travel speed and material volume flow rate significantly affect the solidity ratio of the filament. Additionally, a gap distance characterisation test was carried out to find the maximum gap distance that the filament can cross over without a significant sag. The combined results were used to determine the different printable regions for different operations. An overhang structure was printed to verify the results obtained. The main advantage of this technique is being able to complete the printing process with minimal human intervention and without much interference to the printing time gap. It also allows the complex structure with overhangs to be built.

The use of primary material to print support structure was found to bring more benefits than the other two support techniques. However, this investigation does not suggest that using the primary material as a support structure is the best method. Support structures are eventually sacrificed after the object is built. Furthermore, the presence of support structures increases both the manufacturing time and post-

processing operations. Since printing support with primary material has its own setbacks, the first rule of thumb is to decrease the use of support material to reduce waste.

With these printing regions established, printing a functionally graded material (FGM) is possible. The investigation in Chapter 6 such as printing with different travel speeds and flow rates can create an optimised structure that possesses different material characteristics.

The proposed method as demonstrated can be used for small construction activities such as window openings, electrical, mechanical, and finishing work or holes. It is unwise to print a support structure that is twice or more than the amount of material required to print the main structure. Different support techniques can be combined to fabricate the main structure with the aim of reducing manpower, material waste and time required for production.

Chapter 6: Printing functional graded concrete materials

6.1 Introduction

Functionally graded materials (FGM) are a type of inhomogeneous material that comprises of different material properties engineered to perform multi-functional role [140]. This type of material has a large impact in terms of cost, material and energy-saving [140]. However, due to the limitation in the conventional method of casting concrete, functionally graded concrete material (FGCM) is not common in the building and construction (B&C) industry. It is even more uncommon for porosity gradient functionally gradient concrete material, where the porosity within a specific region of the concrete changes according to its requirement. Such material is more popular in the biomedical industry. Usually, the material that is intended to be replaced has functionally graded porosity in nature and the graded porosity would help in the integrations of the implant and the surrounding tissue [141].

In recent years, the interest to use three dimensional (3D) printing for B&C industry has increased [3], [142]. This manufacturing method is able to create complex structure without the need for formwork. Furthermore, this layer-wise manufacturing technique has the potential to reduce material wastage, reliant on labour and manufacturing time [3], [143]. Most of the research work in 3D concrete printing focuses on new printable materials and possible design to improve the mechanical strength [68], [101], [144]. There is little research on the topological optimization of the printed structure especially in the direction perpendicular to the print path. Since this manufacturing technique produces structure in an additive manner, if the amount of material deposition can be controlled through topology

optimization, a structure with different mechanical property can be created. Additionally, printing an FGCM structure helps to improve the strength-to-weight ratio, save on the load-bearing requirements of the structure as well as improve the use of resources effectively. Asprone et al. [145] have demonstrated the concept of printing a concrete beam with reinforcement. He applied a flexural loading as shown in Figure 6.1 and found out that the initial flexural stiffness of the printed reinforced concrete (RC) beam has a comparable result with a full solid RC beam. Similar work was carried out by Salet et al. [146] by printing a full-scale bridge. Such an approach increases the complexity of a structure but will not affect the printing cost. Although the work presented was not topologically optimized, it proves that printing concrete struts in the beam can improve the performance.

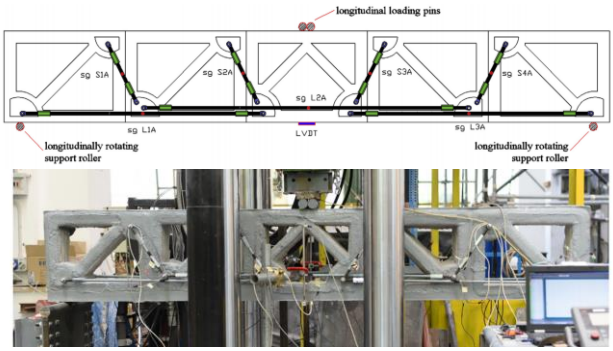

Figure 6.1: 3D printed reinforced concrete beam.

6.2 Methodology

6.2.1 Materials preparation and experiment setup

Ordinary Portland cement (OPC, ASTM Type 1, Grade 42.5), silica fume (Undensified, Elkem), fly ash (Class F) and river sand were used in this study. The information on the material mix design used in this study cannot be disclosed due to the non-disclosure agreement with the collaborators. However, the information on

the material properties such as the compressive, flexural and tensile strength can be disclosed and are 30 MPa, 4 MPa and 0.8 MPa respectively.

The material preparation procedure is illustrated in Section 3.2.1. A gantry printer was used in this study and with the help of a positive displacement pump the concrete is extruded out of the nozzle. The shapes and sizes of the nozzles determine the dimension and geometry of the concrete filament. Hence, it is important to select the right nozzle for the print. Additionally, the print path of the structure in this investigation has many sharp corners to navigate. Therefore, a round nozzle with a 12 mm diameter is selected for this investigation to print the optimized structure in two dimensions and three dimensions. All samples were cured in the lab conditions in an ambient temperature of 22.5°c and 61% humidity for 28 days before testing. These samples were also fully covered with a plastic sheet during the curing process. All experimental results were shown in Section 6.4.

6.2.2 Parameters characterization test

There are two different parameter characterization tests established in this study. The first characterization test is the filament characterisation test, where seven different flow rates (6 ml/s, 9 ml/s, 12 ml/s, 16 ml/s, 19 ml/s, 22 ml/s and 24 ml/s) and seven different travel speed (60 mm/s, 75 mm/s, 90 mm/s, 105 mm/s, 120 mm/s, 135 mm/s and 150 mm/s) are used in this characterization. The protocol is illustrated in Section 5.2.2. This test maps out the printable range of the printing parameters as some of the printing parameters can cause poor structural integrity due to insufficient material or dimensional error due to an excess amount of material.

The second parameters characterization test is the acceleration-deceleration printing test. This print path prints only one filament and has a consistent flow rate,

however, the nozzle travel speed changes within the single row. This test characterized the effect of the acceleration and deceleration of the nozzle have on the printed filament. The top view of the print path for this test is shown in Figure 6.2. The travel speed of the nozzle increases from the selected normal printing speed to the support structure printing speed and back to the normal printing speed in a single row. This helps to capture the effect of the acceleration and deceleration of the nozzle travel speed have on the printed filament.

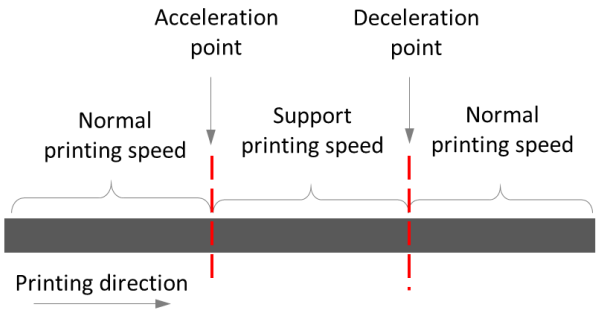

Figure 6.2: The top view of a schematic drawing of the acceleration-deceleration test print path.

6.2.3 Topology optimization

The main aim of this investigation is to determine if the FGCM can to be printed. In order to ensure that the printed sample is a functionally graded material, the carefully engineered continuously varying spatial composition profile must serve a purpose. Topology optimization was performed on the Messerschmitt-Bolkow-Blohm (MBB) beam with a dimension of 450 x 100 x 100 mm. The beam has two simple support at each end and a constant load is applied in the middle. With the initial design, properties of the material and external constraint established, the topology optimization process determines the optimum design by effectively removing elements from the analysis with a software (Abaqus) [147]. Structural

optimization using Abaqus is an iterative design process that refines the part design subjected to design constraints and objectives. The result of the structural optimization would produce a lightweight and rigid part, that can bear the same structural load as its original unoptimized design. The concrete beam was modelled using a Concrete Damaged Plasticity (CDP) model. The material model provides general capabilities for modelling concrete and other quasi-brittle materials. It uses an isotropic damaged elasticity in combination with isotropic tensile and compressive plasticity to represent the inelastic behaviour of concrete. The objective function of the optimization is to minimize the strain energy, in effect maximizing the stiffness of the optimizing structure while constraining the volume of the structure [148]. Figure 6.3 (a) shows the schematic drawing of a MBB beam.

All samples were tested with the centre-point loading method on a Universal Instron testing machine (Instron 5969). The experiment setup is shown in Figure 6.3 (b). The loading rate of the samples was in accordance with the ASTM standard [149] where the maximum stress on the tension face increases at a rate of 0.9 MPa/min.

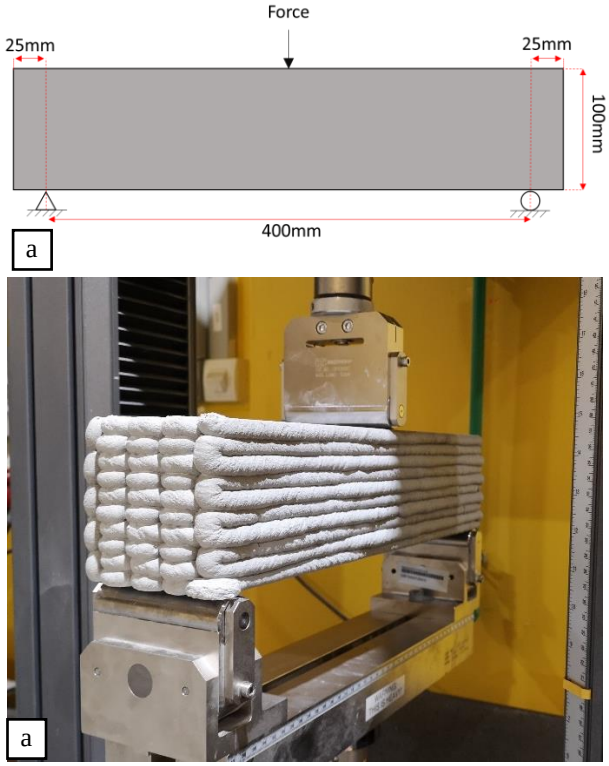

Figure 6.3: (a) A MBB beam with the initial design dimensions
(b) Center-point loading method setup

6.2.4 Printing code generation

The STL files were fed into open source slicing software (Slic3r) to find the boundaries between solid and support regions. These STL files were sliced into layers and the G-code generated from the slicing software is further processed with a Python code before downloading into the gantry printer.

A self-developed Python code was used to extract the boundary information from the generated G-code. The coordinates of the solid and support regions were read from the G-code, then the layer width was added into the solid region to find the real boundaries between solid and support region. Next, the coordinates of these boundaries were used to generate the printing code of the parts, as shown in Figure 6.4. For a solid region, the nozzle travels with a slow speed. For the support region, the nozzle travels with a fast speed. In some sections of the solid regions, the width

of the section is not large enough for two filaments, then the nozzle will travel at the slower speed to fulfil the required section width.

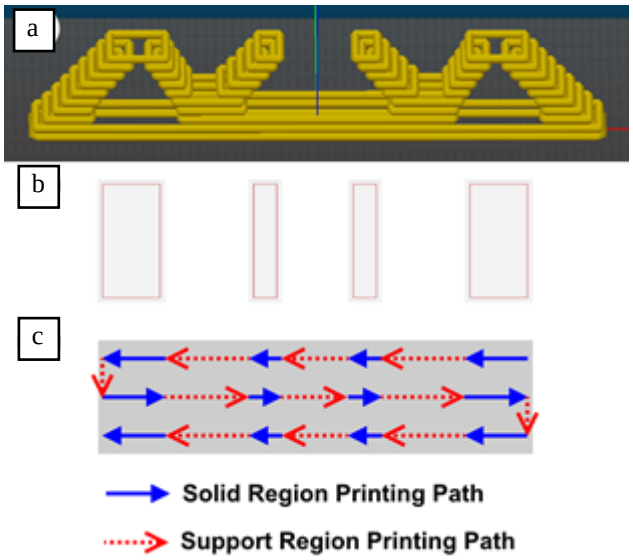

Figure 6.4. (a) The slicing preview of the first 10 layers. (b) The Slic3r generated G-code showing the solid regions of the 10th layer. (c) The longitudinal printing path for the 10th layer generated from extracted boundary coordinates with slowed down nozzle travel speed for some of the sections.

6.3 Results

6.3.1 S-shape printing test

The investigations of the s-shape printing test protocol gave an insight into the behaviour of the extruded material with different printing parameters. Three of the seven s-shape printing result were shown in Figure 6.5 that shows the effect of the filament by varying the printing parameters. A total of 49 different filaments were printed with different material flow rates and nozzle travel speeds. Similar to the existing literature [11], the breakage in the filament increases as the travel speed increases or the flow rate decreases. This increase in travel speed or reduce in flow rate decrease the solidity ratio (SR). As defined in the previous work [11], the SR is

the expected filament size. When SR is more than 1, a larger filament is expected. When SR is lesser than 1, the filament will show more discontinuity and breakage [11]. However, instead of quantifying the results with the SR value, a dimensionless value ($R_{m/i}$) is introduced. The SR value is the ratio of the different volume flow rates, whereas $R_{m/i}$ is the difference in the surface area. Due to the material brittle nature, breakages tend to appear in the filaments, and this makes the quantifying of the filament difficult. Thus, capturing the top surface area seems to be a possible solution to quantify the filament extruded.

Although the s-shape printing test has been carried out in previous research [11], the nozzle in this investigation has a different geometry. The size of the nozzle used in this study is much smaller. In order to achieve SR = 1, without changing the travel speed, the flow rate has to reduce.

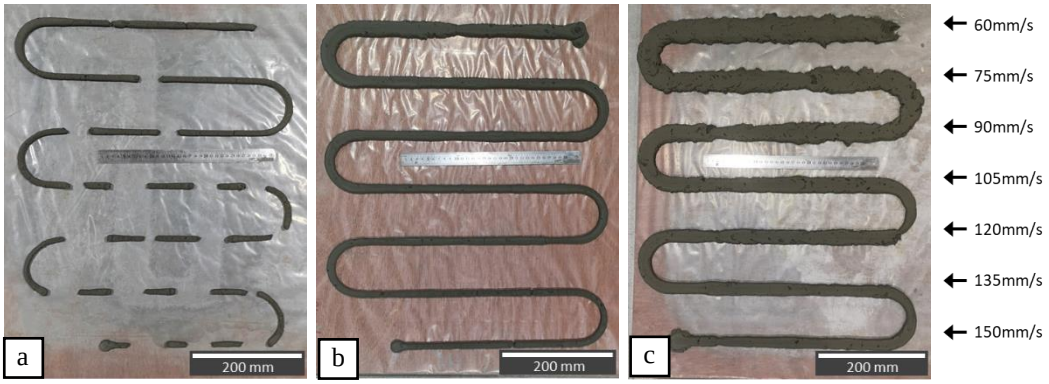

Figure 6.5: S-shape printing with round nozzle (a) 6 ml/s (b) 12 ml/s (c) 22 ml/s

The $R_{m/i}$ value of the filament shown in Table 6.1 was obtained using imaging software (ImageJ) with the results in Figure 6.5. Based on visual inspection, the filaments were separated into different regions as denoted by the different colours of shading as shown in Figure 6.6. The examination to separate the $R_{m/i}$ into the different regions were recorded in the previous literature [11].

It is observed that as the $R_{m/i}$ values exceed 2.2 in the oversupply region, bulging starts to appear on the filament. These intermediate bulging showed in Figure 6.5 (e.g. travel speed of 60 mm/s, 70 mm/s and 90 mm/s) can cause dimension inaccuracy in the printed filament. Unless these bulging can be controlled to print impression on a wall, such bulging is deemed as a failure region.

Table 6.1: $R_{m/i}$ of filament obtained from ImageJ

	60 mm/s	75 mm/s	90 mm/s	105 mm/s	120 mm/s	135 mm/s	150 mm/s
24 ml/s	3.49	2.91	2.46	2.08	1.89	1.63	1.52
22 ml/s	3.20	2.64	2.24	1.93	1.74	1.49	1.44
19 ml/s	2.44	2.17	1.80	1.52	1.35	1.19	1.13
16 ml/s	2.19	1.86	1.49	1.36	1.18	1.08	1.00
12 ml/s	1.87	1.44	1.26	1.07	0.97	0.83	0.78
9 ml/s	1.39	1.29	1.02	0.92	0.84	0.79	0.75
6 ml/s	1.00	0.74	0.61	0.52	0.46	0.40	0.39

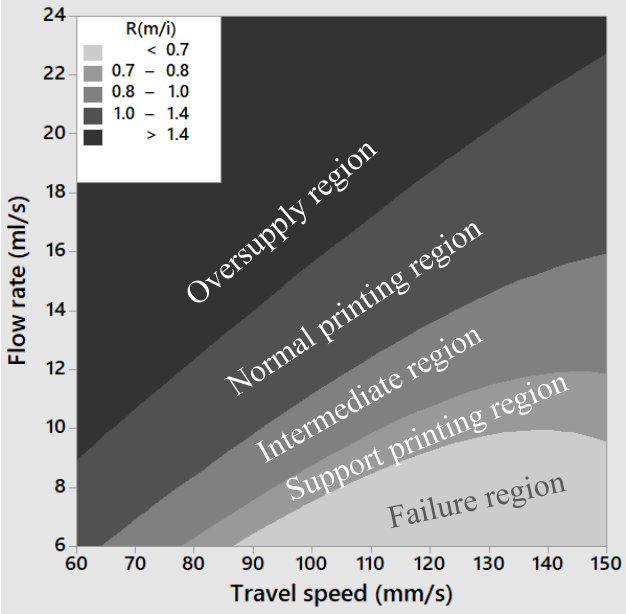

Figure 6.6: Contour plot of the $R_{m/i}$

6.3.2 Acceleration-deceleration printing test

The change of the travel speed will cause acceleration or deceleration of the nozzle as shown in Figure 6.7. This acceleration and deceleration at a constant flow

rate cause the filament to have a transition region. If there is no adjustment accommodate to this acceleration and deceleration of the nozzle speed, the structure printed may not achieve the actual dimensions. For this investigation, in order not to compromise the structural integrity, printing the normal section is more important. Therefore, the actual deceleration of the travel speed has to start before the start of the deceleration point shown in Figure 6.7(c). The distance that needs to be compensated is illustrated as the lag distance shown in Figure 6.7(c).

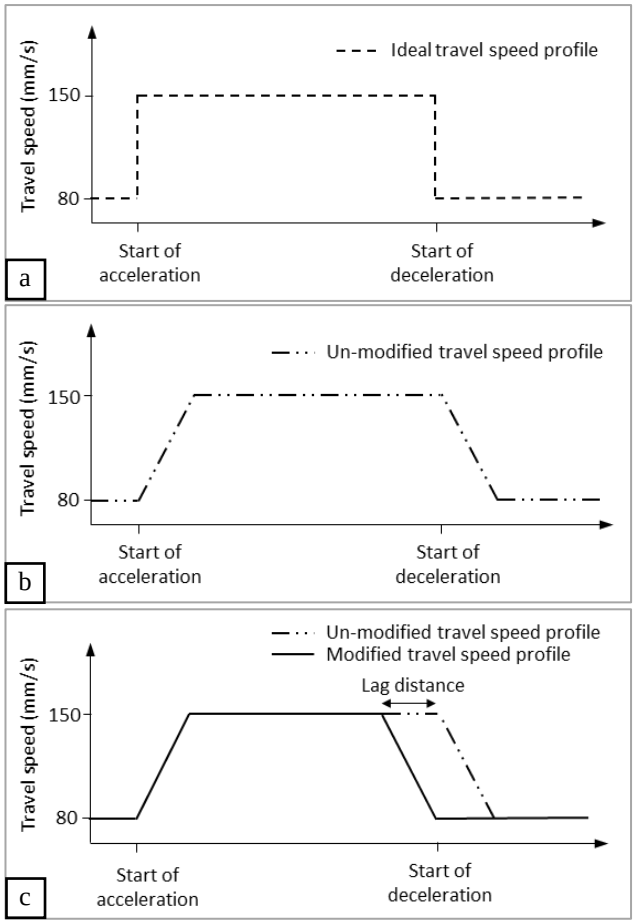

Figure 6.7: (a) Ideal travel speed profile of the nozzle (b) Travel speed profile of the nozzle without modification (c) Travel speed profile of the nozzle with modification

From the results in the s-shape printing, the printing parameters were chosen to be 10 ml/s at 80 mm/s and 150 mm/s for the normal printing and the support

printing respectively. With the printing parameters known, the acceleration and deceleration printing test can be carried out and the results were shown in Figure 6.8. The acceleration and deceleration transition regions were marked by the red lines and the distance between the lines was measured using an image processing software (ImageJ). From the test result, the acceleration and deceleration cause a tapered filament to appear in this region. The length of this tapered region for the acceleration and deceleration is 16.06 mm and 19.73 mm respectively.

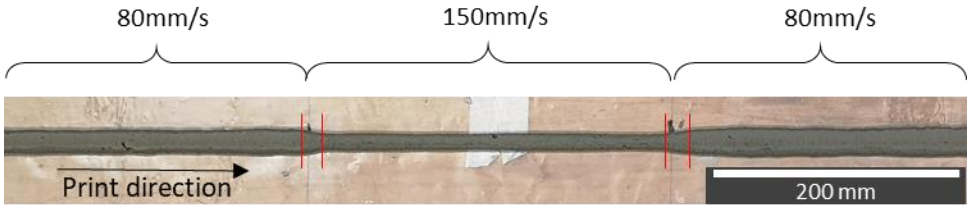

Figure 6.8: Acceleration-deceleration printing test

From the results obtained, it can be observed that both the acceleration and deceleration have a transition region which starts near to the mark where the acceleration or deceleration begins. Printing without consideration of this acceleration and deceleration region can cause the support region and the solid region to deviate from its position and may cause the stresses from the loading to fail at a weaker region resulting in a weaker structure. Especially for the deceleration region, the lag distance is added into the code to accommodate this delay. On the other hand, no modification has to be made to the acceleration point since it does not affect the normal printing region.

6.3.3 Topology optimized structure

The topology optimization was performed on a software (Abaqus) in two dimensions (2D). The 2D model is prepared in Abaqus which represents the initial design space of a conventional beam that to be tested under a centre-point loading setup. This initial design space measures 450 mm x 100 mm. In order for it to be printed and for actual measurement of the flexural strength, the depth of the sample was given the same length as the height of 100 mm. The objective of the topological optimization is to find the material distribution with a volume constraint in the given initial design domain such that the structure is the stiffest.

Mesh size can influence the results of the Abaqus analysis such as stress, displacement and energy. As the results are sensitive to the mesh size, it is reasonable to assume that the finer the mesh, the more accurate the results. However, the finer mesh would also result in a higher number of elements that requires more computational effort. An optimal mesh size conducted through a mesh sensitivity analysis would determine the optimal mesh size while maintaining a reasonable tradeoff between accuracy and computation time. As shown in Table 6.2, using a mesh size of 20 mm will produce a model with 110 elements, while a 3 mm mesh size will produce a model with 4950 elements. Looking at the result of the max stress, it has converged at a mesh size of 5 mm. Therefore, topology optimization would be conducted using a mesh size of 5 mm. The 2D model is mesh into 1800 numbers of elements with a load of 50N applied as a single load case.

The results of the topology optimization converged, with different volume constraint, after numerous iteration giving a detailed shape of the final figure and were shown in Figure 6.9. The optimization results shown gives a new design layout

with internal ribs as links between the loading point and the support points. The areas that do not contribute to the stress loading are removed and appear as voids. It is evident from the result that the topology of the structure has the same contour among the different volume fractions for the 2D optimized structure.

Table 6.2: Mesh size and total element analysis.

Mesh size (mm)	Total elements	S, Max in plane stress (MPa)
20	110	1.80248
15	210	1.80019
10	460	1.80048
5	1800	1.80034
3	4950	1.80035

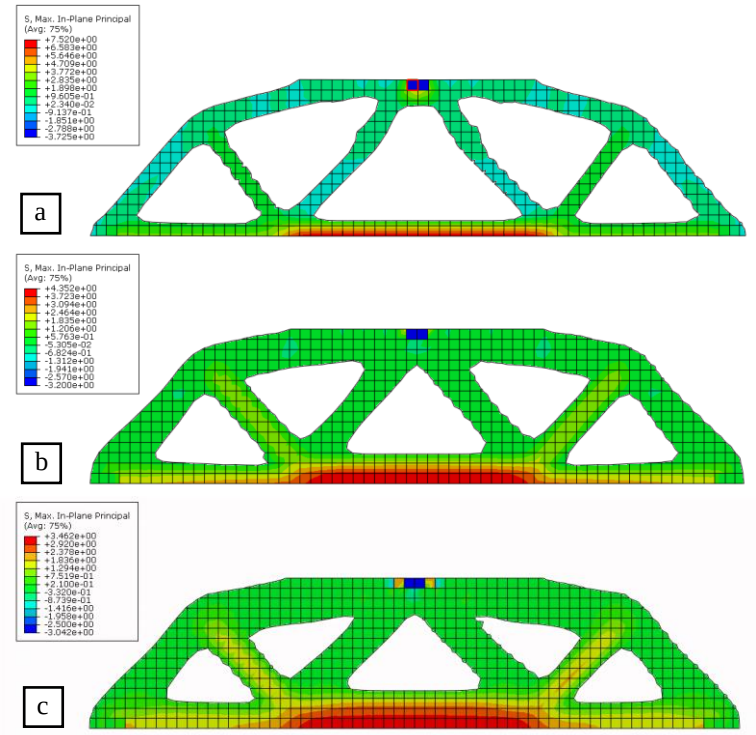

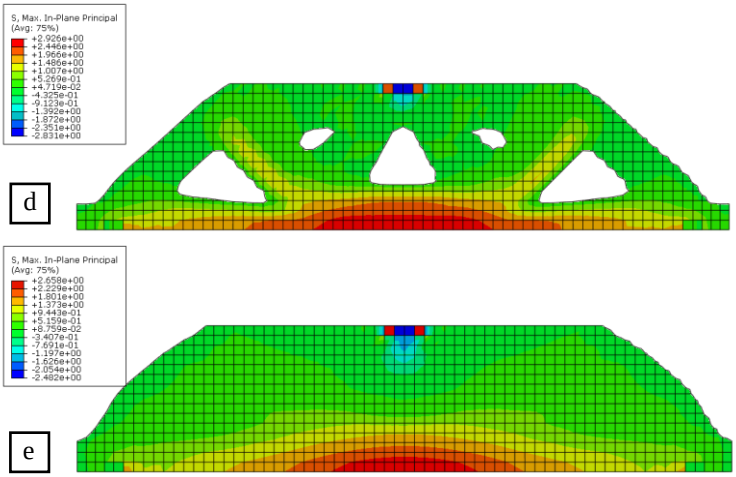

Figure 6.9: 2D optimized beam structure for volume fraction of (a) 20% (b) 40% (c) 50% (d) 60% (e) 80%

Figure 6.10 shows the collated result of the maximum stress in tension experienced by the different structure at different volume constraint given a constant load. From Figure 6.9, the maximum stress concentrates at the bottom surface of the model. This proves to be the weakest region in the whole structure. Therefore, to increase the strength of the region, the thickness of the material at the region increases as the volume permissible increases. As the internal ribs widen with an increase in the volume constraint, the maximum stress reduces. From Figure 6.10, the maximum stress of the structure with less than 50% volume fraction constraint deviates more than 30% from the 100% structure. From 60% structure onwards, there is lesser than 10% deviation in the maximum stress. In order to achieve a high strength structure, the maximum stress experienced by the structure should be as low as possible. Therefore, the 60% volume fraction constraint structure is chosen as the optimum structure to be printed. Additionally, the 80% volume fraction constraint structure was printed to determine if the topology optimized 60% structure has an advantage

when compared to the 80% structure without the inner voids in terms of strength-to-weight ratio.

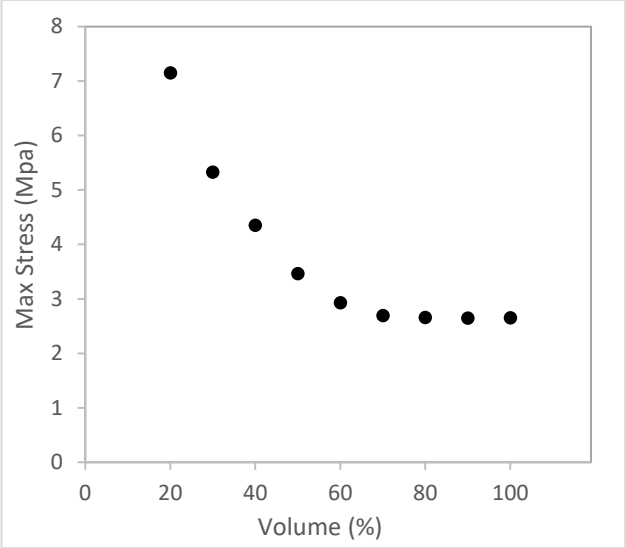

Figure 6.10: Maximum stress at different volume for the 2D optimized structure

Results of the topology optimization are refined and smoothened in a software (Solidworks). The 2D model was converted to a 3D model using the extruded function in this software by 100 mm. The part file in Solidworks was converted into an STL format file for processing in the SLIC3R software. The voids in the 60% structure will be printed with a support material as described in Section 6.2.1. After slicing the model in the SLIC3R software, the optimized model was modified at this stage to account for deceleration lag distance described in Section 6.2.2. The finally optimized model ready for 3D concrete printing is shown in Figure 6.11. The rib of the optimized structure can also be clearly seen from the contour of the surface of the 60% structure (See Figure 6.11 (c)) when comparing to the 80% structure (See Figure 6.11 (b)). The strength and weight ratio will be used as an indicator to determine the improvement of using such printing technique. Furthermore, in order to have a control sample, a beam with a dimension of 450 x 100 x 100 mm (L x H x

W) was cast. This allows the printed samples to be compared with the conventional method of manufacturing.

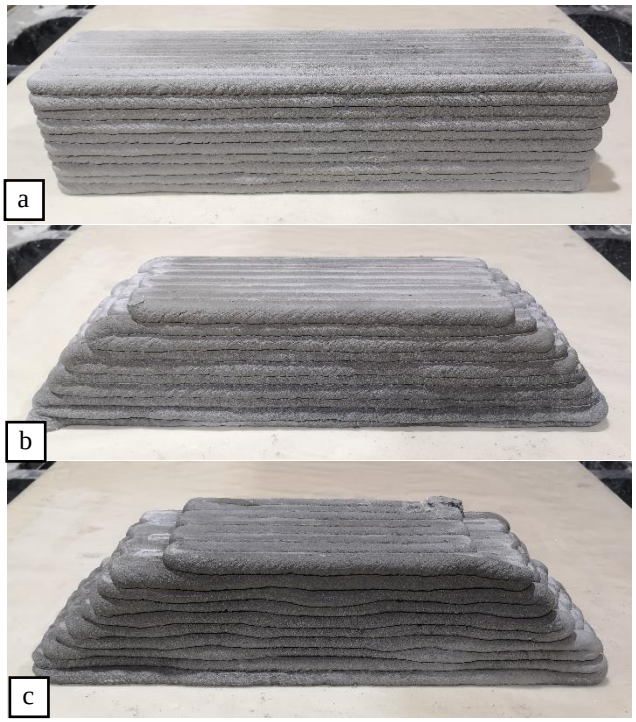

Figure 6.11: 3D printed structure in the longitudinal direction with a volume fraction of (a) 100% (b) 80% (c) 60%

6.3.4 Validation of results

Four different samples were prepared for comparison. A 100% beam was cast (100%C) and printed (100%P), a sample with 80% of the volume fraction (80%P) was printed and the sample with the 60% volume fraction (60%P) was printed along the longitudinal direction. Figure 6.12 shows the fracture of the different samples. In the flexural test, the samples were subjected to a bending motion. This motion causes the top half section to be in a compression condition and the bottom half to be in a tensile condition. Since concrete is a weak material under tensile loading, cracks usually start to propagate from the bottom in the middle directly under the centre of the loading.

As shown in Figure 6.12, all of the samples fail in the middle section. From Figure 6.12 (a)-(c), it can be seen that the samples have a flat crack across the fracture surface (in the x and z-axis direction). Although printed with different volume fractions, the fracture surface for Figure 6.12 (b) and (c) seems similar, with the iconic voids in-between the filaments when round nozzle used. These voids between the filament are created due to the geometrical shape of the round nozzle which created rounded filament. Additionally, the cross-sections of the filament in Figure 6.12 (b) and (c) have a consistent geometry throughout the structure. However for Figure 6.12 (d), the crack propagation is different, the crack propagation in the z-axis direction is independent of the x-axis. Furthermore, the cross-section of the filaments does not have the same geometry thought the structure. The filaments were more compact at the top and bottom surface and more loosely packed in the middle range. Moreover, the filaments in Figure 6.12 (d) seem to be stacked in individual columns and not in contact with the neighbouring column as shown in Figure 6.13.

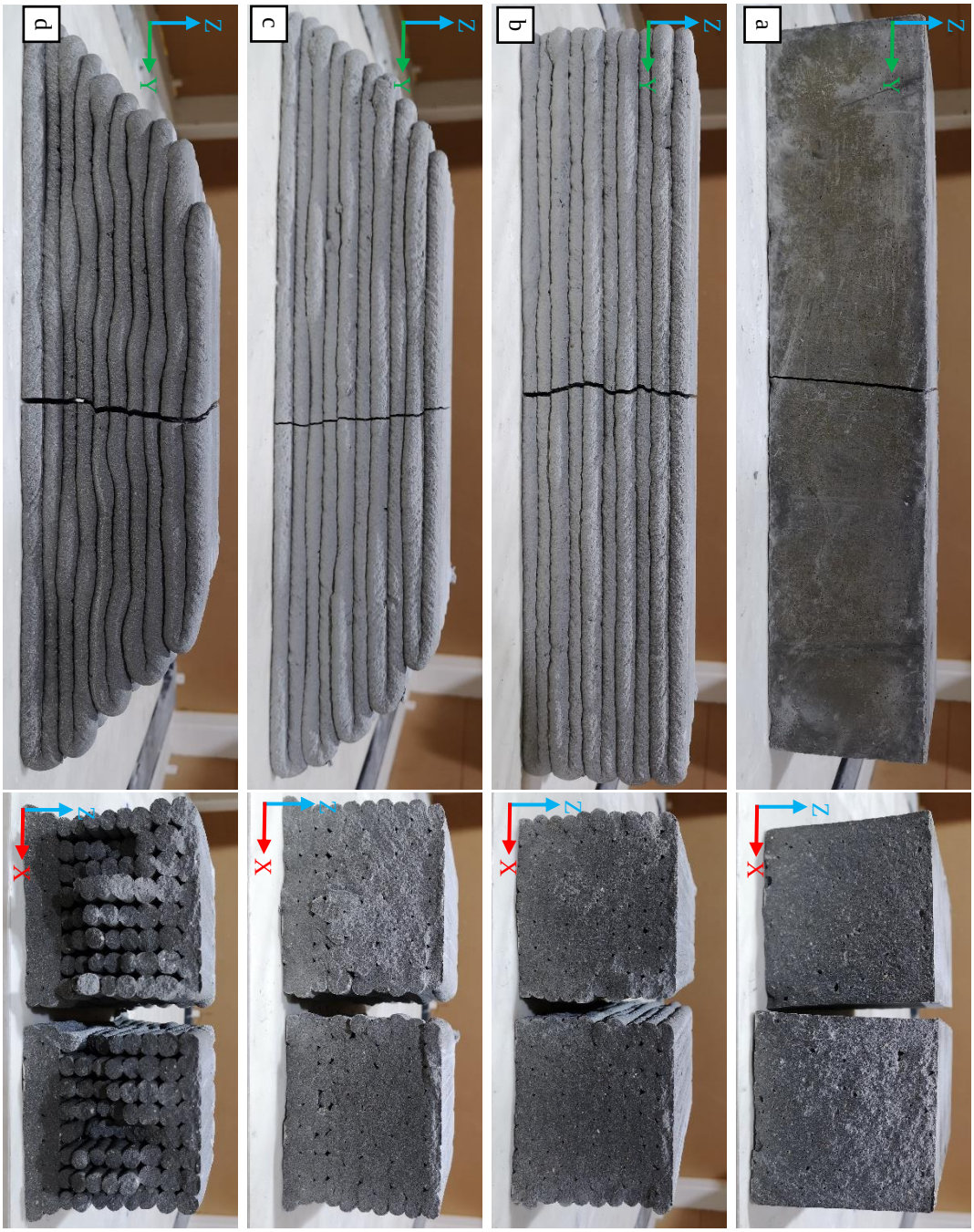

Figure 6.12: Photo of tested samples (a) 100%C (b) 100%P (c) 80%P (d) 60%P

The flexural strength, weight of the samples and the strength-to-weight ratio are shown in Figure 6.14. The weights of the 100%C and 100%P are comparable, however, there is a reduction of 35% in flexural strength for the 100%P sample. This decrease in the flexural strength of the printed sample reduces the strength-to-weight

ratio significantly since the weight of the samples is similar. However, as the structure volume fraction reduces, the strength-to-weight improves.

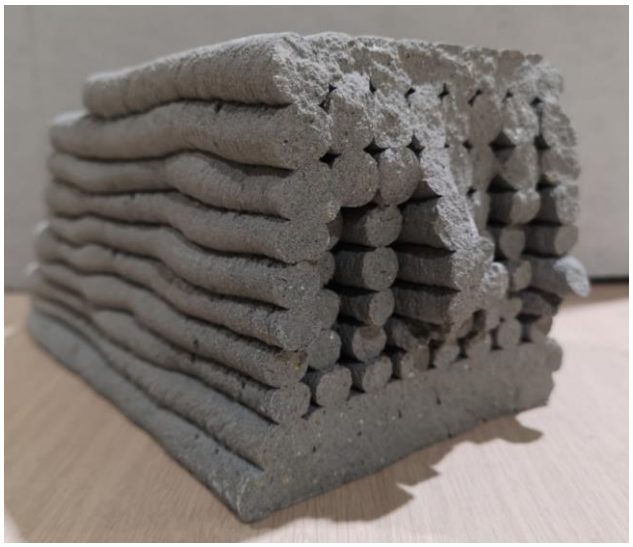

Figure 6.13: Diagonal view of the 60%P sample

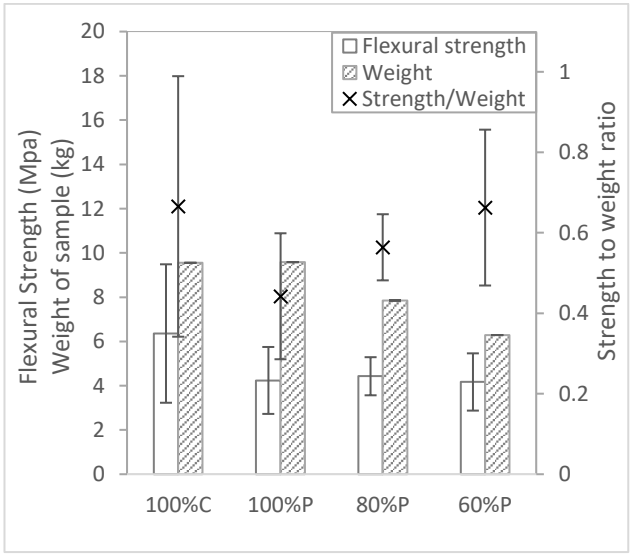

Figure 6.14: Flexural strength, weight and the strength-to-weight ratio of different samples

6.4 Discussion

Although the s-shape experiment protocol was established in Chapter 5, there is a difference in the investigation results. The nozzle used in this investigation has a

different geometry to help navigate through the tight corners in the optimized structure. Although a rectangular nozzle is able to print filament with high stability and able to provide high contact surface area between the top and bottom layer, it is not able to print complex model with high resolution as compared to a round nozzle. The round nozzle is able to follow more closely to the complex path than the rectangular nozzle. Due to this reduction in the size and shape of the nozzle, it was observed that the range of $R_{m/i}$ value is much higher than the previous research as shown in Figure 6.6. This high $R_{m/i}$ value causes the material to flow in the direction perpendicular to the printing path and this phenomenon was not observed in the previous investigation. As the $R_{m/i}$ increase beyond 1.4, these excess materials that are flowing in the direction perpendicular to the printing path are causing the material in the middle to be more compacted which will result in low voids and high strength. The investigation shows that the filament with $R_{m/i}$ value more than 2.2 shows significantly more intermediate bulging. This material flow in the perpendicular direction causes the filament to have intermediate bulging which can cause dimensional inaccuracy and should be avoided unless the bulge position and size can be controlled. On the other hand, the filament that has a lower $R_{m/i}$ ($R_{m/i} < 0.8$) have lesser material extruded out, thus causing more voids in the printed filament and can indirectly cause the printed structure to have lesser strength.

Additionally, the acceleration-deceleration test was carried out with the selected printing parameters to print the normal and support region of the structure. The results concluded that the travel speed's deceleration region is more prominent that the acceleration region. This deceleration needs to be adjusted so that the rib of the optimized structure will not be compromised.

The topological optimization of an MBB-beam problem was carried out with different volume fraction constraint. With the initial design, properties of the material and external constraint established, the topology optimization process determines the optimum design by effectively removing elements from the analysis. The result shows that the structure with 60% volume fraction has the best result with it experiencing only 10% more stress than the 100% structure. The structure that has less than 60% volume fraction shows a higher deviation. The results obtained from the s-shape printing test, acceleration-deceleration test and topology optimization result were used to generate the code for printing.

The decrease in the weight of the sample is due to the different type of material property being printed. Rm/i is a dimensionless value proposed to determine the size of the filament. The filaments with different Rm/i value were shown in Figure 6.5 and Figure 6.6. This difference is due to the change in the printing parameter. High Rm/i value occurs when there is an excess of material being extruded per unit length of filament, which means the filament is more compacted and have a higher strength as compared to filament with low Rm/i value.

By comparing the Figure 6.11(b) and (c), the contour of the optimised rib can be easily identified. These contours of the rib in Figure 6.11 (c) are printed with a higher Rm/i value filament and the concave surfaces of in Figure 6.11 (c) are printed with a lower Rm/i value filament. The lesser material is extruded in these concave surfaces of the structure causing the weight of the structure to be lesser. This change in the Rm/i value of the printed filament within the structure is the reason for the difference in the weight between the 80%P and 60%P sample.

From Figure 6.12 (b) and (c), it is observed that 100% and 80% sample have a similar cross-section in the middle of the sample. This similarity is due to the same printing parameter (flow rate and travel speed) used for these two samples. The only difference is the material that is not printed at the top corners of the 80% sample. Through topology optimisation, these two corners were identified as the low-stressed region which is not used effectively and can be removed [150]. This removal of the material causes weight reduction without affecting the strength of the structure.

The 80% sample and the 60% sample cross-section can be seen in Figure 6.12 (c) and (d), respectively. The first two layers at the bottom for all specimen has the same printing parameters. It is printed with a stronger material property to withstand the load. This is where the stress concentrates as shown in Figure 6.9. The crack formation also begins from these bottom layers. Furthermore, through topology optimisation, the rib and frame structure as shown in Figure 6.11(c) are the region that is more critical. These ribs ensure that the structure has a maximum stiffness at 60% volume constraint.

The existing literature investigating cracking of concrete mostly revolves around homogenous concrete on microscale [151], [152] and has limited research on fracture analysis on non-homogenous concrete, especially in 3D concrete printing. The existing studies on homogenous concrete analyze the fracture mechanism to determine the necessary condition for the propagation of an existing flaw. In a homogenous concrete, the propagation of a crack under loading is influenced by the properties of the cementitious paste and the heterogeneity of the concrete [152]. However, the cementitious paste and heterogeneity of the concrete are also influencing the crack propagation in non-homogenous concrete. For the non-

homogenous concrete such as 100%P and 80%P sample, the structure can only be seen as a homogenous material in the direction of the print path but the arrangement of the matrix in the filament could be different from the concrete manufactured by the conventional casting method. On the other hand, the printed material in the other direction has an interstitial void between the filaments and could possibly have crack lines appearing between the filaments if the time gap is significantly large [72], [153]. Although these filaments have abnormalities such as voids and cracks in the x and z-axis, the close filament in contact in the x-axis has influences on the crack propagation on the neighbouring filament in the x-axis.

Although there is no obvious crack line appearing between the printed filaments, the interaction between these filaments is still relatively unclear and should not be seen as a homogenous mixture between the two filaments. Whereas in a homogenous mixture an existing crack will propagate rapidly through the material if the total energy supplied by an external force and the change of the stored strain energy is more than the total energy required for the formation of the new crack [152]. Furthermore, it was found that the crack did not propagate as one single crack [154] but was formed through many micro-cracks in the paste content [155]. These micro-cracks are present in the matrix and the matrix-aggregates interface even before any load was applied. Since 3D printing is a process without compaction, there could be a possibility that there are more micro-cracks present in the matrix thus resulting in a much lower strength as shown in Figure 6.14.

From Figure 6.12, the cracks for 60%P samples are much different from the rest of the samples. The cross-section of the printed structure in Figure 6.12 (d) shows how the support filament is printed as the layer progress. The first few layers at the

bottom were printed as the normal filament. This few layers have the same characteristic as the filament printed in 100%P and 80%P samples. They are more compact than the support filament. Furthermore, the crack propagation of these few layers affects the crack propagation of the neighbouring filaments. However, as the layer progresses, the support filament starts to separate from the neighbouring filament along the x-axis. The damage evolution process in the tension direction is that the crack nucleates around the voids and propagates through the weak ITZ [151]. The crack tip usually propagates thought the weakest region of the concrete. Since the filament is not in contact, there is no influence of the crack propagation direction on the neighbouring column thus these columns have a different crack route as shown in Figure 6.13.

The analysis of failure mechanism is important so that solutions can be designed to develop strategies to prevent them in future for homogenous concrete. However, there are limited resources on the failure mechanism of a 3D printed concrete. Furthermore, while the topology optimized structure can be 3D printed to develop materials that have a higher strength-to-weight ratio, it is important that extra caution to be taken during measurement of the flexural strength, since the optimized structure is very sensitive to the loading condition and constraint. Misplacement of the sample can cause the loading to be different thus causing the stress distribution in the rib to be different which may result in a lower strength value.

6.5 Chapter summary

In this investigation, the feasibility of printing a functionally graded structure was tested by varying the flow rate and travel speed to print the main structure and support structure. The effects of printing parameters on 3D printed concrete were

conducted and it was shown that the flow rate and travel speed play a huge role in the effects of the filament dimensions. The main advantage of having a functionally graded structure is the reduction in material and the decrease in printing speed as the support structure region uses less material and helps reduce printing time. From the results obtained in Section 6.2.1, 6.2.2 and 6.2.3, a functionally graded structure was printed. This shows that through topology optimization, this functionally graded material can be manufactured to produce a structure that has improved performance compared to the un-optimized structure.

This experiment was carried out on a 3D structure printed with a 2D optimized design which has a consistent cross-sectional area in the X-axis direction. The challenge for printing 2D optimization is the overhanging elements which need to be addressed carefully, otherwise, such element can collapse. Furthermore, the intricate design of the 2D optimized structure requires correct planning on the acceleration and deceleration of the nozzle or the structure may become distorted and can jeopardize the structural integrity of the printed structure.

These challenges in the 2D structure need to be addressed properly and hastily testing with the 3D optimized structure without properly addressing these challenges will cause the whole experiment to fail. The use of 2D optimized structure in this preliminary study is only for the proof of concept and should be done before further exploration is useful. Therefore, this study did not explore the 3D optimized structure, however, with the promising result in the 2D format, this research can be further explored in the 3D format. In the 3D optimized structure, the connection between the internal structures are in the consideration and will be different from the 2D optimized structure. Furthermore, 3D optimization will increase the number of

iterations which will increase the time needed to perform the optimization process. This optimized 3D model may result in a structure more complex than the current 2D format. However, the printing code generation and the printing process will remain similar. This printed structure may resemble the simulated optimized design and may not be a full replicate of the actual design due to the resolution of the printer. It is important to note, however, that 3D concrete printing is still in the early stage for implementation. Rigorous testing is necessary before it can be used for any real application. Furthermore, concrete with internally optimized structure does not exist in the market yet. However, this result for the 2D structure looks promising. This investigation work is in its preliminary stage and more work needs to be carried out in this area before it can be used for real applications.

The use of functionally graded concrete has many applications in the building construction industry. For example, having a functionally graded floor slab will lead to a considerable reduction in the weight as well as the material used. The area subjected to low compressive strength could be made up with high porosity concrete while area subjected to high compressive strength should be made up with low porosity concrete. Furthermore, the functionally graded wall can be used for this application where the gradual change in density and porosity within the wall will allow the differentiation in the load-bearing wall and the non-load bearing wall which can ultimately reduce the dead weight of the building.

To the best knowledge of the author, there is little literature available with regards to structural optimization on MBB beam with concrete material. this is due to the fact that the manufacturing method to such beam is costly and it is practically impossible previously without 3D printing. This study opens the realm of possibility

for the future work in 3D functionally graded concrete. Future work relates to the FGCM will be discussed in Chapter 8.

Chapter 7: Large scale 3D concrete printing

7.1 Introduction

It is more demanding on the material property to print a large-scale object than to print a small-scale item. The material needs to deliver over a longer distance due to the printer size that will result in an increase in the pressure difference in the hose. This higher pressure in the hose will increase the segregation requirements of the material [49]. Furthermore, the increase of the object size could increase the path length needed to be travelled per layer, resulting in the time gap to increase and could potentially reduce the interlayer bonding strength.

In this chapter, the printing of a large non-structural prefabricated bathroom unit (PBU) with a size of 1620 mm x 1500 mm x 2800 mm (LxWxH) was demonstrated. Figure 7.1 shows the KUKA 6-axis robotic arm printer (KR120 R3900). A rotatable nozzle was specially designed to avoid twisting of the filament at corners and turns of the printing path. Furthermore, a progressive cavity pump (MAI Pictor pump) was used to deliver the material from the reservoir to the nozzle via a 10m hose as shown in Figure 7.1.

Figure 7.1: Robotic arm printer used for large scale printing

Additionally, a rheological test is established to determine if the material is suitable for this large-scale printing. Addition of admixture can improve the buildability of a material. The addition of the admixture changes the reaction of the cement drastically. The dormant phase is shortened from hours to minutes and immediately after addition, the setting of the concrete starts [156]. The behaviour of this reaction can be captured by the rheometer to determine if the material rate of stiffening is sufficient to support the subsequent layers.

7.2 Materials and methods

7.2.1 Materials and preparation

Dry materials were prepared beforehand and packed into bags of 25kg. During printing, the dry materials were pre-mixed in a pan mixer (SoRoTo 80L mixer) to ensure it is homogeneously mixed. Then, water and additives were added to the dry mixture and were mixed before transferring to the reservoir of the pump. Since this project is a collaboration with an industrial partner, detail material composition will not be disclosed. However, the information on the material properties such as the compressive, flexural and tensile strength can be disclosed and are 30 MPa, 4 MPa and 0.8 MPa respectively.

7.2.2 Full-scale printing

The requirements for printing this PBU were given by the industrial partner. The dimensions of the overall size 1620 mm x 1500 mm x 2800 mm (L×W×H) with the wall thickness of 100 mm and a door opening of 2200 mm x 900 mm are the requirements. Furthermore, the inner structure of the PBU wall should use a lattice

design to save materials as well as to reduce the weight. The lattice design should be wide enough for plumbing pipes to be hidden in the wall.

These requirements from our industrial partner established the printing parameters required. In order to increase the contact surface between the lattice and the structure, as well as to make space of the plumbing pipes, the design as shown in Figure 7.2 was used. Additionally, a square nozzle of 20 mm was chosen to keep the wall thickness within the 100 mm limit which also gives a layer thickness of 20 mm.

Figure 7.2: Lattice designed for PBU printing.

Due to the limitation of a 6-axis robotic arm spherical work envelop, the full-size PBU is not able to be fitted into the robot workspace. The PBU model was therefore printed in two parts with a height of 600 mm and 2200 mm. The distance of the printing path for each layer is 18 m for the 600 mm part and 15 m for the 2200 mm part. This is because the 2200 mm part has a door opening of 900 mm in width and 2200 mm in height. Once the printing parameters have been established, the material can be tailored to meet the requirements.

7.2.3 Rheological test

With the printing path and the travel speed of 100 mm/s established, the stress acting on the filament due to the addition of layers can be determined. This allows the tuning of the material by adding an additive to improve the hydration process and increase the stiffening rate of the filament. To test if the material can be used for large scale printing, a rheological test was performed to analyses if the material is suitable to support subsequent layer. The stress acting on the material in the vertical direction increases in a stepwise function with the addition of every layer. This stepwise function can be replicated with a linear ramp as shown in Figure 7.3. This replicated linear ramp increases in the loading stress, σ, experience by the bottom layer can be defined by Equation 7.1.

$$\sigma = \rho g h(t) \qquad \text{Equation 7.1}$$

where ρ is the density of the specimen, g is the gravity and h(t) is the printing build rate which is defined as the rate of increase in the height of the structure as shown in Equation 7.2.

$$h(t) = \delta_t / t \qquad \text{Equation 7.2}$$

where δ_t is the layer thickness, t is the time taken to complete one layer. This shows that the vertical stress experienced by the bottom layers is dependent on the layers added above.

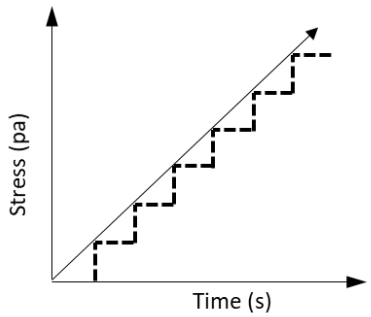

Figure 7.3: Schematic diagram of the stepwise function and the linear ramp of the loading stress

The static yield stress of cementitious material is defined as the minimum stress required to initiate flow from rest [157]. This yield stress originates from the microstructure of the cementitious suspension which has a network of powder particles and early nucleation of hydration product that builds up with time [91]. This change in the yield stress of the material over time due to hydration can be used to determine if the material is suitable for the printing speed.

A rheometer (Anton Par MCR102) as shown in Figure 4.1 is used to obtain the static yield stress of the mix design with different dosage of admixture. A low shear rate of $0.1s^{-1}$ is applied to the specimen for 2 mins. This test is carried out on a single batch of materials at 15-minutes, 30-minutes, 45-minutes, 60-minutes and 75-minutes mark after water is added to the mixture.

7.3 Result

7.3.1 Rheological testing

Based on the calculation of the time required to print per layer for the 2200 mm part and the 600 mm part, the h(t) is 0.48 m/h and 0.4 m/h respectively. Figure 7.4 shows the comparison of the different loading stress due to different h(t), as well as, the yield stress of the material with different dosage of admixture at

different time intervals. At time = 0, the printing process starts, therefore, both the loading stress starts from zero and increases linearly. Since the 600 mm part has a longer distance to cover for each layer, the loading stress has a lower rate. At the same time when time = 0, the material should have ended its mixing and delivery process thus the first yield stress appears at time = 0.

As time increases, the increment in the vertical stress remains constant for both build rates. On the other hand, the yield stress of all the material increases in an exponential behaviour. The increment behaviour of the yield stress for all sample is a result of the flocculation of the cement particles and the chemical reaction of the accelerator and the cement particles. Bürge investigated the mechanism of action of aluminium sulphate in cement and found that aluminium sulphate reacts with lime and produces ettringite and aluminium hydroxide [158]. Similar work by Paglia also found that ettringite is responsible for the rapid setting [159]. As a by-product of the reaction, Aluminium hydroxide is formed which is also known to be an accelerator [160].

The loading stress intercepts the yield stress of the mixture with 0% additive and 0.3% additive. This means that the rate of strength development without the help of admixture is not sufficient to support the weight of subsequent layers at the given build rate. With the given build rate, a 0.7% admixture is necessary for buildability.

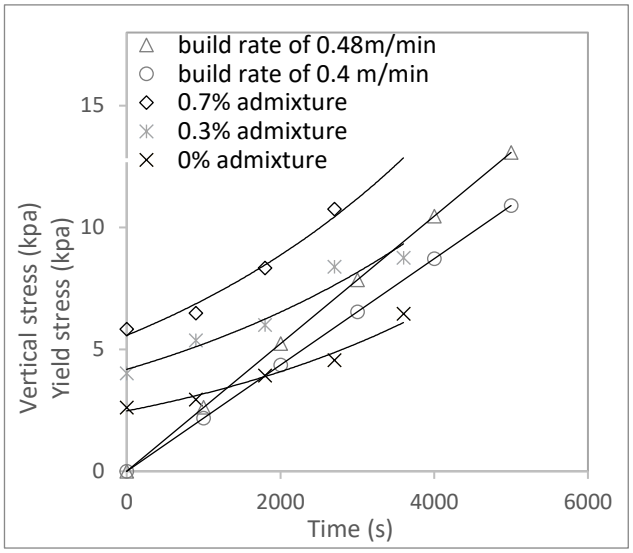

Figure 7.4: Comparison of the materials yield stress and the vertical stress experienced on the bottom layer during printing

7.3.2 Fabrication process

The base slab was positioned within the work envelope of the robotic arm before printing. An adjustment has to be made to ensure that the cast slab is aligned with the print path. A bonding agent (W1, supplied by Warrior Pte Ltd) was applied to the expected printing path on the base slab to improve the bond strength between the base slab and the printed concrete. Figure 7.5 shows the printing process of the 2200 mm part. This part is printed with a door frame thus having a shorter distance to travel for each layer as compared to the 600 mm part shown in Figure 7.6.

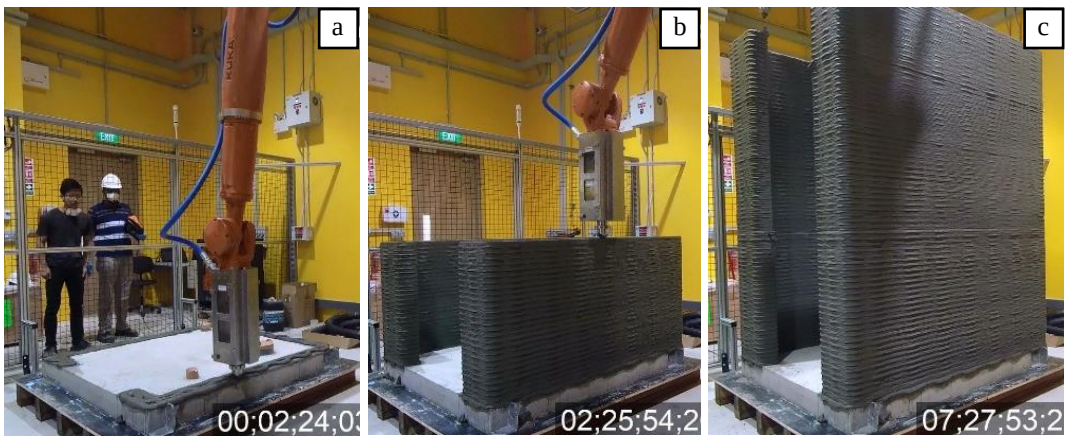

Figure 7.5: Printing process of the 2200 mm part. (a) printing the 1st layer (b) printing the 59th layer (c) printing the last layer

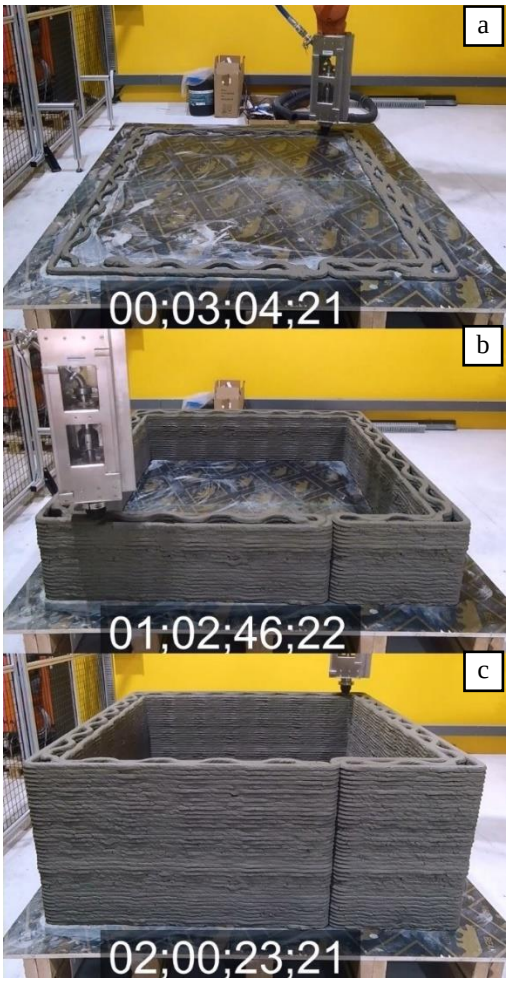

Figure 7.6: Printing process of the 600 mm part. (a) printing the 1st layer (b) printing the 20th layer (c) printing the last layer

After the printing process, both parts were covered with a plastic cover to prevent evaporation of water. A fork-lift was later used to stack the 600 mm part on top of the 2200 mm part. The bonding agent is applied to the top surface of the 2200 mm part to improve the bond strength between the 2200 mm part and the 600 mm part. Post-processing process on the main structure was carried out to incorporate construction work commonly found in the PBU. The post-processing of a 3D printed PBU is the same as the cast PBU as shown in Figure 7.7. The post-

processing starts with casting the door threshold. This threshold is slightly raised to prevent water from flowing out. The waterproof coating is applied to the walls and the floor after the threshold casting is complete. Next, the tiling of the wall and the floor together with the plumbing pipes and floor trap were installed. Lastly, all the sanitary, fittings, lightings and the toilet door were connected.

Figure 7.7: Post-processing after the 600 mm part is stacked above the 2200 mm part (a) casting of the door threshold (b) waterproofing applied (c) tiling of the wall and floor completed (d) post-processing process completed.

7.3.3 Concrete lattice structure

The increased level of control offered by 3DCP enables the use of an advanced computational algorithm to reduce the density of the structure by creating a lattice structure. These optimized structures (see Figure 7.8) not only reduce the overall weight but also improve the use of resources effectively. Beyond economical and architectural benefits, the optimized structure reduces the use of material which could reduce the environmental footprint of the industry. In addition, it can incorporate structural members such as rebar, pre-stressing cable to produce structural concrete [33]. A 3D printed pedestrian bridge [146] is one of the recent examples, where the printed structure was post-tensioned after assembling the individual 3D printed sections.

It is worthy to note that, the traditional optimization software only considers isotropic material properties during the analysis, however for 3D printing projects the part design needs to be finalized whilst taking the properties and limitations of a 3D concrete printer and the material properties into account.

Figure 7.8. 3D printed lattice shape wall element printed in SC3DP, NTU.

7.4 Chapter summary

3D concrete printing can be a complex process, especially if the requirements are unclear. Whether to tune the printing parameters to suit the material characteristics or to tailor the material properties to adapt the printing parameters can be puzzling. In any case, the final decision should depend on the requirement of the project. If the project requirement is to save cost on the material, the printing parameters should tune to suit the material characteristics. However, if the project requirement is to save time, material needs to be tailor to adapt to the fast pace of the nozzle travel speed.

Different printed structure can behave differently to structural failure. It is true that buckling can affect the stability of a printed structure as shown by Wolf et al. [161]. However, according to Gupta and Gautam [162], short column effect can be considered when the ratio of the effective length to the least lateral dimension is less than 12. In this study, the structure printed can be considered as a short column. Although the nozzle size is only 20mm, the lattice design increases the lateral dimension giving support to both walls. This lattice design reduces the ratio of the effective length to the least lateral dimension to 2.2. In this case, the structure generally fails by crushing and not by buckling. This made the yield stress testing more important than the stability criterion thus is it not considered in this study. It is further confirmed in the fabrication process that buckling did not occur.

This chapter illustrated the method used to determine the accelerator content to tune the material property used for large scale printing. The project requirement has to be established before adjusting the rest of the printing parameters as well as

the material property. After the project requirement such the structural size, lattice design and the time frame of the project is established, the printing parameters can be adjusted to fulfil these requirements. Lastly, with the printing parameters such as flow rate and travel speed established, the material can be tuned to meet the stiffening rate required.

Chapter 8: Conclusion and future work

8.1 Conclusion

The main objective of this dissertation is to characterize a printable cementitious material using standardized field-friendly protocols such as the slump and flow table tests. Additionally, pumpability index and surface quality index were introduced to examine the material characteristic. These results obtained were used to evaluate the material suitability for 3D concrete printing. Another objective of this dissertation is to evaluate the printing parameters to determine the different printing region for different operations. The different printing regions allow the structure to be printed with varying properties by changing the printing parameters.

From the material investigation, it is observed that mixtures with low slump values have low buildability due to its pores and discontinuity. On the other hand, mixtures with high slump values do not have the stiffness to support the subsequent layers. Therefore, the middle region between a slump value of 4 and 8 mm and a flow diameter value of 150 to 190mm possess a balance material behaviour ideal for printing. Mixtures having the same slump value may behave differently when stress is applied. The mortar that has high paste yield stress and low-volume fraction of aggregates can have the same yield stress as mortar with low paste yield stress and high-volume fraction of sand. Both mixtures will behave differently when the external stress is applied especially during pumping which could affect the surface finish on the printed filament. It is also found out that some of the material used in the existing literature falls within this acceptable printing region.

The result of the pumpability index in this study was limited to the pump capability. A pump that has a higher pump pressure capability can deliver a stiffer

material. Furthermore, the pump specification limits the size of the aggregates used in this study to 2mm. While a wider or narrower range of material that can be pump depends on the pump capability, this pumpability index result can only be used to compare the different material using the same pump. Different pump power and different rotor and stator condition can produce different pumping capability which may differ the result.

In the printing parameters study, results in Chapter 4, 5 and 6 shows that there is a significant effect on the printed filament by varying the printing parameters. Through finding the different printing regions, different printing parameters can be used to print structure with the different operation. By printing the weaker section of the structure (e.g. support structure), gap and voids could appear in these sections. This causes the gap-distance in the filament to be important. Fresh cementitious material is not able to support itself upon extrusion and tends to slump when there is insufficient support surface underneath. It was found out that this gap distance should be lesser than 10 mm for the sag in the bridging layer to be lesser than 2 mm for the material tested.

A dimensionless value ($R_{m/i}$) was introduced to characterize the different parameters. It is the ratio of the measured surface area to the ideal surface area of the filament. Although the flow rate and travel speed of the printing parameter may be different, it could register the same $R_{m/i}$ value. The proposed method to evaluate the printing parameters for determining the different printing regions is limited to the material and the gantry capability such as the movement rate of the X and Y-axis. Although converting the printing parameter to the $R_{m/i}$ of the filament can help to analyses the printing parameter effectively, such test result is different for different

materials and different gantry capabilities. This test is therefore required to be carried out in order to examine the filament when a different material or printer is used. Concurrently, having the same $R_{m/i}$ can have different time gap which could affect the strength of the inter-bonding layer. It is concluded that as the time between the extrusion of the current layer and the subsequent layer increases, the strength reduces. This is due to the stiffening of the surface in contact with the subsequent layer. As shown in the rheological result in Section 4.4.1 and photos on the macroscopic scale in Figure 4.11, the material stiffness increases as the time increases for the current layer. However, the results in Figure 4.7 shows that the stiffness of the material remains similar for different interval up to 20-minutes. When the time gap is short, the stresses induced by the extrusion of the subsequent layer on the existing layer cause the contacting surfaces to mingle and interact. However, as the time gap increases, the stiffness of the current layer increases, this stress-induced by extrusion of the subsequent layer is insufficient to cause this mingling. Since there is lesser interaction between the layers, more voids appear as time gap increases which also causes the lower inter-bonding strength.

A topology optimized functionally graded concrete material was printed by varying the printing parameters. The effects of printing parameters on 3D printed concrete were conducted and it was shown that the flow rate and travel speed play a huge role in the effects of the filament dimensions. The main advantage of having a functionally graded structure is the reduction in material and the decrease in printing speed as the support structure region uses less material and help to reduce printing time. This shows that through topology optimization, this functionally graded

material can be manufactured to produce a structure that has improved performance compared to the un-optimized structure.

To the best knowledge of the author, there is little literature available with regards to structural optimization on MBB beam with concrete material. this is due to the fact that the manufacturing method to such beam is costly and it is practically impossible previously without 3D printing. This study on FGCM opens the realm of possibility for the future work in 3D functionally graded concrete and has a wide application in the building and construction industry. Having an FGCM will reduce the dead load in the building saving the cost of the additional column for support, at the same time, increasing the space usage saved for such a column.

Besides the material investigation in Chapter 3, a rheological investigation in Chapter 7 was able to determine the accelerator content to establish a suitable material stiffening rate for large scale application. 3D concrete printing can be a complicated process, especially if the requirements are not clear. The printing parameters and material properties should be tailored to fulfil the project requirements such as cost and duration. With the printing path and speed established, the vertical loading stress can be determined. This vertical stress can be compared with the yield stress of the mixture to determine if it is suitable for printing. The stiffening rate of the mixture should be higher than the vertical stress of the printing process otherwise it may collapse under its own weight.

3D concrete printing is a promising technology to address the sustainability challenges in today's construction industry and open up new opportunities for design possibilities. Beyond economical and architectural benefit, 3D printing technology itself is a sustainable solution. The level of control offered by 3D printing can

improve the use of resources effectively. Concurrently, different green materials can be used to amplify the sustainability of this technique. Construction firms need to recognise that sustainable construction is becoming a greater concern. Investing in the latest sustainable technologies and employing passive architectural design can help the company recoup these investment costs over time in the form of decreased building operations as a result of energy efficiency. The future of construction is most likely to be an integrated process that allows the organization to take advantage of both conventional and additive manufacturing technologies. With rapid urbanization in many developing countries, there is an urgent need to come up with clever ideas that optimize the sustainable performance of the buildings that we live and work in. Regulators also play a significant role in sustainable construction by creating the right incentives for companies that choose to build in a sustainable way. Finally, the government can legislate and create mandates that require firms to build in a sustainable way.

8.2 Future research perspective

The research work performed in this dissertation has explicitly dealt with many of the aspects in concrete printing including material and printing parameters investigation. However, there is still a lot of refining work and possible limitations that could be further explored. Below are some of the following aspects are considered relevant for further research.

- The pumpability and the buildability were two of the main focus for evaluating the printability region in the slump and flow diameter chart. Although these two values are sufficient to determine the printability of a mixture, the mechanical

strength of the selected mixture should also meet a certain criterion. It is recommended that future studies can focus on the mechanical properties of the mixture within the printability region.

- The analysis of the printability region can be extended with a range of aggregate gradation. In this dissertation, the focus is to establish a region suitable for 3D printing, therefore only one type of aggregates is used. Evaluating a wider range of gradation can strengthen the work presented in this dissertation.
- Improving the interlayer bond strength while keeping the high modulus of the filament can be explored. Different methods can be used to improve the bond strength, such as increasing the surface contact area of the interface or inducing vibration to the surface of the previous filament before layering the subsequent layer.
- Topology optimisation based on an anisotropic material property. This will require a higher computation memory as the simulation variable is larger and may require a longer amount of time to generate the results. Furthermore, the optimization can extend to 3D design of a topological optimization model instead of a 2D model. By using a 3D model will provide a more realistic simulation of the actual results as compared to a 2D model as more variables are accounted for.

Publications

Chapter 2

1. Y. W. D. Tay, B. Panda, S. C. Paul, N. A. Noor Mohamed, M. J. Tan, and K. F. Leong, "3D printing trends in building and construction industry: a review," *Virtual and Physical Prototyping*, vol. 12, no. 3, 2017.

Chapter 3

2. Y. W. D. Tay, B. Panda, S.C. Paul, M.J. Tan, S.Z. Qian, K.F. Leong, C.K. Chua, "Processing and properties of construction materials for 3D printing," in *Materials Science Forum*, 2016, vol. 861, pp. 177–181.
3. Y. W. D. Tay, Y. Qian, and M. J. Tan, "Printability region for 3D concrete printing using slump and slump flow test," *Composites Part B: Engineering*, vol. 174, p. 106968, 2019.

Chapter 4

4. Y. W. D. Tay, M. Y. Li, and M. J. Tan, "Effect of printing parameters in 3D concrete printing: Printing region and support structures," *Journal of Materials Processing Technology*, vol. 271, pp. 261–270, 2019.

Chapter 5

5. Y. W. D. Tay, G. H. A. Ting, Y. Qian, B. Panda, L. He, and M. J. Tan, "Time gap effect on bond strength of 3D-printed concrete," *Virtual and Physical Prototyping*, vol. 14, pp. 104–113, 2019.

Chapter 6

6. Y. W. D. Tay, J. H. Lim, N. H. A. Koh, M. Y. Li, and M. J. Tan, "Creating 3D concrete functional graded materials with varying printing parameters" Submitted to Journal of Automation in Construction; Under review.

Chapter 8

7. Y. W. D. Tay, B. N. Panda, G. H. A. Ting, N. M. N. Ahamed, M. J. Tan and C. K. Chua, "3D Printing for sustainable construction" presented as a conference paper (keynote in 2nd International conference on sustainable smart Manufacturing (S2M 2019), April 2019, Manchester, UK.

Other journal paper

1. B. Panda, S. C. Paul, L. J. Hui, Y. W. D. Tay, and M. J. Tan, "Additive manufacturing of geopolymer for sustainable built environment," *Journal of Cleaner Production*, vol. 167, pp. 281–288, 2017.
2. S. C. Paul, Y. W. D. Tay, B. Panda, and M. J. Tan, "Fresh and hardened properties of 3D printable cementitious materials for building and construction," *Archives of Civil and Mechanical Engineering*, vol. 18, no. 1, pp. 311–319, 2018.
3. B. Panda, Y. W. D. Tay, S. C. Paul, and M. J. Tan, "Current challenges and future potential of 3D concrete printing," *Materials science and Engineering Technology*, vol. 49, no. 5, pp. 666–673, 2018.
4. X. Zhang, M. Y. Li, J. H. Lim, Y. Weng, Y. W. D. Tay, H. Pham, Q. C. Pham, "Large-scale 3D printing by a team of mobile robots," *Automation in Construction*, vol. 95, pp. 98–106, 2018.
5. B. Panda, S. C. Paul, N. A. N. Mohamed, Y. W. D. Tay, and M. J. Tan, "Measurement of tensile bond strength of 3D printed geopolymer mortar," *Measurement: Journal of the International Measurement Confederation*, vol. 113, pp. 108–116, 2018.
6. G. H. A. Ting, Y. W. D. Tay, Y. Qian, and M. J. Tan, "Utilization of recycled glass for 3D concrete printing: rheological and mechanical properties," Journal of Material Cycles and Waste Management, Mar. 2019.

Conference paper

1. Y.W.D. Tay and M.J. Tan (2018). Influence of admixture on 3D printable construction material. *Proceedings of the SLD4 conference* (1-7). The Netherlands, Delft: TU Delft.
2. Y.W.D. Tay, G.H.A. Ting, P. Biranchi, M.J. Tan (2018). Bond Strength of 3D Printed Concrete. *Proceeding of the 3rd International Conference on Progress in Additive Manufacturing (Pro-AM)* (25-30). Singapore: Nanyang Technological University.
3. Y.W.D. Tay, B. Panda, Y. Qian, M.J. Tan (2018). Progress in Construction Automation: Review on 3D Printing of Concrete Materials. *First*

International Conference on 3D Concrete Printing (3DcP) (1-9). Swinburne University of Technology, Melbourne, Australia.

4. Y.W.D. Tay, D.K.B. Sin and MJ Tan (2019). *Evaluation of Extrusion Methods for 3D Concrete Printing*. Paper presented at 13th Asia-Pacific Conference on Materials processing, Sydney, Australia.
5. B. Panda, M. Li, Y.W.D. Tay, S.C. Paul and M.J. Tan (2018). Modelling Fly Ash Based Geopolymer Flow for 3D Printing Applications. *International Conference on Advances in Construction Materials and Systems* (9-15). Chennai, India: Rilem Publications S.A.R.L.
6. W.X. Lao, Y.W.D. Tay, D. Qiurin and M.J. Tan (2018). The effect of nozzle shape on the compactness and strength of structures printed by additive manufacturing of concrete. *Proceeding of the 3rd International Conference on Progress in Additive Manufacturing (Pro-AM)* (80-86). Singapore: Nanyang Technological University
7. B. Panda, N.A.N. Mohamed, Y.W.D. Tay, L.W. He, M.J. Tan (2018). Effects of slag addition on bond strength of 3D printed geopolymer mortar: An experiment investigation. *Proceeding of the 3rd International Conference on Progress in Additive Manufacturing (Pro-AM)* (62-67). Singapore: Nanyang Technological University.
8. G.H.A. Ting, Y.W.D. Tay, A. Annapareddy, M. Li, M.J. Tan (2018). Effect of Recycled Glass Gradation in 3D Cementitious Material Printing. *Proceeding of the 3rd International Conference on Progress in Additive Manufacturing (Pro-AM)* (50-55). Singapore: Nanyang Technological University.
9. B. Panda, N.A.N. Mohamed, Y.W.D. Tay, M.J. Tan (2018). Bond strength in 3D printed geopolymer mortar. Paper presented at *RILEM 1st International Conference on Concrete and Digital Fabricaton*, Switzerland.
10. B. Panda, M. Li, Y.W.D. Tay, S.C. Paul and M.J. Tan (2017). *Fresh properties of fly ash-based geopolymer for 3D printing.* Paper presented at International Conference on Advance in Construction Materials and System, India.

11. B. Panda, Y.W.D. Tay, S.C. Paul, M.J. Tan, K.F. Leong and I. Gibson (2016, May). Current Challenges and Future Perspectives of 3D Concrete Printing. Paper presented at *2nd International Conference on Progress in Additive Manufacturing (Pro-AM) (2016)*, Nanyang Executive Center, Singapore.

Reference

[1] M. K. Hurd, *Formwork for concrete*, 7th Editio. Farmington Hills, Michigan, US: American Concrete Institute, 2006.

[2] A. S. Hanna, *Concrete formwork systems*. Madison, USA, USA: Marcel Dekker, 1998.

[3] Y. W. D. Tay, B. Panda, S. C. Paul, N. A. Noor Mohamed, M. J. Tan, and K. F. Leong, "3D printing trends in building and construction industry: a review," *Virtual and Physical Prototyping*, vol. 12, no. 3, pp. 261–276, 2017.

[4] Y. Tan, L. Shen, and H. Yao, "Sustainable construction practice and contractors' competitiveness: A preliminary study," *Habitat International*, vol. 35, no. 2, pp. 225–230, 2011.

[5] I. Kothman and N. Faber, "How 3D printing technology changes the rules of the game: Insights from the construction sector," *Journal of Manufacturing Technology Management*, vol. 27, no. 7, pp. 932–943, 2016.

[6] S. Mellor, L. Hao, and D. Zhang, "Additive manufacturing: A framework for implementation," *International Journal of Production Economics*, vol. 149, pp. 194–201, 2014.

[7] Y. W. D. Tay *et al.*, "Processing and properties of construction materials for 3D printing," in *Materials Science Forum*, 2016, vol. 861, pp. 177–181.

[8] T. T. Le, S. Austin, S. Lim, R. Buswell, A. Gibb, and T Thorpe, "Mix design and fresh properties for high-performance printing concrete," *Materials and Structures*, vol. 45, no. 8, pp. 1221–1232, 2012.

[9] N. Roussel, "Rheological requirements for printable concretes," *Cement and Concrete Research*, vol. 112, pp. 76–85, 2018.

[10] F. Bos, R. Wolfs, Z. Ahmed, and T. Salet, "Large Scale Testing of Digitally Fabricated Concrete (DFC) Elements," in *First RILEM International Conference on Concrete and Digital Fabrication -- Digital Concrete 2018*, 2019, pp. 129–147.

[11] Y. W. D. Tay, M. Y. Li, and M. J. Tan, "Effect of printing parameters in 3D concrete printing: Printing region and support structures," *Journal of Materials Processing Technology*, vol. 271, pp. 261–270, 2019.

[12] I. Perkins and M. Skitmore, “Three-dimensional printing in the construction industry: A review,” *International Journal of Construction Management*, vol. 15, no. 1, pp. 1–9, 2015.

[13] B. Khoshnevis, D. Hwang, K. T. Yao, and Z. Yah, “Mega-scale fabrication by contour crafting,” *International Journal of Industrial and Systems Engineering*, vol. 1, no. 3, pp. 301–320, 2006.

[14] G. Cesaretti, E. Dini, X. De Kestelier, V. Colla, and L. Pambaguian, “Building components for an outpost on the Lunar soil by means of a novel 3D printing technology,” *Acta Astronautica*, vol. 93, pp. 430–450, 2014.

[15] E. Dini, “D-SHAPE – The 21st century revolution in building technology has a name,” 2009. [Online]. Available: http://www.cadblog.pl/podcasty/luty_2012/d_shape_presentation.pdf. [Accessed: 15-Dec-2015].

[16] B. N. Panda, R. M. Bahubalendruni, B. B. Biswal, and M. Leite, “A CAD-based approach for measuring volumetric error in layered manufacturing,” *Proceedings of the Institution of Mechanical Engineers, Part C: Journal of Mechanical Engineering Science*, vol. 231, no. 13, pp. 2398–2406, 2017.

[17] J. Duro-Royo, L. Mogas-Soldevila, and N. Oxman, “Flow-based fabrication: An integrated computational workflow for design and digital additive manufacturing of multifunctional heterogeneously structured objects,” *CAD Computer Aided Design*, vol. 69, pp. 143–154, 2015.

[18] H. Yoshida *et al.*, “Architecture-Scale Human-Assisted Additive Manufacturing,” *ACM Transactions on Graphics (TOG)*, vol. 34, no. 4, pp. 1–8, 2015.

[19] B. Khoshnevis, “Automated construction by contour crafting - Related robotics and information technologies,” *Automation in Construction*, vol. 13, no. 1, pp. 5–19, 2004.

[20] D. Hwang and B. Khoshnevis, “Concrete Wall Fabrication by Contour Crafting,” in *ISAR 2004 21st International Symposium on Automation and Robotics in Construction*, 2004.

[21] S. Lim, R. A. Buswell, T. T. Le, S. A. Austin, A. G. F. Gibb, and T. Thorpe, “Developments in construction-scale additive manufacturing processes,”

Automation in Construction, vol. 21, pp. 262–268, 2012.

[22] S. Lim, R. A. Buswell, P. J. Valentine, D. Piker, S. A. Austin, and X. De Kestelier, "Modelling curved-layered printing paths for fabricating large-scale construction components," *Additive Manufacturing*, vol. 12, pp. 216–230, 2016.

[23] C. Nan, "A New Machinecraft," in *International Conference on Computer-Aided Architectural Design Futures*, 2015, vol. 527, pp. 422–438.

[24] S. Keating, N. A. Spielberg, J. Klein, and N. Oxman, "A compound arm approach to digital construction," in *Robotic Fabrication in Architecture, Art and Design 2014*, 2014, pp. 99–110.

[25] N. Hack and W. V. Lauer, "Mesh-Mould: Robotically Fabricated Spatial Meshes as Reinforced Concrete Formwork," *Architectural Design*, vol. 84, no. 3, pp. 44–53, 2014.

[26] J. Xu, L. Ding, and P. E. D. Love, "Digital reproduction of historical building ornamental components: From 3D scanning to 3D printing," *Automation in Construction*, vol. 76, pp. 85–96, 2017.

[27] R. J. M. Wolfs, F. P. Bos, E. C. F. van Strien, and T. A. M. Salet, "A Real-Time Height Measurement and Feedback System for 3D Concrete Printing," in *High Tech Concrete: Where Technology and Engineering Meet*, 2018, pp. 2474–2483.

[28] R. A. Buswell, W. R. L. de Silva, S. Z. Jones, and J. Dirrenberger, "3D printing using concrete extrusion: A roadmap for research," *Cement and Concrete Research*, vol. 112, pp. 37–49, 2018.

[29] A. Kazemian, X. Yuan, O. Davtalab, and B. Khoshnevis, "Computer vision for real-time extrusion quality monitoring and control in robotic construction," *Automation in Construction*, vol. 101, pp. 92–98, 2019.

[30] B. Zareiyan and B. Khoshnevis, "Effects of interlocking on interlayer adhesion and strength of stucutres in 3D printing of concrete," *Automation in Construction*, vol. 83, pp. 212–221, 2017.

[31] T. Marchment, J. Sanjayan, and M. Xia, "Method of enhancing interlayer bond strength in construction scale 3D printing with mortar by effective bond area amplification," *Materials & Design*, vol. 169, p. 107684, 2019.

[32] E. Hosseini, M. Zakertabrizi, A. Habibnejad Korayem, and G. Xu, “A novel method to enhance the interlayer bonding of 3D printing concrete: An experimental and computational investigation,” *Cement and Concrete Composites*, vol. 99, pp. 112–119, 2019.

[33] J. H. Lim, B. Panda, and Q.-C. Pham, “Improving flexural characteristics of 3D printed geopolymer composites with in-process steel cable reinforcement,” *Construction and Building Materials*, vol. 178, pp. 32–41, 2018.

[34] B. Panda, S. C. Pual, and M. Tan, “Anisotropic mechanical performance of 3D printed fiber reinforced sustainable construction material,” *Materials Letters*, vol. 209, no. 15, pp. 146–149, 2017.

[35] G. H. A. Ting, Y. W. D. Tay, Y. Qian, and M. J. Tan, “Utilization of recycled glass for 3D concrete printing: rheological and mechanical properties,” *Journal of Material Cycles and Waste Management*, pp. 1–10, Mar. 2019.

[36] B. Lu, M. Li, K. F. Leong, S. Qian, and M. J. Tan, “Develop cementitious materials incorporating fly ash cenophere for spray-based 3D printing,” in *Proceedings of the 3rd International Conference on Progress in Additive Manufacturing (Pro-AM 2018)*, 2018, pp. 38–43.

[37] X. Zhang *et al.*, “Large-scale 3D printing by a team of mobile robots,” *Automation in Construction*, vol. 95, pp. 98–106, 2018.

[38] B. Panda, S. Ruan, C. Unluer, and M. J. Tan, “Improving the 3D printability of high volume fly ash mixtures via the use of nano attapulgite clay,” *Composites Part B: Engineering*, vol. 165, pp. 75–83, 2019.

[39] V. S. Fratello and R. Rael, “Cool brick,” *Emerging Objects*, 2015. [Online]. Available: http://www.emergingobjects.com/2015/03/07/cool-brick/. [Accessed: 31-Jan-2019].

[40] R. Stott, “Emerging objects creates ‘Bloom’ pavilion from 3D printed cement,” *Arch Daily*, 2015. [Online]. Available: https://www.archdaily.com/613171/emerging-objects-creates-bloom-pavilion-from-3-d-printed-cement. [Accessed: 31-Jan-2019].

[41] C. Gosselin, R. Duballet, P. Roux, N. Gaudillière, J. Dirrenberger, and P.

Morel, “Large-scale 3D printing of ultra-high performance concrete - a new processing route for architects and builders,” *Materials and Design*, vol. 100, pp. 102–109, 2016.

[42] B. Panda, Y. W. D. Tay, S. C. Paul, and M. J. Tan, “Current challenges and future potential of 3D concrete printing,” *Materials science and Engineering Technology*, vol. 49, no. 5, pp. 666–673, 2018.

[43] B. N. Panda, S. C. Paul, N. A. N. Mohamed, Y. W. D. Tay, and M. J. Tan, “Measurement of tensile bond strength of 3D printed geopolymer mortar,” *Measurement*, vol. 113, pp. 108–116, 2018.

[44] B. Panda and M. J. Tan, “Experimental study on mix proportion and fresh properties of fly ash based geopolymer for 3D concrete printing,” *Ceramics International*, vol. 44, no. 9, pp. 10258–10265, 2018.

[45] National Environment Agency, “Waste management statistics and overall recycling measures,” 2018. [Online]. Available: https://www.nea.gov.sg/our-services/waste-management/waste-statistics-and-overall-recycling. [Accessed: 31-Jan-2019].

[46] G. H. A. Ting, Y. W. D. Tay, A. Annapareddy, M. Li, and M. J. Tan, “Effect of recycled glass gradation in 3D cementitious material printing,” in *Proceedings of the 3rd International Conference on Progress in Additive Manufacturing (Pro-AM 2018)*, 2018, pp. 50–55.

[47] A. U. Nilsen and P. J. Monteiro, “Concrete: a three phase material,” *Cement and Concrete Research*, vol. 23, no. 1, pp. 147–151, 1993.

[48] D. Kaplan, F. de Larrard, and T. Sedran, “Avoidance of blockages in concrete pumping process,” *ACI Materials Journal*, vol. 102, pp. 183–191, 2005.

[49] R. A. Crepas, *Pumping Concrete: Techniques and application*, 3rd ed. Elmhurst: Crepas and Associates Inc., 1997.

[50] S. H. Kwon, K. P. Jang, J. H. Kim, and S. P. Shah, “State of the Art on Prediction of Concrete Pumping,” *International Journal of Concrete Structures and Materials*, vol. 10, no. 3, pp. 75–85, 2016.

[51] V. Mechtcherine, V. N. Nerella, and K. Kasten, “Testing pumpability of concrete using Sliding Pipe Rheometer,” *Construction and Building*

Materials, vol. 53, pp. 312–323, 2014.

[52] M. Choi, N. Roussel, Y. Kim, and J. Kim, "Lubrication layer properties during concrete pumping," *Cement and Concrete Research*, vol. 45, pp. 69–78, 2013.

[53] T. T. Ngo, E. H. Kadri, R. Bennacer, and F. Cussigh, "Use of tribometer to estimate interface friction and concrete boundary layer composition during the fluid concrete pumping," *Construction and Building Materials*, vol. 24, no. 7, pp. 1253–1261, 2010.

[54] K. H. Jeon, M. B. Park, M. K. Kang, and J. . Kim, "Development Of An Automated Freeform Construction System And Its Construction Materials," in *Proceedings of the 30th International Symposium on Automation and Robotics in Construction and Mining*, 2013, pp. 1359–1365.

[55] Z. Malaeb *et al.*, "3D Concrete Printing: Machine and Mix Design," *International Journal of Civil Engineering and Technology*, vol. 6, no. 6, pp. 14–22, 2015.

[56] A. Perrot, D. Rangeard, and A. Pierre, "Structural built-up of cement-based materials used for 3D-printing extrusion techniques," *Materials and Structures*, vol. 49, no. 4, pp. 1213–1220, 2016.

[57] T. T. Le *et al.*, "Hardened properties of high-performance printing concrete," *Cement and Concrete Research*, vol. 42, no. 3, pp. 558–566, 2012.

[58] J. Hu, "A study of effects of aggregate on concrete rheology," PhD Thesis, Iowa State University, 2005.

[59] M. Thomas and P. Eng, "Optimizing the use of fly ash in concrete," *Portland Cement Association*, p. 24, 2007.

[60] V. M. Malhotra, "Global warming, and role of supplementary cementing materials and superplasticisers in reducing greenhouse gas emissions from the manufacturing of portland cement.," *International Journal of Structural Engineering*, vol. 1, no. 2, pp. 116–130, 2010.

[61] P. C. Aïtcin, "Cements of yesterday and today: concrete of tomorrow," *Cement and Concrete Research*, vol. 30, no. 9, pp. 1349–1359, 2000.

[62] S. H. Kosmatka, B. Kerkhoff, and W. C. Panarese, *Design and Control of Concrete Mixture*, 14th ed. Skokie, IL: Portland Cement Association, 2002.

[63] D. A. R. Jones, B. Leary, and D. V Boger, “The rheology of a concentrated colloidal suspension of hard spheres,” *Journal of Colloid and Interface Science*, vol. 147, no. 2, pp. 479–495, 1991.

[64] P. Coussot, *Rheometry of pastes, suspensions and granular materialss : Applications in industry and environment*. John Wiley & Sons, Inc, 2005.

[65] H. Hoorndhad, “Toward development of self-compacting no-clump concrete mixtures,” *PhD thesis*, 2014.

[66] C. T. Kennedy, “The Design of Concrete Mixes,” *Journal of the American Concrete Institute*, vol. 36, no. 2, pp. 373–400, 1940.

[67] K. van B. Hooman Hoornahad, Eduardus A. B. Koenders, “Towards the development of self-compacting no-slump concrete mixtures,” *Journal of Sillicate Based and Composite Materials*, vol. 67, no. 4, pp. 135–139, 2015.

[68] S. C. Paul, Y. W. D. Tay, B. Panda, and M. J. Tan, “Fresh and hardened properties of 3D printable cementitious materials for building and construction,” *Archives of Civil and Mechanical Engineering*, vol. 18, no. 1, pp. 311–319, 2018.

[69] S. Austin, P. Robins, and Y. Pan, “Tensile bond testing of concrete repairs,” *Materials and Structures*, vol. 28, pp. 249–259, 1995.

[70] B. Zareiyan and B. Khoshnevis, “Interlayer adhesion and strength of structures in Contour Crafting - Effects of aggregate size, extrusion rate and layer thickness,” *Automation in Construction*, vol. 81, pp. 112–121, 2017.

[71] B. Zareiyan and B. Khoshnevis, “Effects of mixture ingredient on interlayer adhesion of concrete in Contour Crafting,” *Rapid Prototyping Journal*, vol. 24, no. 3, pp. 584–592, 2018.

[72] Y. W. D. Tay, G. H. A. Ting, Y. Qian, B. Panda, L. He, and M. J. Tan, “Time gap effect on bond strength of 3D-printed concrete,” *Virtual and Physical Prototyping*, vol. 14, pp. 104–113, 2019.

[73] B. Khoshnevis *et al.*, “Lunar contour crafting—a novel technique for ISRU-based habitat development,” in *American Institute of Aeronautics and Astronautics Conference*, 2005, no. January, pp. 5–19.

[74] J. F. D. Dahmen and J. A. Ochsendorfs, “Earth masonry structures: arches, vaults and domes,” in *Woodhead Publishing Series in Energy*, M. R. Hall, R.

Lindsay, and M. B. T.-M. E. B. Krayenhoff, Eds. Woodhead Publishing, 2012, pp. 427–460.

[75] G. Strano, L. Hao, R. M. Everson, and K. E. Evans, "A new approach to the design and optimisation of support structures in additive manufacturing," *The International Journal of Advanced Manufacturing Technology*, vol. 66, no. 9–12, pp. 1247–1254, 2013.

[76] J. W. Stansbury and M. J. Idacavage, "3D printing with polymers: Challenges among expanding options and opportunities," *Dental Materials*, vol. 32, no. 1, pp. 54–64, 2016.

[77] M. Fahad, P. Dickens, and M. Gilbert, "Novel polymeric support materials for jetting based additive manufacturing processes," *Rapid Prototyping Journal*, vol. 19, no. 4, pp. 230–239, 2013.

[78] J. Kaufhold *et al.*, "Wood-based support material for extrusion-based digital construction," *Rapid Prototyping Journal*, vol. 25, no. 4, pp. 690–698, Jan. 2019.

[79] J. Dumas, J. Hergel, and S. Lefebvre, "Bridging the gap: Automated steady scaffoldings for 3D printing," *ACM Transactions on Graphics (TOG)*, vol. 33, no. 4, pp. 98(1)-98 (10), 2014.

[80] J. Vanek, J. A. G. Galicia, and B. Benes, "Clever Support: Efficient Support Structure Generation for Digital Fabrication," *Computer Graphics Forum*, vol. 33, no. 5, pp. 117–125, 2014.

[81] S. Cacace, E. Cristiani, and L. Rocchi, "A level set based method for fixing overhangs in 3D printing," *Applied Mathematical Modelling*, vol. 44, pp. 446–455, 2017.

[82] O. S. Carneiro, A. F. Silva, and R. Gomes, "Fused deposition modeling with polypropylene," *Materials & Design*, vol. 83, pp. 768–776, 2015.

[83] M. H. Zhang and O. E. Gjvorv, "Mechanical properties of high-strength lightweight concrete," *American Concrete Institute Materials Journal*, vol. 88, no. 3, pp. 240–247, 1991.

[84] J. Roesler, G. Paulino, C. Gaedicke, A. Bordelon, and K. Park, "Fracture behavior of functionally graded concrete materials for rigid pavements," *Transportation Research Record*, vol. 2037, no. 1, pp. 40–49, 2007.

[85] A. Nazari and J. G. Sanjayan, “Compressive strength of functionally graded geopolymers - role of position of layers,” *Construction and Building Materials*, vol. 75, pp. 31–34, 2015.

[86] N. Oxman, S. Keating, and E. Tsai, “Functionally graded rapid prototyping,” in *Proceedings of VRAP: Advanced Research in Virtual and Rapid Prototyping*, 2011, pp. 483–489.

[87] M. C. Leu, B. K. Deuser, L. Tang, R. G. Landers, G. E. Hilmas, and J. L. Watts, “Freeze-form extrusion fabrication of functionally graded materials,” *CIRP Annals*, vol. 61, no. 1, pp. 223–226, 2012.

[88] R.Rashid, S. H. Masooda, D. Ruan, S. Palanisamy, X. Huang, and R. A. R. Rashid, “Topology optimisation of additively manufactured lattice beams for three-point bending test,” in *Annual International Solid Freeform Fabrication Symposium*, 2018, pp. 635–647.

[89] P. Martens, M. Mathot, F. Bos, and J. Coenders, “Optimising 3D printed concrete structures using topology optimisation,” in *High Tech Concrete: Where Technology and Engineering Meet*, 2018, pp. 301–309.

[90] D. Han and R. D. Ferron, “Effect of mixing method on microstructure and rheology of cement paste,” *Construction and Building Materials*, vol. 93, pp. 278–288, 2015.

[91] D. Lowke, T. Kränkel, C. Gehlen, and P. Schießl, “Effect of Cement on Superplasticizer Adsorption, Yield Stress, Thixotropy and Segregation Resistance,” in *Design, Production and Placement of Self-Consolidating Concrete*, 2010, pp. 91–101.

[92] A. W. Saak, H. M. Jennings, and S. P. Shah, “A generalized approach for the determination of yield stress by slump and slump flow,” *Cement and Concrete Research*, vol. 34, no. 3, pp. 363–371, 2004.

[93] N. Roussel, “From industrial testing to rheological parameters for concrete,” in *Understanding the Rheology of Concrete*, N. Roussel, Ed. Woodhead Publishing, 2012, pp. 83–95.

[94] T. Marchment, J. G. Sanjayan, B. Nematollahi, and M. Xia, “Interlayer strength of 3D printed concrete: influencing factors and method of enhancing,” in *3D Concrete Printing Technology*, J. G. Sanjayan, A. Nazari,

and B. Nematollahi, Eds. Butterworth-Heinemann, 2019, pp. 241–264.

[95] R. K. Dhir, J. de Brito, R. V Silva, and C. Q. Lye, "Use of recycled aggregates in mortar," in *Sustainable Construction Materials*, R. K. Dhir, J. de Brito, R. V Silva, and C. Q. Lye, Eds. Woodhead Publishing, 2019, pp. 143–179.

[96] G. De Schutter and D. Feys, "Pumping of fresh concrete: Insights and challenges," *RILEM Technical Letters*, vol. 1, pp. 76–80, 2016.

[97] Ma. Jolin, D. Burns, B. Bissonnette, F. Gagnon, and L.-S. Bolduc, "Understanding the pumpability of concrete," in *Shotcrete for Underground Support XI*, 2009, pp. 1–14.

[98] L. G. Li and A. K. H. Kwan, "Mortar design based on water film thickness," *Construction and Building Materials*, vol. 25, no. 5, pp. 2381–2390, 2011.

[99] N. Roussel, G. Ovarlez, S. Garrault, and C. Brumaud, "The origins of thixotropy of fresh cement pastes," *Cement and Conrete Research*, vol. 42, pp. 148–157, 2012.

[100] Y. Zhang, Y. Zhang, G. Liu, Y. Yang, M. Wu, and B. Pang, "Fresh properties of a novel 3D printing concrete ink," *Construction and Building Materials*, vol. 174, pp. 263–271, 2018.

[101] S. C. Figueiredo *et al.*, "An approach to develop printable strain hardening cementitious composites," *Materials & Design*, vol. 169, p. 107651, 2019.

[102] O. H. Wallevik, D. Feys, J. E. Wallevik, and K. H. Khayat, "Avoiding inaccurate interpretations of rheological measurements for cement-based materials," *Cement and Concrete Research*, vol. 78, pp. 100–109, 2015.

[103] S. Chidiac, D. Chan, and F. Habibbeigi, "Slump and slump flow for characterizing yield value of fresh concrete," *Materials Journal*, vol. 103, no. 6, pp. 413–418, 2006.

[104] ASTM Standard C230/ C230M-14, "Standard specification for flow table for use in tests of hydraulic cement," *ASTM International*, West Conshohocken, PA, 2014.

[105] N. Roussel and P. Coussot, "'Fifty-cent rheometer' for yield stress measurements: From slump to spreading flow," *Journal of Rheology*, vol. 49, no. 3, pp. 705–718, 2005.

[106] A. I. Laskar, “Correlating slump, slump flow, vebe and flow tests to rheological parameters of high-performance concrete,” *Materials Research*, vol. 12, pp. 75–81, 2009.

[107] S. H. Kosmatka and M. L. Wilson, *Design and control of concrete mixtures*, 15th editi. Portland Cement Association, Skokie, Illinois, USA, 2011.

[108] S. H. Kosmatka, B. Kerkhoff, and W. C. Panarese, *Design and control of concrete mixtures*, 14th editi. Portland Cement Association, Skokie, Illinois, USA, 2002.

[109] ASTM C1437-15, “Standard test method for flow of hydraulic cement mortar,” *ASTM International*, West Conshohocken, PA, 2015.

[110] J. H. Lee, J. H. Kim, and J. Y. Yoon, “Prediction of the yield stress of concrete considering the thickness of excess paste layer,” *Construction and Building Materials*, vol. 173, pp. 411–418, 2018.

[111] P. Domone, “The Slump Flow Test for High-Workability Concrete 11Communicated by C.D. Pomeroy.,” *Cement and Concrete Research*, vol. 28, no. 2, pp. 177–182, 1998.

[112] P. F. G. Banfill, “Rheology of fresh cement and concrete,” *Rheology Reviews*, pp. 61–130, 2006.

[113] P. F. G. Banfill, “The rheology of fresh cement and concrete: A review,” in *Proceeding for 11th International Cement Chemistry Congress*, 2003, pp. 1–13.

[114] P. F. G. Banfill, “The rheology of cement and concrete - A review,” in *Proceeding for 11th International Cement Chemistry Congress*, 2003, pp. 1–13.

[115] F. J. Rubio-Hernández, J. F. Velázquez-Navarro, and F. J. Galindo-Rosales, “Rheological characterization of a time dependent fresh cement paste,” *Mechanics of Time-Dependent Materials*, vol. 13, pp. 199–206, 2009.

[116] S. M. Mansour, M. T. Abadlia, K. Bekkour, and I. Messaoudene, “Improvement of rheological behaviour of cement pastes by incorporating metakaolin,” *European Journal of Scientific Research*, vol. 42, no. 3, pp. 442–452, 2010.

[117] R. P. Chhabra and J. F. Richardson, *Non-Newtonian Flow and Applied*

Rheology, 2nd editio. 2008.

[118] F. M. Léon-Marti and P. F. de J. Cano-Barrita, "Yield Stress of Mortars in Rotational and Oscillatory Shear Experiments Conducted Using a Ball Measuring System," *Applied Rheology*, vol. 27, pp. 1–11, 2017.

[119] N. Roussel and F. Cussigh, "Distinct-layer casting of SCC: the mechanical consequences of thixotropy," *Cement and Concrete Research*, vol. 38, pp. 624–632, 2008.

[120] Anton Paar GmbH, "Extended material characterization," 2017. [Online]. Available: https://www.anton-paar.com/?eID=documentsDownload&document=18382&L=0. [Accessed: 07-Apr-2018].

[121] ASTM C1583 / C1583M-13, "Standard Test Method for Tensile Strength of Concrete Surfaces and the Bond Strength or Tensile Strength of Concrete Repair and Overlay Materials by Direct Tension (Pull-off Method)," ASTM International, West Conshohocken, PA, 2013.

[122] A. Varshney *et al.*, "Rheology of hydrating cement paste: Crossover between two aging processes," *Cement and Concrete Research*, vol. 95, pp. 226–231, 2017.

[123] A. Franck, "Understanding rheology of structured fluids," TA Instruments, 2004.

[124] M. A. Schultz and L. j. Struble, "Use of Oscillatory shear to study flow behavior of fresh cement paste," *Cement and Concrete Research*, vol. 23, pp. 273–282, 1993.

[125] M. Choi, K. Park, and T. Oh, "Viscoelastic properties of fresh cement paste to study the flow behavior," *international journal of concrete structures and materials*, vol. 10, no. 3, pp. S65–S74, 2016.

[126] F. A. Mazzeo, "Importance of Oscillatory Time Sweeps in Rheology," *TA Instruments*, 2012. [Online]. Available: http://www.tainstruments.com/pdf/literature/RH081.pdf. [Accessed: 05-Dec-2017].

[127] T. Nick, "Measurement of fluid rheology and interpretation of rheograms," Kaltec Scientific, Michigan, USA, Michigan, USA, 1988.

[128] J. W. Bullard *et al.*, "Mechanisms of cement hydration," *Cement and Concrete Research*, vol. 41, pp. 1208–1223, 2011.

[129] A. Papo and B. Caufin, "A study of the hydration process of cement pastes by means of oscillatory rheological techniques," *Cement and Concrete Research*, vol. 21, pp. 1111–1117, 1991.

[130] J. G. Sanjayan, B. Nematollahi, M. Xia, and T. Marchment, "Effect of surface moisture on interlayer strength of 3D printed concrete," *Construction and Building Materials*, vol. 172, pp. 468–475, 2018.

[131] V. N. Nerella, S. Hempel, and V. Mechtcherine, "Effects of layer-interface properties on mechanical performance of concrete elements produced by extrusion-based 3D-printing," *Construction and Building Materials*, vol. 205, pp. 586–601, 2019.

[132] P. Feng, X. Meng, J.-F. Chen, and L. Ye, "Mechanical properties of structures 3D printed with cementitious powders," *Construction and Building Materials*, vol. 93, pp. 486–497, 2015.

[133] A. Rudenko, "3D concrete house printer," *3D Concrete Printer - Designed to print medium-sized homes*, 2014. [Online]. Available: http://www.totalkustom.com/video.html. [Accessed: 02-Aug-2018].

[134] G. Carra and L. Stabile, "Pushing the boundaries of 3D printing," *The Arup Journal*, vol. 1, no. 1, pp. 28–31, 2018.

[135] W. C. Panarese, "Concrete for pumping," *Concrete Construction*, pp. 1–5, 1973.

[136] ASTM C33 / C33M-18, "Specification for Concrete Aggregates," *ASTM International*, 2018.

[137] W. Lao, M. Li, L. Masia, and M. J. M. J. Tan, "Approaching rectangular extrudate in 3D printing for building and construction by experimental iteration of nozzle design," in *Proceedings of the 28th Annual International Solid Freeform Fabrication Symposium (SFF 2017)*, 2017, pp. 2612–2623.

[138] D. C. Montgomery, *Design and analysis of experiments*. New York, USA: John Wiley & Sons, 2017.

[139] Y. Jin, Y. He, and J. Fu, "Support generation for additive manufacturing based on sliced data," *The International Journal of Advanced Manufacturing*

Technology, vol. 80, no. 9–12, pp. 2041–2052, 2015.

[140] N. Oxman, "Variable property rapid prototyping," *Virtual and Physical Prototyping*, vol. 6, no. 1, pp. 3–31, 2011.

[141] R. M. Mahamood and E. T. Akinlabi, *Functionally graded materials*. Springer International Publishing, 2017.

[142] D. Delgado Camacho *et al.*, "Applications of additive manufacturing in the construction industry - a prospective review," in *Proceedings of the 34rd International Symposium on Automation and Robotics in Construction*, 2017, pp. 246–253.

[143] A. Bhardwaj *et al.*, "Additive Manufacturing Processes for Infrastructure Construction: A Review," *Journal of Manufacturing Science and Engineering*, p. 1, 2019.

[144] Y. Chen, S. Chaves Figueiredo, Ç. Yalçınkaya, O. Çopuroğlu, F. Veer, and E. Schlangen, "The effect of viscosity-modifying admixture on the extrudability of limestone and calcined clay-based cementitious material for extrusion-based 3D concrete printing," *Materials*, vol. 12, p. 1374, 2019.

[145] D. Asprone, F. Auricchio, C. Menna, and V. Mercuri, "3D printing of reinforced concrete elements: Technology and design approach," *Construction and Building Materials*, vol. 165, pp. 218–231, 2018.

[146] T. A. M. Salet, Z. Y. Ahmed, F. P. Bos, and H. L. M. Laagland, "Design of a 3D printed concrete bridge by testing," *Virtual and Physical Prototyping*, vol. 13, no. 3, pp. 222–236, 2018.

[147] R. Larsson, "Methodology for topology and shape optimization: application to a rear lower control arm," *Master Thesis, Department of Applied Mechanics, Chalmers University of Technology, Goteborg*, 2016.

[148] M. P. Bendsoe and O. Sigmund, *Topology optimization: theory, methods, and applications*. Springer-Verlag Berlin Heidelberg, 2004.

[149] ASTM C293/C293M − 16, "Standard test method for flexural strength of concrete (using simple beam with center-point loading)," *ASTM International, West Conshohocken, PA*, 2016.

[150] C. C. Mitropoulou, Y. Fourkiotis, N. D. Lagaros, and M. G. Karlaftis, "Evolution strategies-based metaheuristics in structural design optimization,"

in *Metaheuristic Applications in Structures and Infrastructures*, A. H. Gandomi, X.-S. Yang, S. Talatahari, and A. H. Alavi, Eds. Oxford: Elsevier, 2013, pp. 79–102.

[151] Y. Huang, Z. Yang, W. Ren, G. Liu, and C. Zhang, "3D meso-scale fracture modelling and validation of concrete based on in-situ X-ray computed tomography images using damage plasticity model," *International Journal of Solids and Structures*, vol. 67–68, pp. 340–352, 2015.

[152] J. Lott and C. E. Kesler, "Crack propagation in plain concrete," *Symposium on Structure of Portland Cement Paste and Concrete, Special Report No. 90, Highway Research Board*, pp. 204–218, 1966.

[153] T. Marchment, M. Xia, E. Dodd, J. Sanjayan, and B. Nematollahi, "Effect of delay time on the mechanical properties of extrusion-based 3D printed concrete," in *34th International Symposium on Automation and Robotics in Construction (ISARC)*, 2017, pp. 240–245.

[154] M. F. Kaplan, "Crack propagation and the fracture of concrete," *American Concrete Institute Journal Proceedings*, vol. 58, no. 11, pp. 591–610, 1961.

[155] J. Glucklich, "Fracture of Plain Concrete," *Journal of the Engineering Mechanics Division*, vol. 89, no. 6, pp. 127–138, 1963.

[156] V. N. Nerella, M. A. B. Beigh, S. Fataei, and V. Mechtcherine, "Strain-based approach for measuring structural build-up of cement pastes in the context of digital construction," *Cement and Concrete Research*, vol. 115, pp. 530–544, 2019.

[157] E. Koehler, A. Jeknavorian, and S. Klaus, "Selecting Admixtures to Achieve Application-Required Rheology," in *Design, Production and Placement of Self-Consolidating Concrete*, 2010, pp. 79–88.

[158] T. A. Bürge, "Mode of action of alkali-free sprayed shotcrete accelerators," in *International Conference on Engineering Developments in Shotcrete*, 2001, pp. 79–85.

[159] C. Paglia, F. Wombacher, and H. Böhni, "The influence of alkali-free and alkaline shotcrete accelerators within cement systems: I. Characterization of the setting behavior," *Cement and Concrete Research*, vol. 31, no. 6, pp. 913–918, 2001.

[160] R. Myrdal, “Accelerating admixtures for concrete,” SINTEF Building and Infrastructure; Concrete Innovation Center (COIN), Norway, 2007.

[161] R. J. M. Wolfs, F. P. Bos, and T. A. M. Salet, “Early age mechanical behaviour of 3D printed concrete: Numerical modelling and experimental testing,” *Cement and Concrete Research*, vol. 106, pp. 103–116, 2018.

[162] S. Gupta and C. Gautam, “A Review on short column seismic behavior and their prevention on sloping ground,” *Journal of Civil Engineering and Environmental Technology*, vol. 3, no. 6, pp. 523–528, 2016.